Title

Seismic constrains on a double-layered Hawaiian plume and the Cascadia subduction slab heterogeneity

Author

Cheng, Cheng

Publication Date

2016

Peer reviewed|Thesis/dissertation

Seismic constrains on a double-layered Hawaiian plume and the Cascadia subduction slab heterogeneity

by

Cheng Cheng

A dissertation submitted in partial satisfaction of the
requirements for the degree of
Doctor of Philosophy

in

Earth and Planetary Science

in the

Graduate Division

of the

University of California, Berkeley

Committee in charge:

Professor Richard Allen, Chair
Professor Bruce Buffett
Professor David Brillinger

Fall 2016

Seismic constrains on a double-layered Hawaiian plume and the Cascadia subduction slab heterogeneity

Abstract

Seismic constrains on a double-layered Hawaiian plume and

the Cascadia subduction slab heterogeneity

by

Cheng Cheng

Doctor of Philosophy in Earth and Planetary

Science University of California, Berkeley

Professor Richard Allen, Chair

It is generally accepted that mantle plumes are responsible for hotspot chains, and as such provide insight to mantle convection processes. Among all the hotspots, the Hawaii chain is a characteristic example that has been extensively explored. But many questions remain including, what is the shape, size and orientation of the plume conduit? To what extent can the seismic structure of the plume be mapped? Can we see a continuous plume conduit extending from the lower to the upper mantle? At what depth do melting processes occur? In the first part of this thesis, we are trying to answer these questions from a seismic imaging perspective. We combine constraints from three data sets (body waves, ballistic surface waves and ambient noise) to create 3D images of the velocity structure beneath the Hawaiian island chain from a depth of ~800 km to the surface. Our multiphase 3D model results indicate there is a large deep-rooted low velocity anomaly rising from the lower mantle. At transition zone depth the conduit is located to the southeast of Hawaii. A 2% S-wave anomaly is observed in the core of the plume conduit around 700 km depth which, once corrected for damping effects, suggests a 200-250°C temperature anomaly assuming a thermal plume. In the upper mantle, there is a horizontal plume "pancake" at shallow depths beneath the oceanic lithosphere, and there is also a second horizontal low-velocity layer in the 250 to 410 km depth range beneath the island chain. We suggest this feature is a deep eclogite pool (DEP), an interpretation consistent with geodynamic modeling.

The second major part of this thesis is imaging the Cascadia subduction plate. First, we present a novel 3-D pre-stack Kirchhoff depth migration (PKDM) method for teleseismic receiver functions. The proposed algorithm considers the effects of diffraction, scattering and traveltime alteration caused by 3-D volumetric heterogeneities. It is therefore particularly useful for imaging complex 3-D structures such as dipping discontinuities, which is hard to accomplish with traditional methods. Next, we present a 3D model of upper mantle seismic discontinuity structure below Cascadia using this migration method. In this model, multiple and primary signals are

separated by our analysis. The 410km discontinuity is observed across the entire image together with lithosphere-asthenosphere boundary (LAB). A fine analysis of the primary and multiple reverberated phases allows imaging of the Juan de Fuca plate dipping below the North American continent. At two frequency bands (5 s and 10 s period), the main seismic discontinuities in the plate are limited to a downward increase of shear-wave velocities. Our model shows along-strike variations in the visibility of this discontinuity. To the southern and northern ends of the subduction system, the discontinuity is clearly observed down to the transition zone. In the center under central Oregon, this structure is however missing, which leaves a seismic discontinuity gap within the subducted oceanic plate at the depth between ~150 km and ~300 km. We attribute the observed heterogeneity of the discontinuity structure inside oceanic plate to different hydration and plume-slab processes prior to and during subduction.

Contents

List of Figures

Acknowledgments

I want to start with this special acknowledgement to my advisor, Professor Richard Allen. I first met Richard in Beijing, when I was a master student in Chinese Academy of Science. Little did I expect he would bring me to Berkeley and I would have a chance to work with him for great five years. Richard has always been a great advisor during my research time. Richard has spurred me to grow towards a successful Ph.D. by constantly challenging me with new questions and putting high standard on the quality of work. I benefit from him in nearly everything associated with scientific research: the attitude towards science, the standards for writing a scientific paper, an open mind in collaboration with other researchers around the world, and so on. Perhaps two of the benefits gained from Richard are of the greatest importance to me: the capability of independent research and the capability of being detail-oriented researcher. Additionally, I sincerely appreciate the large freedom he has granted me to focus on the problems I find most interesting. He gives me great support when I was trying to learn the technique in oil industry and apply it back to the global earth structure imaging problem. I look forward for future collaborations with Richard if I continue my research career.

I would like to thank the other two members of my dissertation committee, Professor Bruce Buffett and Professor David Brillinger – both of whom provided valuable feedback not only on the material in this thesis, but also as members of my qualifying exam committee and in their courses that I've had the pleasure of taking. And I would like to thank another member of my qualifying exam committee – Professor Donald DePaolo also for his great help and discussion.

I would like to thank the collaborators with whom I've had the opportunity to work over the past years – particularly Thomas Bodin and Rob Porritt for their insights and for many hours of stimulating conversation. Rob helped me on my first project, where he guided me through the tomography code our group is using. Thomas helped me a lot on my second project. He has broad view on geophysics and passion on trying new ideas together with me. Without them, this thesis won't be able to be finished.

I want to thank the faculty here at Berkeley Seismological Laboratory (BSL) for the outstanding high quality and challenging classes provided here. I want to thank Professor Barbara Romanowicz, who allows me to go to her group meeting and answer me various naive questions. I would also like to thank the BSL and EPS staff who have helped me overcome several challenges in both research and academics.

I like to thank my best friend and colleague Qingkai Kong. Qingkai came to Berkeley the same year as me, both as student of Richard. He accompanies me through these five years and help me at every aspect of normal life. I would immediately think about him when I am in trouble.

A big thank you to all the previous and current graduate students in BSL and EPS department: Sanne Cottar, Aurelie Guilhem, Shan Dou, Allen Zhao, Scott French, Andrea Chiang, Sierra Boyd, Felipe Orellana, Heidi Fuqua, Eloisa Zepeda, Avinash Nayak, William Hawley, Robert Martin-Short, Chris Johnson, Kathryn Materna, Alex Robson, Nate Lindsey, etc. I first come to Berkeley as an international student who knows little about the culture and has bad English. People help me to get familiar with the amazing

culture of Berkeley and America. Also, academically, talking with them is great benefit.

Finally, I dedicate this thesis to my family, my parents, Yanhua Cheng and Huiqing Zhang. Without their continuous support, I can't imagine how I can finish such a long journey of studying.

Chapter 1

Introduction

In most seismologists' minds, the complicated earth structure is simplified as two end members: the low frequency end which is represented by velocity perturbation to some reference earth model and the high frequency end which is represented by discontinuity structure that reflect and transmit seismic waves. By understanding them we can improve our knowledge of the physical composition of the Earth, the thermal structure, the dynamic process, and the history of Earth's evolution. High resolution seismic imaging is an efficient tool to understand them in detail, and different seismic methods can be applied to reveal these two end members. In this thesis we explore the complicated Earth structure as imaged with different imaging techniques and use to images to address scientific questions about physical Earth processes. It is primarily composed of two major pieces of work during my PhD. The first is the Hawaii plume seismic velocity structure as revealed by finite frequency seismic tomography. The second is the Cascadia subduction system seismic discontinuity structure as revealed by receiver function Kirchhoff migration.

Many researchers consider the Hawaii island chain to be a case example of a deep-rooted whole-mantle plume [Morgan, 1971]. There is an ongoing debate about the morphology of the plume system including the depth of origin, and direction from which the plume originates if it is not vertical. The structure of the plume in the upper mantle and how it interacts with the overriding lithosphere of the Pacific Plate is also an open question with a variety of geochemical interpretations [e.g. Lassiter et al., 1996; Abouchami et al., 2005; Huang et al., 2011; Weis et al., 2011] and geodynamical models attempting to predict the possible interactions [e.g. Detrick and Crough, 1978; Monnereau et al., 1993; Farnetani et al., 2009, 2010, 2012; Rychert et al., 2013]. Seismic tomography techniques provide a powerful mechanism to constrain the 3D structure and origin of the island chain. Studies that rely exclusively on on-shore recorded data have a limited aperture (width) of the seismic array and the poor ray-path coverage makes it impossible to fully assess the deeper mantle structure. More recent regional studies instead make use of the offshore deployment of seismometers during the Plume and Lithosphere Undersea Melt Experiment (PLUME) data [Wolfe et al., 2009, 2011; Laske et al., 2007, 2011], which increases the aperture, and thereby constrains structure over a wider area at shallow depth, and also deeper into the lower mantle. In Chapter 2 we combine body- and surface-wave observations using a joint inversion scheme and a finite frequency kernel approach. Our method uses teleseismic body-wave traveltime measurements and surface-wave phase velocity information from ballistic surface waves and ambient noise cross-correlation measurements. All constraints are jointly inverted to obtain a multiphase tomographic shear-wave velocity model. The resulting model

constrains structure from the surface down to ~800 km depth. It is simultaneously consistent with all the seismic observations, meaning that it takes advantage of the surface wave constraints to resolve shallow (<200km) structure, while being consistent with teleseismic traveltimes that are able to constrain deeper structure.

Seismic tomography can reveal the low frequency velocity structure of the deep earth, while in contrast seismic migration is another technique which can reveal the high frequency discontinuity structure. There are plenty of discontinuity structures in the deep Earth, such as, Moho, LAB, 410km, 660km. These discontinuity structures are a reflection of chemical and thermal structure of deep Earth and can provide useful information about the dynamic process of the mantle. In Chapter 3, we first show a novel seismic receiver function migration method which can image in high resolution 3D, dipping structures. Receiver functions observed at different stations of an array of seismometers may be combined into a 2D or 3D volume and interpreted structurally. We present an efficient 3D pre-stack Kirchhoff depth migration method for teleseismic receiver functions. It is similar to the acoustic wave migration scheme, as it can account for 3D dipping structures and strong volumetric heterogeneities. However, this migration scheme is easy to implement and as fast and efficient as CCP depth mapping [Cheng et al., 2016]. It leads to an efficient algorithm for performing migration in 3D, which will allow for the possibility of using it for studies where CCP stacking was previously the only plausible approach.

In Chapter 4 we present a high-resolution migration image of the Cascadia subduction slab extending from 10km down to 450 km depth, based on this 3-D pre-stack Kirchhoff depth migration (PKDM) method for teleseismic receiver functions. As one of the most well-observed subduction zones in the world, extensive seismic studies have been done in Cascadia. These include teleseismic tomography [Obrebski et al., 2011; Hawley et al., 2016], regional tomography [Gao, 2016; Bell et al., 2016], receiver functions [Audet et al., 2009; 2010], seismic anisotropy [Martin-Short et al., 2015], reflection imaging offshore [Han at al., 2016] and seismicity studies [McCrory et al., 2012a]. All these studies provide strong constraints on the geometry and physical properties of the subducting slab and surrounding mantle. However, the geometry of the slab in the deep mantle, and the chemical composition of the slab remain controversial due to the complexity. We combine the primary Ps arrival, multiple arrivals, and account for the 3D velocity variations to provide a 3D discontinuity model that has advantages over previous studies [e.g., Sheehan et al., 2000; Levander and Miller, 2012; Tauzin et al., 2013]. This work differs from previous receiver function studies in a number of ways. First, in this study we present a 3D migration model of the dipping slab for the first time, while previous studies have only provided 2D section [e.g. Bostock et al. 2013]. Benoit et al. [2013] provide a 3D model, however, the image obtained using CCP stacking, which is severly limited for dipping structures. Second, we carefully analyze the model and distinguish multiple signals from the primary. The discontinuity in the 3D image volume is well resolved in this study allowing us to recognize that the dominant seismic conversion structure inside the subduction oceanic crust varies anomalously along the strike of the subduction zone from the Gorda Plate to Juan de Fuca Plate.

Our Kirchhoff migration approach applied to the Cascadia subduction slab is also not a perfect image. First, the image does not take advantage of the full spectrum of information in the data. Second, the image is contaminated by multiples. In chapter 5 we explore possible ways to improve the imaging drawing on techniques used in oil and gas exploration. We show the concept of using least-squares migration (LSM) to tackle some of the problems and apply it to reflection data. Least-squares migration (LSM) has been proposed to seek an inverted image, which generates the simulated data best matching the amplitude of the seismic data. The idea of LSM was first applied to Kirchhoff migration then generalized to one-way wave equation migration and is now applied to reverse time migration (RTM). It can remove the data collection footprint, remove the source effect and improve the migration image quality. We show the successful application to the seismic reflection data and speculate about the potential to apply it in large continental scale imaging.

In this dissertation, I hope to have answered some scientific questions and provide new ideas about physical processes within the Hawaii plume and Cascadia subduction system from a seismology perspective. Hopefully the techniques presented in this thesis will have further applications and can provide directions for future research.

Chapter 2

Investigation of Hawaii plume with finite-frequency tomography

2.1 Abstract

It is generally accepted that mantle plumes are responsible for hotspot chains, and as such provide insight to mantle convection processes. Among all the hotspots, the Hawaii chain is a characteristic example that has been extensively explored. However, many questions remain. If a plume does exist beneath the Hawaii Island chain, what is the shape, size and orientation of the plume conduit? To what extent can the seismic structure of the plume be mapped? Can we see a continuous plume conduit extending from the lower to the upper mantle? At what depth do melting processes occur? Here, we combine constraints from three data sets (body waves, ballistic surface waves and ambient noise) to create 3D images of the velocity structure beneath the Hawaiian island chain from a depth of ~800 km to the surface. We use data from the Hawaiian Plume Lithosphere Undersea Melt Experiment (PLUME), which was a network of four-component broadband ocean bottom seismometers that had a network aperture of ~1000 km. Our multiphase 3D model results indicate there is a large deep-rooted low velocity anomaly rising from the lower mantle. At transition zone depths the conduit is located to the southeast of Hawaii. A 2% S-wave anomaly is observed in the core of the plume conduit around 700 km depth which, once corrected for damping effects, suggests a 200-250°C temperature anomaly assuming a thermal plume. In the upper mantle, there is a horizontal plume "pancake" at shallow depths beneath the oceanic lithosphere, and there is also a second horizontal low-velocity layer in the 250 to 410 km depth range beneath the island chain. This second layer is only revealed after surface wave phase velocity data are incorporated into the inversion scheme to improve the constraints on the structure in the upper ~200 km. We suggest this feature is a deep eclogite pool (DEP), an interpretation consistent with geodynamic modeling [Ballmer et al., 2013]. The model also shows reduced lithospheric velocities compared to typical ~100 Myr old lithosphere implying lithospheric rejuvenation by the plume. In addition, a shallow (~20 km) low velocity anomaly is observed to the southeast of the Big Island. This suggests newly modified lithosphere as might be expected in the location of an emerging new island in the Hawaiian island chain.

2.2 Introduction and motivation

The Hawaii island chain is an ideal place to study intraplate hotspots. Many researchers consider it to be a case example of a deep-rooted whole-mantle plume [Morgan, 1971]. While a plume origin is broadly accepted, there is an ongoing debate about the morphology of the plume system including the depth of origin, and direction from which the plume originates if it is not vertical. The structure of the plume in the upper mantle and how it interacts with the overriding lithosphere of the Pacific Plate is also an open question with a variety of geochemical interpretations [e.g. Lassiter et al., 1996; Abouchami et al., 2005; Huang et al., 2011; Weis et al., 2011] and geodynamical models attempting to predict the possible interactions [e.g. Detrick and Crough, 1978; Monnereau et al., 1993; Farnetani et al., 2009, 2010, 2012; Rychert et al., 2013].

Seismic imaging techniques provide a powerful mechanism to constrain the 3D structure and origin of the island chain. There are several regional seismic studies of Hawaii, which are based on onshore station data [Woods and Okal, 1996; Priestley and Tilmann, 1999; Tilmann et al., 2001] or offshore station data [Wolfe et al., 2009, 2011; Laske et al., 2007, 2011]. Studies that rely exclusively on on-shore recorded data have a limited aperture (width) of the seismic array and the poor ray-path coverage makes it impossible to fully assess the deeper mantle structure. More recent regional studies instead make use of the offshore deployment of seismometers during the Plume and Lithosphere Undersea Melt Experiment (PLUME), which increases the aperture, and thereby constrains structure over a wider area at shallow depth, and also deeper into the lower mantle.

For example, Wolfe et al. [2009, 2011] use P- and S-wave arrivals from teleseismic earthquakes to image mantle structure to great depths and conclude that the plume stem extends into the lower mantle, with an origin to the southeast of Hawaii. SS precursor observations are consistent with this result [Schmerr et al., 2006, 2010]. However, imaging with inverse scattering of SS waves has been interpreted to suggest the presence of an 800- to 2000-kilometer-wide thermal anomaly in, and immediately below, the transition zone 1000 km west of Hawaii [Cao et al., 2011]. The conclusion drawn is that hot material does not rise from the lower mantle through a narrow vertical plume, but instead accumulates near the base of the transition zone before being entrained into flow toward Hawaii. Cao et al. [2011] also find a thinned transition zone to the southeast of Hawai‘i, but disregard it as the estimated excess temperature is too low, and is lower that the 300-400°C estimated excess temperature for the anomaly to the west. Laske et al. [2011] analyze Rayleigh waves recorded across the PLUME network at frequencies between 10 and 50 mHz thereby constraining structure in the upper 100-200 km. Their study reveals lithospheric rejuvenation within an area likely confined to within 150 km of the island chain.

In an effort to better constrain the 3D structure of the upper mantle beneath Hawaii we combine body- and surface-wave observations using a joint inversion scheme [Obrebski et al., 2011] and a finite frequency kernel approach. Our approach uses teleseismic body-wave traveltime measurements and surface-wave phase velocity information from ballistic surface waves and ambient noise cross-correlation measurements. All constraints are jointly inverted to obtain a multiphase tomographic

shear-wave velocity model. The resulting model constrains structure from the surface down to ~800 km depth. It is simultaneously consistent with all the seismic observations, meaning that it takes advantage of the surface wave constraints to resolve shallow (<200km) structure, while being consistent with teleseismic traveltimes that are able to constrain deeper structure.

2.3 Data and methodology

2.3.1 PLUME dataset

The PLUME experiment included a large network of four-component broadband ocean bottom seismometers (OBSs) occupying more than 70 sites and having an overall aperture of more than 1000 km [Laske et al., 2009]. PLUME was designed as a tool to determine the deep mantle seismic velocity structure beneath the Hawaiian hotspot island chain. PLUME was a two-year deployment that ran from January 2005 through June 2007. The first stage of this deployment was a 500-km-wide ocean bottom seismometer (OBS) network with inter-station spacing of ~80 km, where data was recorded continuously from January 2005 through January 2006. In the second stage of the deployment, the OBSs occupied a 1000 km wide region with station spacing of about 220 km from April 2006 through June 2007. In this two-phase deployment, data from the broadband sensors had undetermined orientations.

The first step in our processing is orienting the PLUME OBS horizontal components using teleseismic P-wave particle motions. Generally, our method produces stable and reliable orientations (average standard deviation is about 6 degrees) over a wide range of earthquake back-azimuths. To maximize the signal to noise ratio (SNR) we began by applying a 0.04-0.1 Hz bandpass filter and measured ~1100 P-wave relative arrival times on vertical component data. These P-wave measurements were used to determine orientations. We compared our estimated orientations with those determined using surface-waves and found them to be consistent. Once these data were rotated to radial and transverse orientations, ~750 S-wave relative arrival times (including direct S and SKS phases) were determined from the SV component via multi-channel cross correlation. Of these, we selected 75 events distributed in as wide a range of back azimuth directions as possible (Fig. 2.1), restricting the data to events with epicentral distances greater than 30 degrees and M_w greater than 5.5. As part of the waveform-by-waveform quality control, arrivals were picked manually using the Antelope dbpick software. This software has an interface for viewing waveform data and the ability to pick arrival times and provides markers that are then used as a starting point for the cross correlation step. We use a multi-channel least squares cross-correlation approach [VanDecar and Crosson, 1990] that results in a relative travel-time delay dataset. We select only the highest quality data based on the standard deviation of the cross-correlation-derived delay times to make sure that our body-wave data set contains reliable shear arrivals [Obrebski et al., 2011].

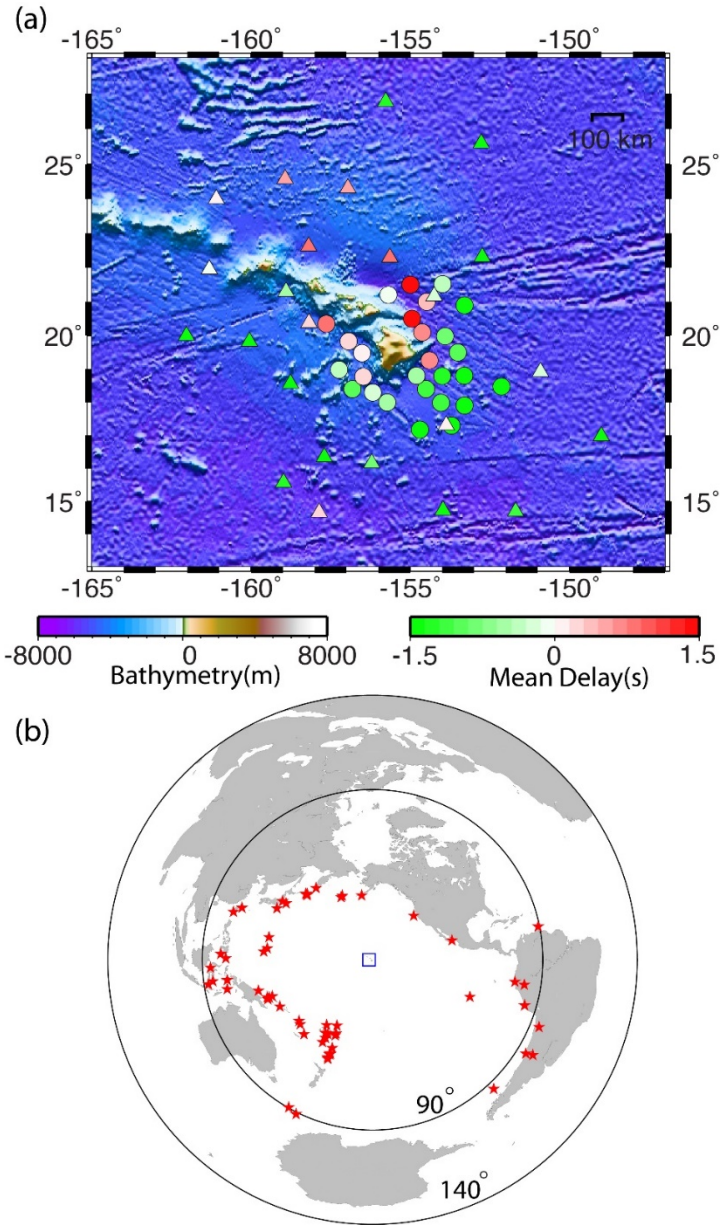

Figure 2.1: Map of the study area. (a) Ocean bathymetry showing seismometer locations. Stations deployed in the first year are indicated by circles and those deployed in the second year are marked by triangles. The station colors indicate the mean body-wave delays (measured at 0.04–0.1 Hz). Only stations that successfully recorded data are shown. (b) Map of earthquakes (red stars) used in this study and our study location (blue box). Black circles are 90° and 140° from the study region.

2.3.2 Joint body wave and surface wave inversion

The surface-wave phase data we use here come from two different sources. The first is ambient noise cross-correlation measurements in the period band of 10 to 25 sec. Due to the relatively high noise environment of OBS data, a linear stack of ~1 year of ambient noise Empirical Green's Function results is still rather noisy, which makes accurate measurements of surface wave phase velocity difficult. To reduce this problem, we apply a time-frequency domain Phase Weighted Stacking (tf-PWS) method [Schimmel and Gallart, 2007; Schimmel et al., 2011], which efficiently increases the SNR. The tf-PWS is an extension of the phase weighted stack method that is a non-linear stack where each sample of a linear stack is weighted by an amplitude-unbiased coherence measure. The idea here is leveraging the time-frequency phase stack, which is based on the time-frequency decomposition of each trace obtained through the S-transform. The results before and after applying the tf-PWS differ significantly (Fig. 2.2) and the number of visible dispersion curves within each period band after implementing the tf-PWS is greatly increased. From our time-frequency analysis we observe two wave trends with different travel times (Fig. 2.2). The T1 phase is the surface wave energy and T2 phase is the acoustic wave propagating in the water.

The second source of phase velocity measurements comes from ballistic surface waves. These are the direct surface wave energy as opposed to scattered energy including ambient noise. We use a two-plane wave tomography method [Forsyth and Li 2005; Yang and Forsyth 2006a; Yang and Forsyth 2006b] in the period band of 25 to 100 sec. Different from the traditional two-station one plane wave method, our method uses the amplitude and phase information simultaneously and the interference of two plane-waves to model each incoming teleseismic wavefield. This approach can account for the scattering and multipathing caused by lateral heterogeneities, and was developed to image regional scale structures with network apertures typically up to 1000 km like PLUME. This method has been applied successfully in various regions with a similar network configuration as ours [e.g. Yang and Forsyth 2006b; Yang et al., 2008]. Using the same methodology, we derive phase velocity at a variety of period bands from 25s to 100s.

In order to simultaneously invert the phase velocity constraints with the body-wave relative traveltime constraints we must determine phase velocity anomaly constraints. This is achieved by subtracting the phase velocities calculated for a background model from the absolute phase velocities. We explored the use of several background models and compared resulting velocity structure at different crustal depths. We found only slight differences in the models indicating that the choice of background model used doesn't significantly alter our results. Given this, we used the global average ocean PREM model as the background model.

Following Obrebski et al. [2011] we create a joint matrix of body wave relative travel time anomalies and the surface wave phase velocity anomalies to use in a joint inversion. The model space extends from 165°W to 145°W and 12°N to 28°N and to a depth of 1000 km. The model grid includes 33 nodes in both the horizontal and vertical directions, yielding a grid spacing of ~30km and ~55 km in the vertical and horizontal directions, respectively. The relative body-wave delays are inverted using finite-frequency sensitivity

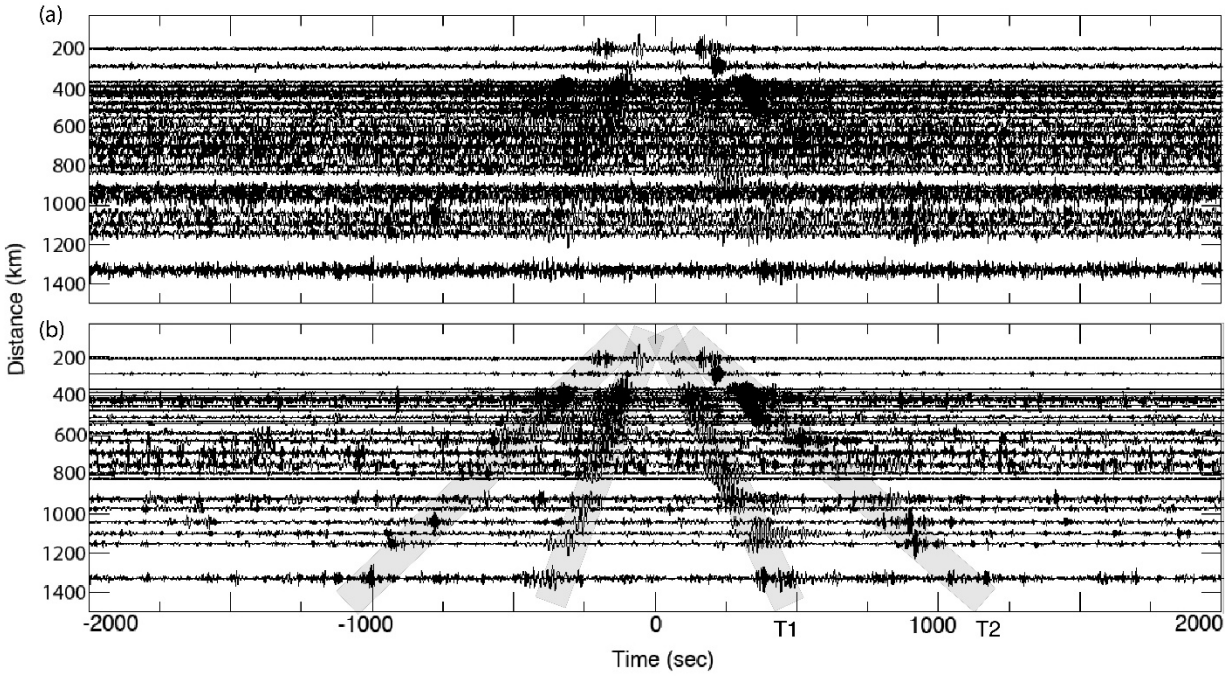

Figure 2.2: Seismic record sections. (a) Record section of the ambient noise cross-correlation between station PL41 and other stations derived using a traditional linear stacking method. (b) The same record section as shown in (a) except derived using a phase weighted stacking method [Schimmel and Gallart, 2007, 2011]. Boxed phases, labeled T1 and T2, are surface waves and acoustic waves propagating in the water column, respectively.

kernels that account for the frequency dependent width of the region to which body waves are sensitive and also accounts for wave front healing effects. Our tomographic method uses paraxial kernel theory to calculate the Born approximation forward-scattering sensitivity kernels for teleseismic arrival times [Dahlen et al., 2000; Hung et al., 2000; Hung et al., 2004]. The surface wave matrix is made of relative phase velocities estimated for 15 frequencies (10s, 12s, 15s, 18s, 20s, 22s, 24s, contributed from ambient noise; 25s, 29s, 33s, 40s, 50s, 66s, 83s, 100s, contributed from ballistic surface waves) at each node, which constrain the velocity structure from 0 to 300 km depth. To weight the body wave and surface wave constraints in the joint matrix, we use the same weighting scheme as Julia et al. [2000] and Obrebski et al. [2011]. They define the parameter p in their weighting formula, which allows for a manual tuning of the relative contribution of each dataset. After experimentation with various values of p, we settled on using a value of 0.7 as optimal. The sensitivity of very shallow (<60 km) velocity structure to the body-waves is also reduced through a ramp parameter. This is set to zero at the surface and increases linearly to 1 at 60 km depth. This is a multiplicative factor applied to the body-wave kernels to prevent the body-waves from introducing very short wavelength (one station spacing) velocity anomalies at shallow depths where the ray paths are vertical and there is no resolution. The shallowest part of our model is therefore entirely determined by surface wave data constraints. Station terms and event corrections are also included in the inversion. Our inversion requires damping and uses LSQR [Paige and Saunders 1982] to iterate to a final model. We also apply a smoothing factor to the model space. To choose the inversion damping parameter, we examine the residual misfit curves as a function of the model norm and find 0.2 is the best damping factor for our inversion scheme.

2.4 Image results

As a first reference model we produce a smoothed 3D model derived using inversion of only the SV body wave travel-times, which we refer to as HW13-SV (Figs. 2.3, 2.5b, 2.5e). The structure is very similar to the teleseismic body wave result of Wolfe et al., [2009], as we would expect. We observe a fairly continuous low-velocity feature extending from the surface down through the transition zone and into the deep mantle (Figs. 2.3, 2.5b). We interpret this as a plume conduit, the main stem of which comes from the mantle to the southeast of the surface islands. In the upper mantle, low velocities are observed over a wider region extending the length of the island chain and from the surface down to ~400 km depth. We interpret this low-velocity body as the present day plume "pancake", i.e. the low velocity material that is spreading horizontally beneath the oceanic lithosphere. What is surprising about this image is the fact that the low velocities of the plume pancake extend so deep, an observation also noted by Wolfe et al. [2009]. Both geodynamical models and previous tomographic observations of mantle plumes in oceanic settings suggest a much thinner sublithospheric plume pancake confined to the upper ~250 km [Ribe and Christensen, 1994; Allen et al., 2002; Farnetani and Hofmann, 2010].

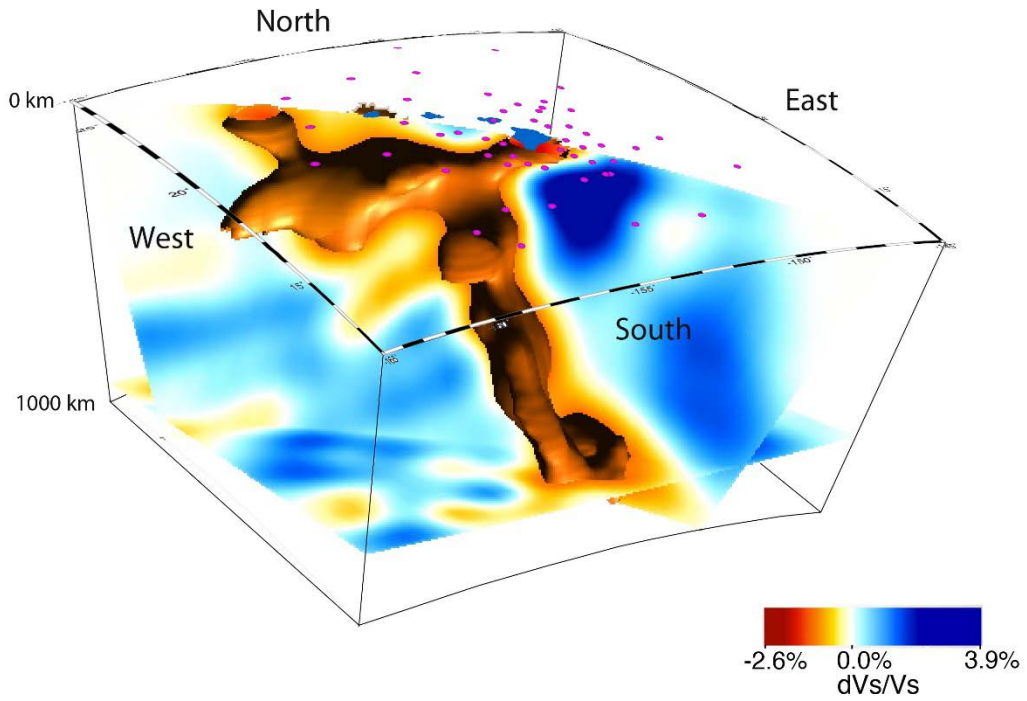

Figure 2.3: A 3D view of our body-wave only S-wave velocity anomaly model (HW13-SV) for the mantle beneath Hawaii. Warm colors indicate low velocity anomaly and cool colors indicate high velocity anomaly. The value of the isosurface is -1.5%. The model reveals a low-velocity region elongated in the sub-vertical direction from the base of the model extending up into the uppermost mantle. This feature is several-hundred kilometers wide and dips to the southeast. We interpret it as the plume conduit. In the upper mantle the low-velocity anomalies are predominantly horizontal and oriented parallel to the island chain. We interpret this as the plume "head", i.e. material that is being dragged along with and beneath the Pacific lithosphere.

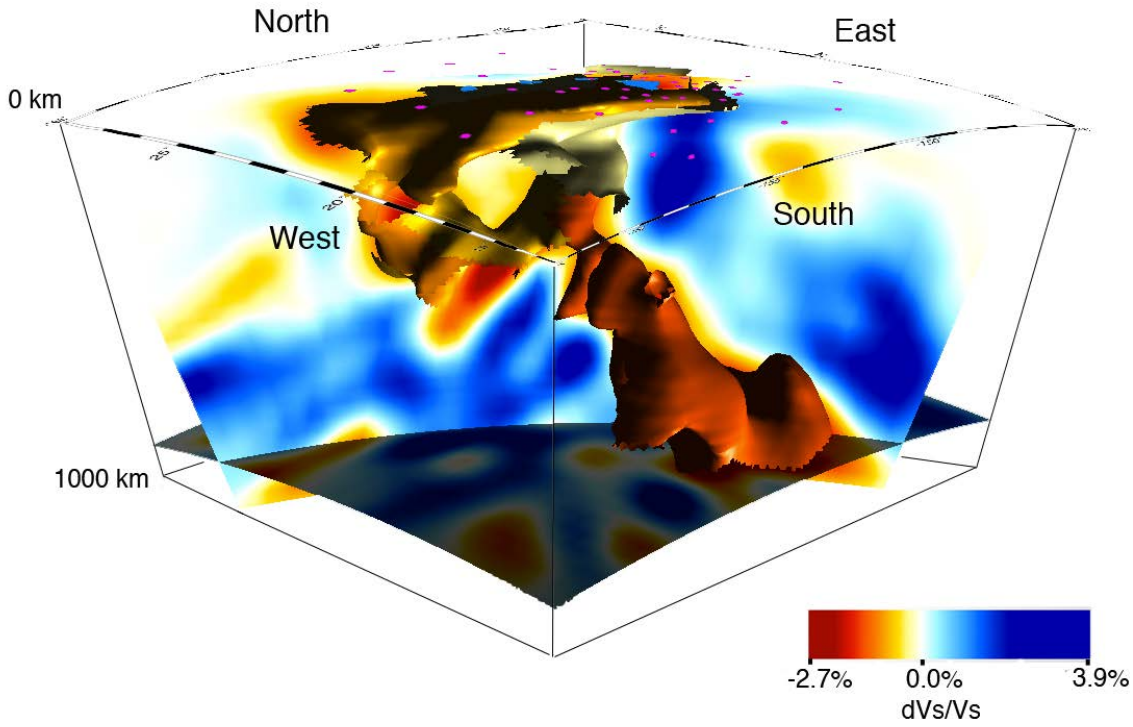

Figure 2.4: A 3D view of our body wave and surface wave joint S-wave velocity anomaly model (HW13-SVJ). This is shown with a similar perspective to the 3D image of HW13-SV in Fig. 2.3. The model shows what is interpreted as the plume conduit extending from the lower mantle southeast of Hawai‘i, up into the upper mantle beneath Hawai‘i. In the upper mantle two sub-horizontal plume pancakes are observed. The shallow pancake is clearest and extends beneath the lithosphere to a depth of 150km. The second pancake is less continuous, but forms a sub-horizontal layer in the 250 to 400 km depth range. We interpret this as the deep ecologite pool (DEP). This feature is revealed in the joint inversion due to the improved resolution in the upper mantle.

In an effort to better resolve this unusual structure in the upper mantle we complete the joint inversion of body- and surface-wave constraints, which we refer to as HW13-SVJ (Figs. 2.4, 2.5c, 2.5f, 2.6). This model retrieves a more complex velocity structure in the upper mantle than HW13-SV (Figs. 2.3, 2.5b, e), as would be expected given the additional constraints. The upper mantle low velocity feature is now observed to separate into two sub-horizontal layers. The first is shallow and immediately beneath the oceanic lithosphere, and extends to ~150 km depth. The depth extent is clearest in Fig. 2.5c and its lateral extent beneath and along the island chain is shown in Fig 2.6b. The second layer is in the depth range of ~250-400 km and is somewhat less continuous in the horizontal direction than the shallow layer (Figs. 2.4, 2.5c and 6d), but is distinct from and is not continuous with the shallow layer as illustrated by the absence of significant low-velocities at 200 km depth (Fig. 2.6c). This deeper low-velocity anomaly is less continuous beneath the island chain than the shallow anomaly (compare Figs. 2.6b and 2.6d). Finally, our seismic model also shows an apparent asymmetry in the low velocity structure of this second layer, which may be related to geochemical differences between the Loa and Kea trends observed at the surface [Ballmer et al., this volume; Huang et al., 2011; Weis et al., 2011].

We also invert for absolute velocity using just the (ambient and ballistic) surface wave data in order to compare these absolute velocities with average Pacific velocity profiles. Absolute velocity profiles at three locations along the island chain are shown in Fig. 2.7. These profiles show that to the southeast of the island, out in front of the region of plume influence, the velocity structure is typical for 100 Ma lithosphere below ~75km depth. Beneath the islands we see evidence of a rejuvenated velocity profile. One inconsistency with previous surface-wave based studies is the fact that we do not see the peak of the low-velocity anomaly around 100 km depth centered to the west of the Big Island as suggested by Laske et al. [2011]. Instead, the velocity anomalies we image at these depths are aligned with and centered on the island chain which is consistent with crustal studies of the underplating process [Leahy et al., 2010], body-wave tomography [Wolfe et al., 2009, 2011], as well as the geometry and geoid anomaly of the Hawaiian Swell [Cadio et al., 2012]. We do see the low-velocity anomalies extending further to the west than to the east, which is consistent with a recent receiver function study suggesting that the melt path to the Big Island originates to the west [Rychert et al., 2013].

2.5 Resolution test

We explored the resolving capabilities of our models using several approaches. First, we show the ray density from the teleseismic body-wave dataset. Fig. 2.8 shows the region with highest ray density plotted in the same cross-sections as the model shown in Fig. 2.5. The coverage is densest immediately beneath the seismic network and to a depth similar to the maximum aperture of the network. The green dashed line outlines the region of dense coverage and is also plotted on the model in Fig. 2.5. Ray density is by no means a complete indicator of resolution (see following additional tests) and crossing rays are needed to resolve structure. However, it is an indicator of where there are many ray paths constraining the velocity structure.

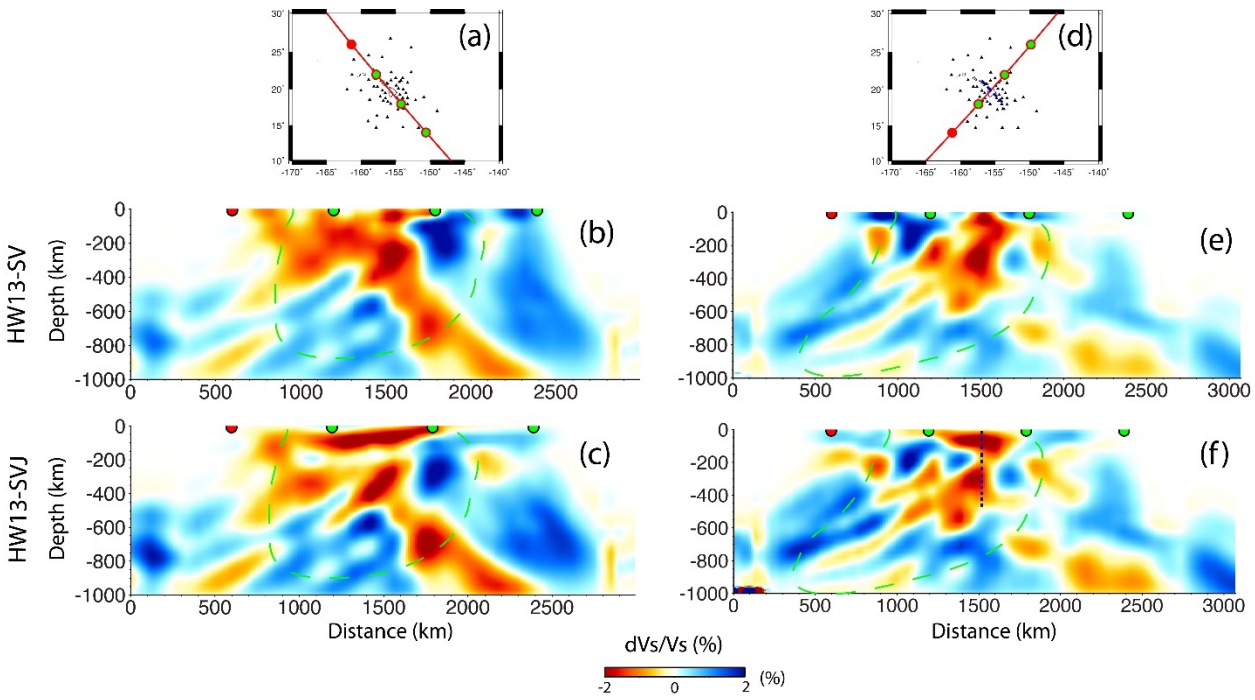

Figure 2.5: Vertical cross-sections through the HW13 models. Images (b-c) are cross-sections parallel to the Pacific plate motion; images (e-f) are cross-sections perpendicular to the plate motion. The locations and orientation of the cross-sections, along with the distribution of stations are shown in (a,d). Results (b) and (e) are from the body-wave-only inversion (HW13-SV), (c) and (f) are from the joint ambient noise, surface wave and body wave inversion (HW13-SVJ). The dash green contours encompass areas with highest teleseismic body wave ray coverage. The vertical dashed blue line on (d) is beneath the center of the island chain.

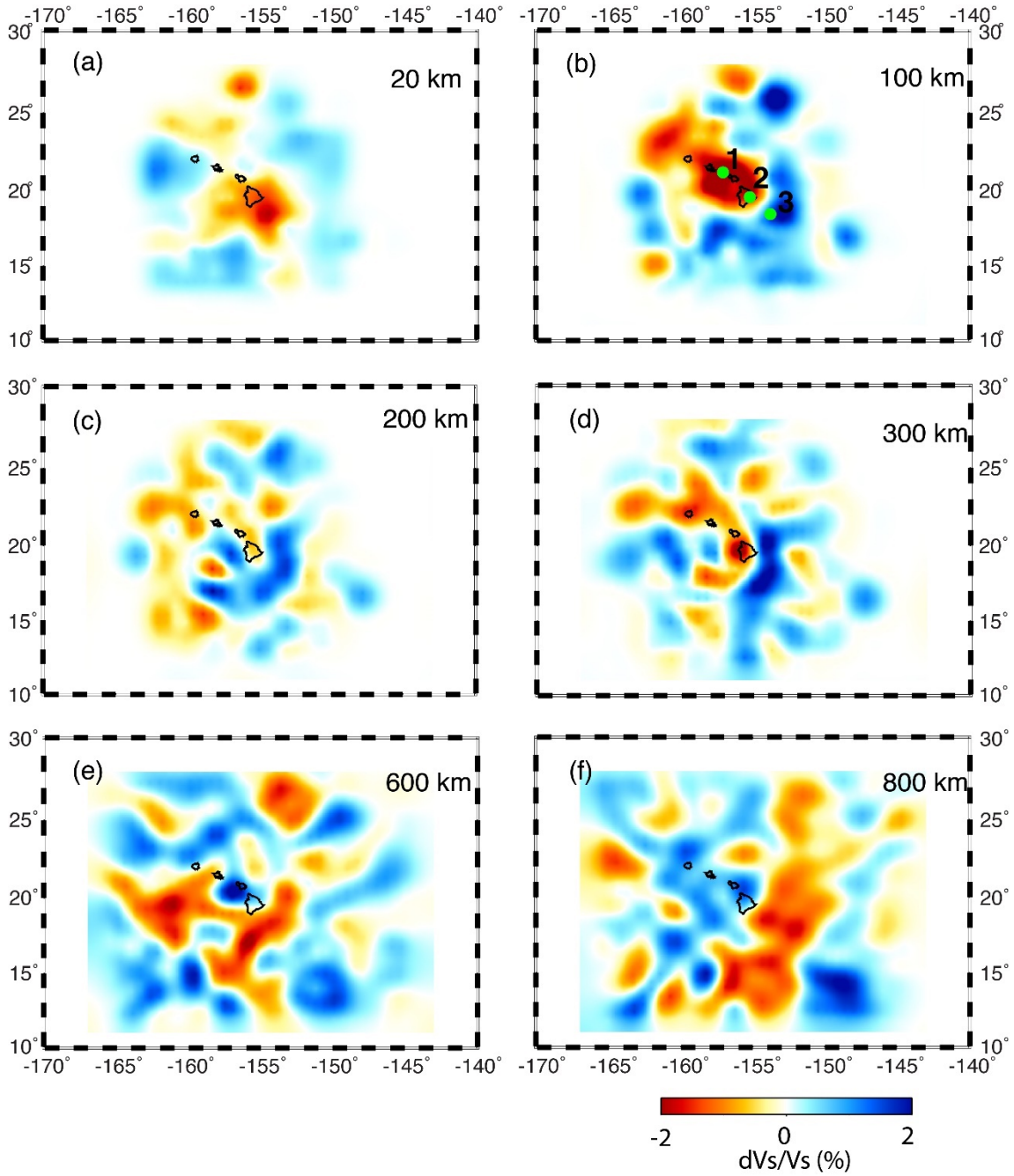

Figure 2.6: Maps of shear wave velocity perturbations in HW13-SVJ at (a) 20, (b) 100, (c) 200, (d) 300, (e) 600 and (f) 800km depth. Numbered green dots in sub-panel (b) are the locations of low velocity zone 1, low velocity zone 2 and high velocity zone 3 in Fig. 2.7.

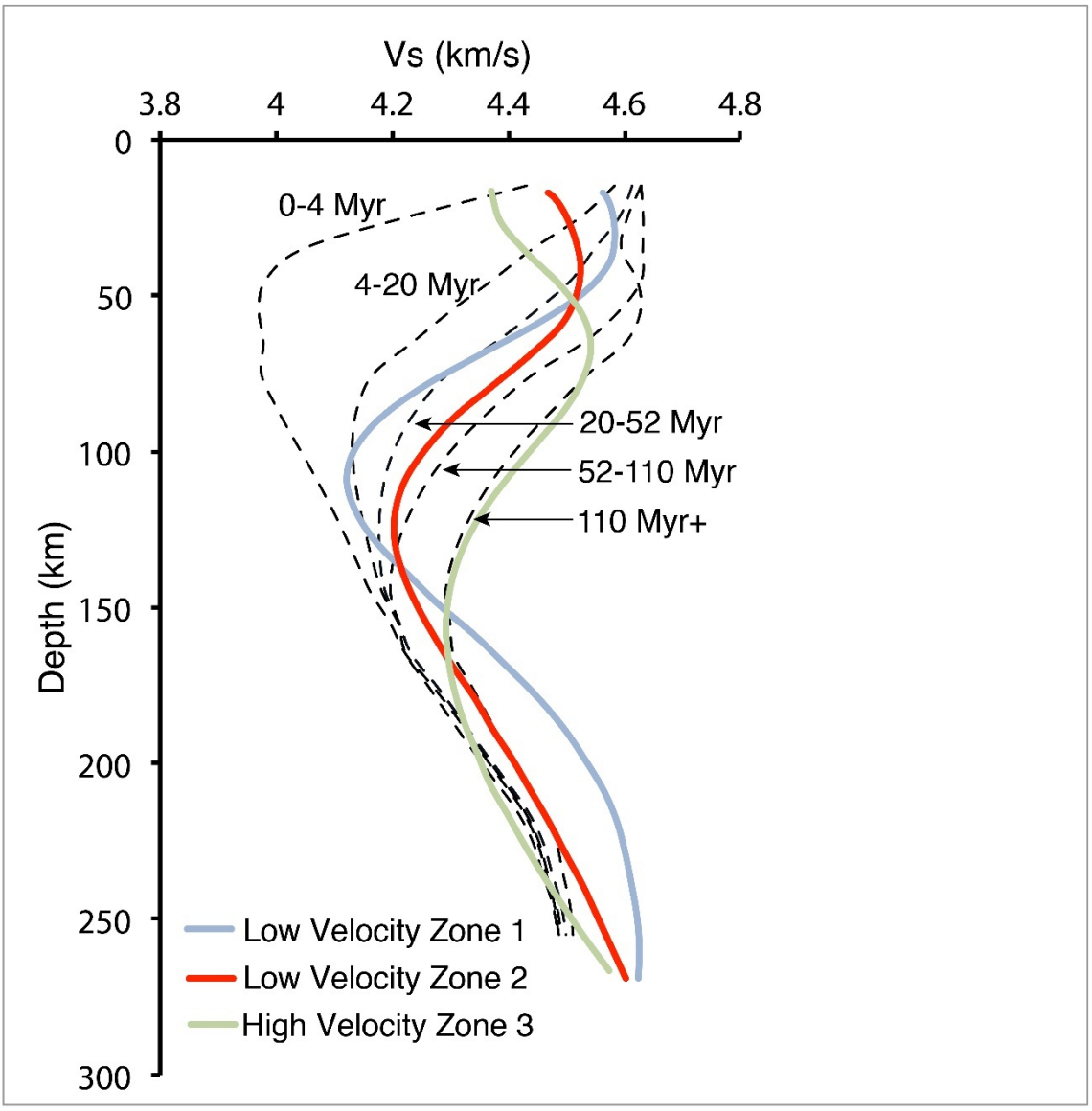

Figure 2.7: Upper mantle absolute velocity profile derived from ambient noise and surface wave inversions. The dash lines are average mantle velocity profiles for Pacific lithosphere with various ages [Nishimura and Forsyth, 1989]. The colored lines shows the velocity profiles at various locations along the length of the island chain and are indicated on Fig. 2.6b.

We next conduct checkerboard resolution tests using synthetic velocity models consisting of alternating high and low-velocity boxes. These synthetic velocity models are used to generate synthetic data, which is then inverted to assess the ability of the dataset to recover the synthetic models. Again, these types of tests are not perfect and do make the assumption that the finite frequency sensitivity kernels used are a "perfect" representation of the true sensitivity of the constraints. We do add 5% noise to the constraints to simulate errors and uncertainties in the measurements made. The recovered velocity models provide a guide to how the scale of structure that can be resolved varies as a function of position in the model. Resolution is possible on shorter scales at shallow depths, primarily due to the inclusion of surface waves, and structures must be larger to be constrained at greater depths. Fig. 2.9 shows that velocity anomalies ~200 km in diameter can be imaged in the upper ~250 km where surface waves provide constraints. At depths where the teleseismic body waves provide most constraint, i.e. from ~300 km to ~600 km, structures ~350 km wide are well recovered. Finally, in the uppermost lower mantle only structures ~450 km wide are recovered.

Finally, we construct a suite of synthetic velocity models to further test the ability of our dataset to resolve a variety of input velocity structures. We focus on the ability of the dataset to constrain vertical plume-like anomalies at a variety of depths. Fig. 2.10 shows the input and the recovered velocity structure for tests with a vertically oriented low-velocity anomaly 200 km wide and with a peak velocity anomaly of -4%. In the first test (Figs. 2.10a,e) the anomaly extends from 0 km to 300 km. The recovered velocity structure successfully captures the input structure in that the strongest low-velocity anomaly also extends from 0 to 300 km depth and has approximately the same width. The amplitude of the anomaly also approaches the input -4% at most depths. Ray-path smearing effects are also seen with high and low-velocity anomalies radiating down and outward from the input velocity structure. However, these smearing effects are all low amplitude with the largest streaking anomalies only being ~0.5%. Based on this test, we conclude that our model would show a strong velocity anomaly constrained to the upper 300 km if the true anomaly structure was only in the upper 300 km. Next we explore the possibility that the low-velocity anomaly is only deep, 350 to 650 km (Figs. 2.10b, f). Again the recovered velocity structure is largely constrained to the same depth range with less smearing than the first test. The amplitude recovery is reduced to -2 to -3% meaning that we only recover 50-75% of the velocity anomaly. Next we use a low-velocity anomaly that extends throughout the full depth range of the model (Figs. 2.10c, g) and find that this is also well recovered with only low-amplitude anomalies resulting from smearing of velocities along down-going ray paths similar to what was observed in the first test. The amplitude of the velocity anomalies in the input plume stem also decreases with depth in a similar fashion to the first two tests.

In the final test we use a synthetic velocity structure based on the "two-layer" geodynamic model for mantle flow beneath Hawaii developed by Ballmer et al. [2013]. We estimated the absolute velocities from the predicted temperature, density, and lithostatic pressure at each point of the quasi steady-state model using the relationships of Faul and Jackson [2005] and Jackson and Faul [2010] with specifications reported in Ballmer et al. [2013]. We then subtract the 1D reference velocity model to determine velocity anomalies for input into our synthetic test. The recovered structure is good beneath the seismic array including the variable size of the low velocity anomaly in the

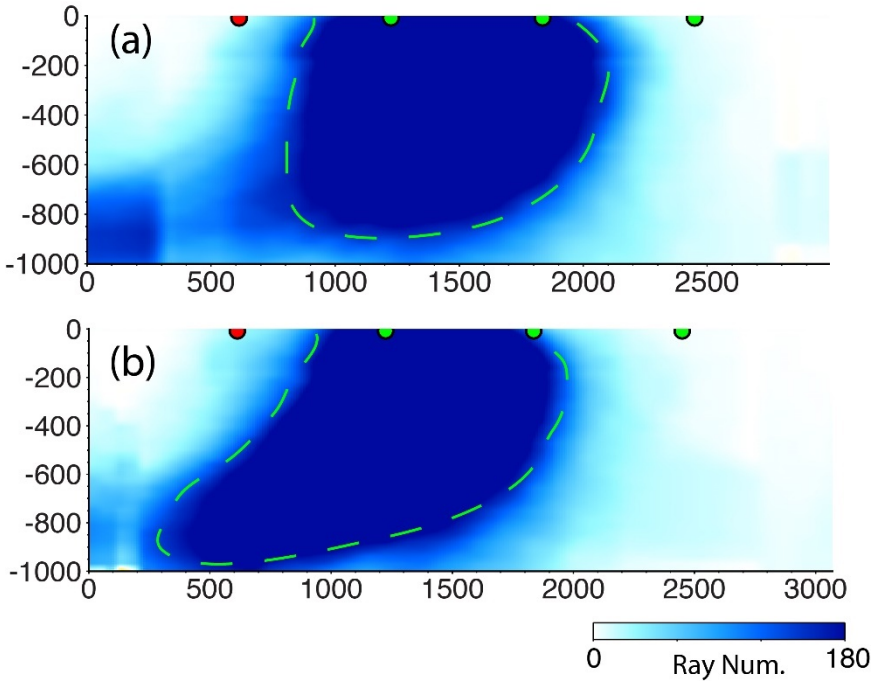

Figure 2.8: Vertical cross-section of ray density maps. (a) Cross-section that is parallel to the Pacific plate motion where the dash green dashed line encompasses areas with "high" ray coverage. This cross-section is the same as shown in Figs. 2.5 b-c. The color bar shows how many rays contributed to the velocity information at a particular model grid point. (b) Cross-section perpendicular to the Pacific Plate motion and the same as shown in Figs. 2.5 e-f.

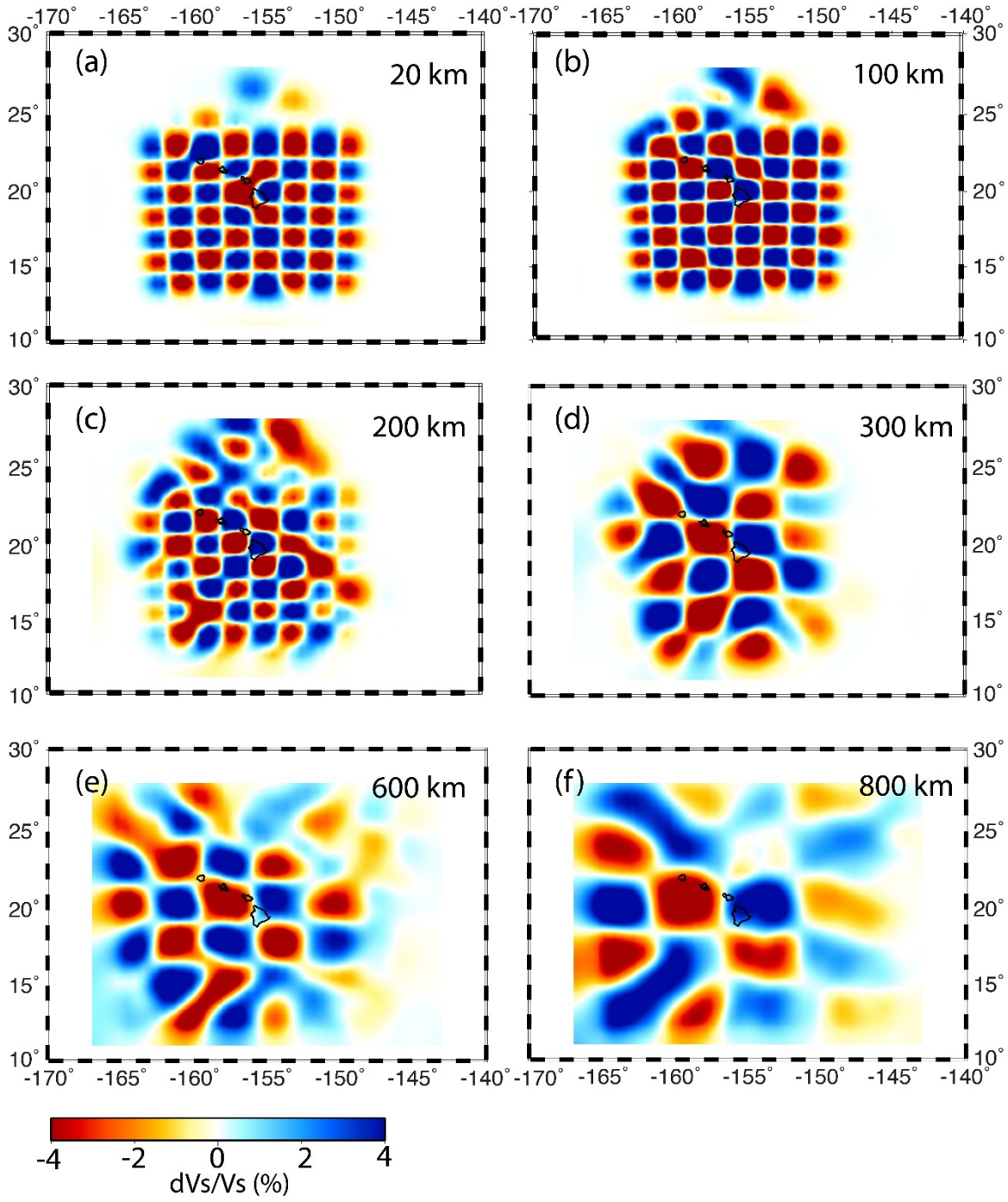

Figure 2.9: Checkerboard resolution tests for input (synthetic) velocities anomalies of ±4 percent. Horizontal slices through the recovered velocity anomalies are shown at depths of 20, 100, 200, 300, 600 and 800 km.

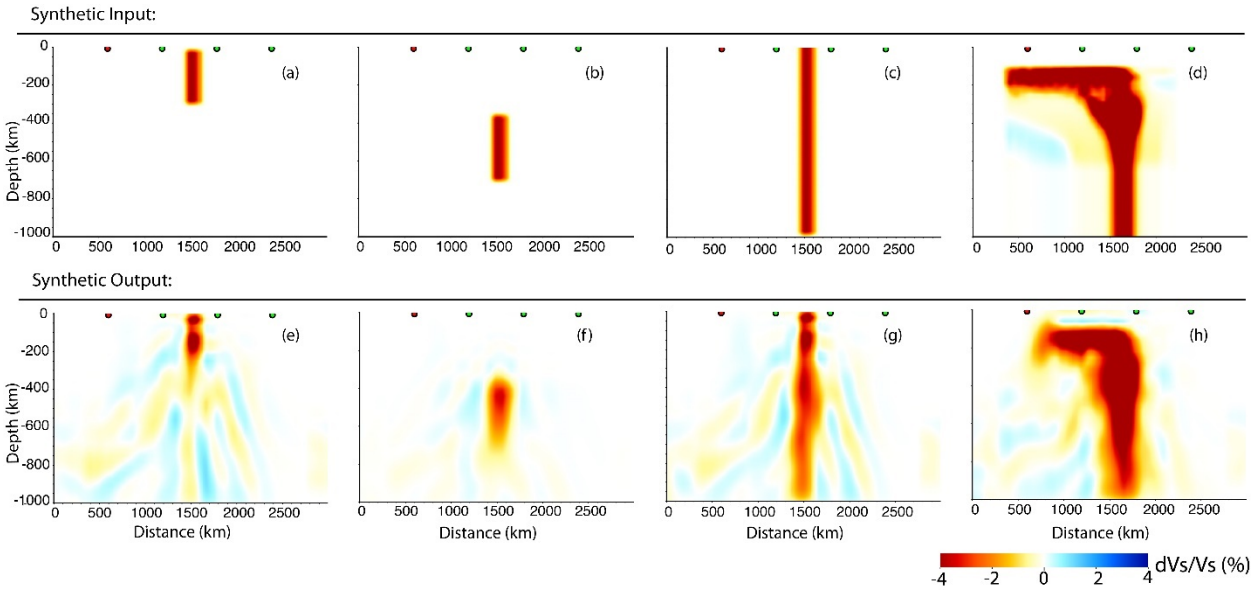

Figure 2.10: Synthetic resolution tests. (a-d) Vertical cross-sections through four synthetic input velocity models. (e-h) Recovered velocity structure. These tests include vertical columns in various depth ranges (a-c; e-g) and a test of the model structure expected for Ballmer et al.'s geodynamic model (d, h). The sections are all parallel to plate motion as in Fig. 2.5(b,c) and Fig. 2.8(a).

upper mantle associated with Ballmer's two-layer structure. These tests leave us confident that the upper-mantle structure is well resolved in our seismic inversion.

2.6 Discussion

2.6.1 Structure and origin of the plume conduit

Our imaging results suggest that a sub-vertically oriented low-velocity anomaly exists beneath Hawaii that extends through the upper mantle and down into the uppermost lower mantle. We interpret this feature as being indicative of a whole-mantle-plume source for the Hawaiian Island chain. This structure and interpretation is similar to the conclusion of Wolfe et al. [2009]. Both results reveal low velocities within the mantle transition zone and in the topmost lower mantle, suggesting there is a deep source region for the Hawaiian plume. A thermal boundary layer near the base of the transition zone has been suggested as a candidate source region for some plumes [e.g. Cserepes and Yuen, 2000]. However, our image does not support this hypothesis as we see no evidence of a broadening of the low-velocity anomaly beneath the 660km discontinuity as would be expected in that case.

We interpret our model to indicate that the plume conduit has an origin to the southeast of the Big Island. As shown by Figs. 2.5 and 2.6 there are several locations in the uppermost lower mantle that have low-velocities in our model. However, we interpret the anomaly to the southeast to be the plume conduit for three reasons. (1) The low-velocities in the SE quadrant are larger in size (lateral extent) and amplitude (see Fig. 2.6f) than any other quadrant reaching 2% when others are closer to 1%. (2) The smaller low-velocity anomalies seen in other quadrants are outside the region of dense ray coverage i.e. outside the green dashed lines in Fig. 2.5. (3) The anomalies extending to the southeast are the most continuous (Figs. 2.4 and 2.5). It is also worth noting that the teleseismic ray coverage is not dominated by rays coming from the southeast (Fig. 2.1b) so the plume conduit that we image/interpret is not due to a particularly dense ray bundle coming from that direction. Our observation that the plume origin is to the southeast is also consistent with geodynamic arguments that mantle convection in general, and the fast-moving Pacific plate in particular, shear and tilt the plume conduit in the upper and lower mantle [Richards and Griffiths, 1988; Steinberger and O'Connell, 1998; Steinberger et al., 2004; Farnetani and Hofmann, 2010].

Several previous studies have explored topography of the transition zone discontinuities in the region beneath Hawai'i in an effort to identify anomalies that may be related to the source of the islands. Shen et al. [2003] observe transition-zone thinning across a broad zone beneath the island chain, which they interpreted as reflecting higher-than-normal temperatures beneath the region due to the passage of plume material through the transition zone. In contrast, Li et al. [2000] and Wölbern et al. [2006] suggest that the transition zone is thinned ~200 km west of Hawai'i. In a study of SS precursors, Cao et al. [2011] argue that ponded plume material sits beneath the transition zone several degrees west of Hawai'i. Our imaging results do not support these observations, instead suggesting that the plume conduit is intersecting the transition zone ~200 km southeast of Hawai'i.

A number of factors can cause velocity heterogeneity in the mantle, including variations in temperature (with contributions from both anharmonic and anelastic components, e.g., Karato, 1993), water content [Karato, 2003], melt [e.g., Hammond and Humphreys, 2000], grain size [Faul and Jackson, 2005; Jackson and Faul, 2010], and bulk composition. The last factor includes depletion by melt extraction [Jordan, 1979], although recent studies suggest that the effects of depletion on P- and S-wave velocities and Vp/Vs ratios may be minor [Schutt and Lesher, 2006; Afonso et al., 2010]. In the uppermost lower mantle (~700km depth) the S wave velocity anomalies are around 2% in our model. As smoothing and damping are part of the inversion scheme, the velocity anomalies we obtain are minimum estimates [Allen et al., 2002]. From our synthetic tests (Fig. 2.10) we find that we recover about 50-75% of the anomaly at this depth, which implies the real velocity anomalies in the plume conduit likely exceed ~3% [Allen and Tromp, 2005]. These velocity anomalies imply an excess temperature of 200-250°C [Schilling et al., 1991; Allen et al., 2002], consistent with petrologic estimates [Herzberg et al., 2007].

2.6.2 Upper mantle structure and a double-layered plume

The low-velocity structure that we image in the upper mantle is in disagreement with the classic version of plume theory. The classic plume model [e.g. Morgan, 1972; Ribe and Christensen, 1994; Farnetani and Hofmann, 2010] involves a near-vertical plume conduit rising through the entire mantle and spreading at the base of the lithosphere to form a pancake of hot material. The main hotspot forms where the conduit feeds the pancake, which is dragged away by plate motion, to the northwest in the case of Hawai‘i. However, instead of a single shallow plume pancake, we image two distinct horizontal low-velocity layers in the upper mantle. One layer is at <150 km depth, and the second is in the ~250 to 400 km depth range. Whereas this study is the first to image two separate layers, it is consistent with a previous study from Wolfe et al. [2009], who have recovered one broad low-velocity body that extends from the base of the lithosphere to ~400 km depth.

Our imaged model structure is consistent with a recent geodynamic model [Ballmer et al., 2013] developed in an effort to explain the thick low-velocity body imaged by Wolfe et al. [2009]. While the model was developed simply to explain the existence of a plume pancake to ~400 km depth beneath the island chain, it also suggests a double-layer to the plume pancake as we observe. In Ballmer et al.'s model the plume is composed of 85% peridotite and 15% chemically dense eclogite. As the plume material rises through the upper mantle, it generates a "deep eclogitic pool" (DEP) at 300-410 km depth, from which a shallow upwelling rises further to feed the pancake [Ballmer et al., 2013]. The compositions used in the geodynamic model are based on geochemical constraints for Hawaiian lava composition, which is thought to contain mafic materials such as eclogites, in addition to peridotite [Hauri et al., 1996; Sobolev et al., 2005; Herzberg, 2011; Pietruszka et al., 2013]. These mafic materials likely originate from subducted oceanic crust that is entrained by the plume, and are denser than peridotite throughout the upper mantle. The ascent of a plume rich in eclogite is thus controlled by a competition between negative compositional and positive thermal buoyancy. In addition, it is affected by phase transitions in the upper mantle, which modulate the densities of eclogite and peridotite to cause a maximum of the excess density of eclogite at 300-410 km depth [Aoki and

Takahashi, 2004]. It is this excess density maximum, which causes the plume to stall and to form a "deep eclogitic pool" (DEP) [Ballmer et al., 2013]. When the material rising out of the DEP crosses the coesite-stishovite phase transition at 300 km depth [Aoki and Takahashi, 2004], the density of eclogite sharply decreases thereby inducing rapid upwelling in a narrow plume conduit. The predicted contrast between a wide DEP and a narrow shallow plume [Ballmer et al., 2013] compares well with our observations (Figs. 2.5, 2.6).

2.6.3 Plume interaction with the lithosphere

The age of Pacific plate around the Hawai'i islands is about 100 Ma [Müller et al., 2008]. Fig. 2.7 shows the typical velocity profiles for oceanic plate of different ages derived from surface wave measurements [Nishimura and Forsyth, 1989]. We determine the absolute velocity based on our surface wave constraints and compare them to the typical profiles at 3 different locations that span regions in both the low- and high-velocity portions of the lithosphere (green dots on Fig. 2.6b). Location 1 is halfway along the island chain, which is in the middle of the strong low-velocity anomaly at ~100 km depth. Location 2 is at the southwest coast of the Big Island and on the edge of the strong low-velocity anomaly. Location 3 is further southwest and "upstream" of the plume, outside the low-velocity region of the plume.

Compared to the typical 100 Ma lithosphere velocity profile that would be expected beneath Hawai'i, the velocity at location 1 is most reduced. The velocity reduction extends from the surface to ~140km, producing a velocity profile that is more similar to the typical profile for 20-52 Ma lithosphere. The velocity at location 2 is also reduced to ~140 km depth, but to a lesser extent. These observations are consistent with the concept of lithospheric rejuvenation [e.g. Detrick and Crough 1978; Von Herzen et al., 1989; Monnereau et al., 1993; Li et al., 2004]. Location 1 has been rejuvenated to a greater extend than location 2 as would be expected given that location 1 has been under the influence of the lithosphere-modifying plume for a longer time than location 2. Our observations are consistent with those of Laske et al. [2011]. We suggest rejuvenation of the lithosphere should be understood primarily as a velocity reduction in the lithosphere and not necessarily a mechanical thinning of the lithosphere.

Location 3 is 150 km southeast of the Big Island and is upstream of the plume. We therefore expect little or no rejuvenation effect. Below 75km depth the velocity profile at location 3 is very similar to the typical profile for 100 Ma lithosphere (Fig. 2.7). But the velocity is significantly reduced at shallower depths. The shallow low-velocity zone is also imaged in HW13-SVJ (Figs. 2.6a and 2.11). We are able to image this low-velocity anomaly at 20 km depth due to the inclusion of the higher frequency constraints from ambient seismic noise (down to 0.1 Hz) which have wavelengths of ~45km. These wavelengths are still too long to image magma chambers, so these shallow low velocities instead indicate a broad region of the lithosphere that must be modified to cause the reduction in velocity. The location of the shallow low-velocity anomaly is centered between earthquake swarms in the upper 30 km and the location of the Lō'ihi seamount (Fig. 2.11). We therefore propose that we are imaging evidence of shallow lithospheric modification in response to the arrival of the next volcano in the island chain.

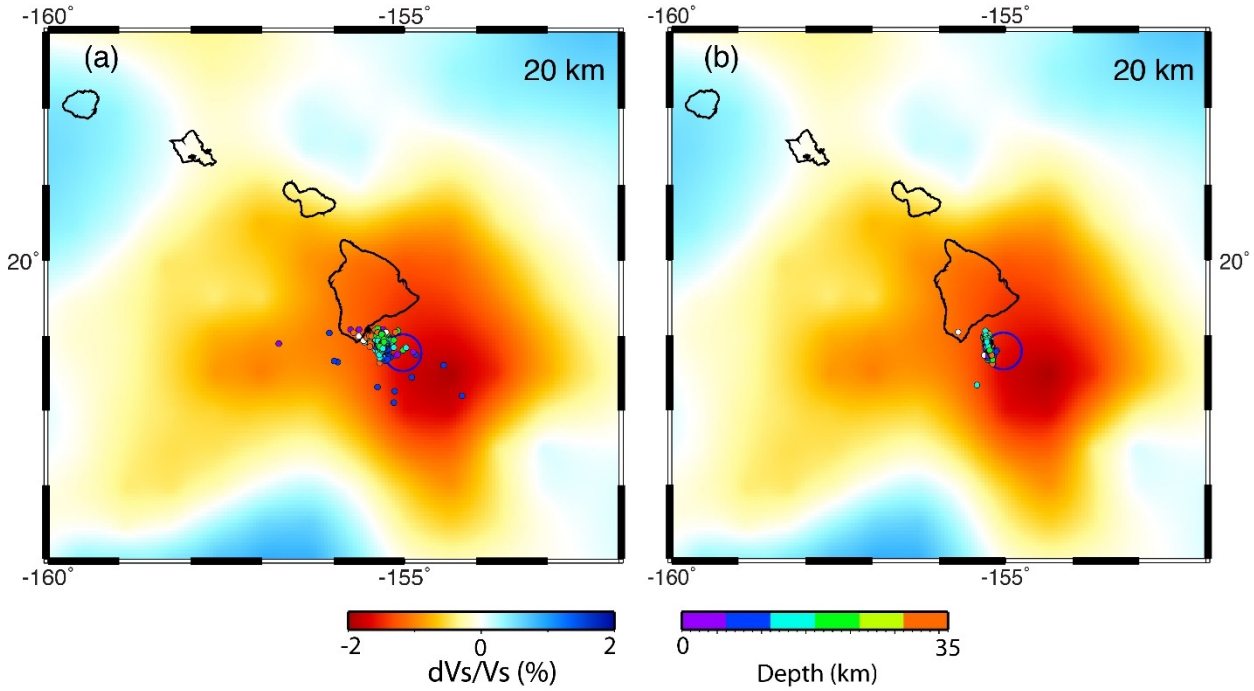

Figure 2.11: Map view of HW13-SVJ at 20 km depth with the location of earthquake swarms from (a) 1971 and (b) 1996, and the location of the Lō'ihi seamount (blue circle). The lower right color scale indicates earthquake depth and the lower left color scale indicates velocity perturbation in percent.

2.7 Summary

We derive a 3D model (HW13-SVJ) of the Hawaii plume extending from the lower mantle to the surface using a multi-constraint seismic tomography method that uses the PLUME OBS data. Checkerboard resolution tests and the synthetic tests suggest that the primary features in our model are robust to 800 km depth. Our results show that under the Hawaii hotspot a continuous low velocity anomaly extends from the roots of the volcanoes downward into the lower mantle. The plume origin is to the southeast of the island chain, which is consistent with what mantle flow models predict. The geometry of this low velocity body is consistent with a whole mantle plume feeding the hotspot in this region. The 2% low velocity anomaly in the lower mantle implies a 200-250°C temperature anomaly once corrected for damping and assuming a purely thermal plume. These modeled deep features are similar to prior body-wave tomography results [Wolfe et al., 2009; 2011].

The addition of surface wave phase velocity constraints from earthquakes and ambient seismic noise provides additional constraints in the upper mantle, including the lithosphere and crust, which are jointly inverted with the body-wave constraints. In the upper mantle, the structure of the low-velocity plume deviates substantially from the classic plume pancake model. Our model suggests the presence of two sub-horizontal low-velocity layers in the upper mantle. The first is immediately below the oceanic lithosphere, as expected. The second anomaly is directly above the 410km boundary and extends up to ~250 km depth. This secondary tomographic feature is consistent with geodynamic models of plumes with high eclogite content [Ballmer et al., 2013]. They predict a low velocity layer immediately above the 410 discontinuity, which is produced by the accumulation of eclogite. The model also suggests a lateral heterogeneity inside this low velocity layer that may be related to the observed geochemistry asymmetry at the surface [Ballmer et al., this volume].

At more shallow, lithospheric depths, our model shows lower velocities than expected for the ~100 Ma oceanic lithosphere. Instead the velocity profiles are more similar to Pacific lithosphere with a mantle age of 20 to 50 Ma. This is consistent with previous observations and interpretations of a rejuvenated lithosphere beneath the Hawaii Island [Laske et al., 2011]. Finally, at the shallowest depth (~20 km), we see a low velocity anomaly southeast of the main island that is likely indicative of the process of lithospheric modification beneath the next newly evolving island in the Hawaiian island chain.

2.8 Bibliography

Abouchami, W. (2005) Lead isotopes reveal bilateral asymmetry and vertical continuity in the Hawaiian mantle plume. *Nature* 434, 851-856.

Allen, R.M., Nolet, G., Morgan, W.J., Vogfjord, K., Bergsson, B.H., Erlendsson, P., Foulger, G.R., Jakobsdottir, S., Julian, B.R., Pritchard, M., Ragnarsson, S., and Stefansson, R. (2002) Imaging the mantle beneath Iceland using integrated seismological techniques, *J. Geophys. Res.*, 107, doi:10.1029/2001JB000595.

Allen, R.M., and Tromp, J. (2005) Resolution of regional seismic models: Squeezing the Iceland anomaly. *Geophys. J. Int.* 161, 373-386 doi: 10.1111/j.1365-246X.2005 .02600.x.

Afonso, J.C., Ranalli, J., Fernàndez, M.,Griffin, W.,O'Reilly, S.Y. and Faul, U. (2010) On the Vp/Vs–Mg# correlation in mantle peridotites: implications for the identification of thermal and compositional anomalies in the upper mantle. *Earth Planet. Sci. Lett.* 289, 606–618.

Aoki, I., and Takahashi, E. (2004) Density of MORB eclogite in the upper mantle. *Phys. Earth Planet. Inter*. 143–144, 129–143.

Ballmer, M., Ito, G., Wolfe, C., Solomon, S. (2013) Double-layering of a thermochemical Hawaiian plume in the upper mantle. *Earth Planet. Sci. Lett.*, 376, 155-164, doi: 10.1016/j.epsl.2013.06.022..

Ballmer, M., Ito, G., and Cheng, C. (2014). Asymmetric dynamical behavior of thermochemical plumes and implications for Hawaiian lava composition. In: Carey, R., Weis, D. & Poland, M. (eds.) *Hawaiian Volcanism: From Source to Surface*: *AGU Monograph*.

Cadio, C., M. D. Ballmer, I. Panet, M. Diament, and Ribe, N. (2012) New constraints on the origin of the Hawaiian swell from wavelet analysis of the geoid to topography ratio, *Earth Planet. Science Lett.*, 359, 40-54.

Cao, Q., Van der Hilst, R.D., De Hoop, M.V., and Shim, S.-H. (2011) Seismic Imaging of Transition Zone Discontinuities Suggests Hot Mantle West of Hawaii, Science 332, 1068, doi: 10.1126/science.1202731.

Cserepes, L. and Yuen, D.A. (2000) On the possibility of a second kind of mantle plume, *Earth Planet. Sci. Lett.* 183, 61-71.

Dahlen, F.A., Hung, S.H. and Nolet, G. (2000) Fre ´chet kernels for finite- frequency traveltimes–I. Theory. *Geophys. J. Int.*, 141, 157–174.

Detrick, R.S. and Crough, S.T. (1978) Island subsidence, hot spots, and lithospheric thinning, *J. geophys. Res.*, 83, 1236–1244.

Farnetani, C.G., and Hofmann, A.W. (2009) Dynamics and internal structure of a lower mantle plume conduit, *Earth Planet. Sci. Lett.* 282, 314-322, doi:10.1016/j.epsl.2009.03.035.

Farnetani, C.G., and Hofmann, A.W. (2010) Dynamics and internal structure of the Hawaiian plume, Earth Planet. Sci. Lett. 295, 231–240, doi:10.1016/j.epsl.2010.04.005.

Farnetani, C.G., and Hofmann, A.W., Class, C. 2012. How double volcanic chains sample geochemical anomalies from the lowermost mantle, *Earth Planet. Sci. Lett.* 259-360, 240-247, doi:10.1016/j.epsl.2012.09.057.

Faul, U.H. and Jackson, I., (2005) The seismological signature of temperature and grain size variations in the upper mantle, *Earth Planet. Sci. Lett.* 234, 119–134, doi:10.1016/j.epsl.2005.02.008.

Forsyth, D.W., and Li, A. (2005) Array-analysis of Two-dimensional Variations in Surface Wave Velocity and Azimuthal Anisotropy in the Presence of Multipathing Interference, in Seismic Earth: Array Analysis of Broadband Seismograms, (A. Levander and G. Nolet, ed.), *AGU Geophysical Monograph* 157, 81-97.

Hammond, W.C., Humphreys, E.D. (2000) Upper mantle seismic wave velocity: effects of realistic partial melt geometries. *J. Geophys. Res.* 105, 10975–10986.

Hauri, E.H., J.C. Lassiter, and D.J. DePaolo (1996) Osmium isotope systematics of drilled lavas from Mauna Loa, Hawaii, *J. Geophys. Res.*, 101(B5), 11793–11806, doi:10.1029/95JB03346.

Herzberg, C., Asimow, P.D., Arndt, N., Niu, Y.L., Lesher, C.M., Fitton, J.G., Cheadle, M.J., Saunders, A.D. (2007) Temperatures in ambient mantle and plumes: constraints from basalts, picrites, and komatiites. *Geochem. Geophys. Geosyst.* 8, 34.

Herzberg, C. (2011) Identification of Source Lithology in the Hawaiian and Canary Islands: Implications for Origins, *Journal of Petrology*, 52, 113-146.

Huang, S., Hall, P.S., Jackson, M.G. (2011) Geochemical zoning of volcanic chains associated with Pacific hotspots. *Nature Geoscience*. 4, 874-878.

Hung, S.H., Dahlen, F.A. and Nolet, G. (2000) Fre´chet kernels for finite- frequency traveltimes–II. Examples, *Geophys. J. Int.*, 141, 175–203.

Hung,S.H., Shen,Y. and Chiao,L.Y. (2004) Imagingseismicvelocitystructure beneath the Iceland hot spot: a finite frequency approach, *J. Geophys. Res.*, 109, B08305, doi:10.1029/2003JB002889.

Jackson, I., and U. H. Faul (2010) Grainsize-sensitive viscoelastic relaxation in olivine: Towards a robust laboratory-based model for seismological application, *Phys. Earth Planet. Inter.*, 183, 151–163, doi:10.1016/j.pepi.2010.09.005.

Jordan, T.H. (1979) Mineralogies, densities, and seismic velocities of garnet lherzolites and their geophysical significance. In: Boyd, F.R., Meyer, H.O.A. (Eds.), The Mantle Sample: Inclusions in Kimberlites and other Volcanic, *American Geophysical Union*, Washington, D.C., pp. 1–14.

Julia, J., Ammon, C.J., Herrmann, R.B. and Correig, A.M., (2000) Joint in- version of receiver function and surface wave dispersion observations, *Geophys. J. Int*., 143, 99–112.

Karato, S. (1993) Importance of anelasticity in the interpretation of seismic tomography. *Geophys. Res. Lett*. 20, 1623–1626.

Karato, S. (2003) Mapping water content in the upper mantle. In: Eiler, J.M. (Ed.), Inside the Subduction Factory. *Geophys. Monograph* 138. American Geophysical Union, Washington, D.C., pp. 135–152.

Kurz, M.D., Jenkins, W.J., Hart, S.R. and Clague, D. (1983) Helium isotopic variations in volcanic rocks from Loihi Seamount and the island of Hawaii, *Earth Planet. Sci. Lett*., 66, 388–406.

Kurz, M. D., J. Curtice, D. E. Lott III, and A. Solow (2004) Rapid helium isotopic variability in Mauna Kea shield lavas from the Hawaiian Scientific Drilling Project, *Geochem. Geophys. Geosyst*., 5, Q04G14, doi:10.1029/2002GC000439.

Laske, G., Phipps Morgan, J. and Orcutt, J.A. (2007) The Hawaiian SWELL pi-lot experiment: evidence for lithosphere rejuvenation from ocean bottom surface wave data, in Plates, Plumes and Planetary Processes, Special Paper 430, pp. 209–233, eds Foulger, G.R. and Jurdy, D.M., Geological Society of America, Boulder, CO.

Laske, G., Collins, J.A., Wolfe, C.J., Solomon, S.C., Detrick, R.S., Orcutt, J.A., Bercovici, D. and Hauri, E.H. (2009) Probing the Hawaiian hot spot with new broadband ocean bottom instruments, *Eos Trans. Am. geophys. Un*., 90, 362–363.

Laske, G., Markee, A., Orcutt, J.A. Wolfe, C.J., Collins, J.A., Solomon, S.C., Detrick, R.S., , Bercovici, D. and Hauri, E.H. (2011) Asymmetric Shallow Mantle Structure beneath the Hawaiian Swell-Evidence from Rayleigh Waves Recorded by the PLUME network. *Geophys. J. Int.*, 187, 1725-1742.

Lassiter, J.C., DePaolo, D.J., Tatsumoto, M. (1996) Isotopic evolution of Mauna Kea volcano: Results from the initial phase of the Hawaiian Scientific Drilling Project. *J. Geophys. Res.* 101, 11769-11780.

Leahy, G.M., J.A. Collins, C.J. Wolfe, G. Laske, S.C. Solomon (2010) Underplating of the Hawaiian Swell: evidence from teleseismic receiver functions. *Geophys. J. Int.* 183, 313-329, doi: 10.1111/j.1365-246X.2010.04720.x.

Li, X., R Kind, K Priestley, S Sobolev, F Tilmann. (2000) Mapping the Hawaiian plume conduit with converted seismic waves. *Nature*, 405 (2000), pp. 938–941.

Li, X., R. Kind, X. Yuan, I. Wölbern, W. Hanka (2004) Rejuvenation of the lithosphere by the Hawaiian plume. *Nature*, 427 (2004), pp. 827–829.

Monnereau, M., M. Rabinowicz, and E. Arquis (1993) Mechanical erosion and reheating of the lithosphere: A numerical model for hotspot swells, *J. Geophys. Res.*, 98, 809-823.

Müller, R.D., Sdrolias, M., Gaina, G., and Roest, W.R. (2008) Age, spreading rates, and spreading asymmetry of the world's ocean crust. *Geochem. Geophys. Geosys.* 9,Q04006. doi:10.1029/2007GC001743.

Nishimura, C.E. and Forsyth, D.W. (1989) The anisotropic structure of the upper mantle in the Pacific, *Geophys. J. Int.*, 96, 203–229.

Obrebski, M., R.M. Allen, F. Pollitz, and S.-H. Hung (2011) Lithosphere-asthenosphere interaction beneath the western United States from the joint inversion of body-wave traveltimes and surface-wave phase velocities, *Geophys. J. Int.* 185, 1003-1021, doi:10.1111/j.1365-246X.2011.04990.x.

Paige, C.C. and Saunders, M.A. (1982) LSQR: An algorithm for sparse linear equations and sparse least squares, TOMS, 8, 43–71.

Pietruszka, Aaron J.; Norman, Marc D.; Garcia, Michael O.; Marske, Jared P.;Burns, Da le H. (2013) Chemical heterogeneity in the Hawaiian mantle plume from the alteration and dehydration of recycled oceanic crust. *Earth Planet. Sci. Lett.*, 361, 298–309.

Priestley, K. and Tilmann, F. (1999) Shear-wave structure of the lithosphere above the Hawaiian hot spot from two-station Rayleigh wave phase velocity measurements, *Geophys. Res. Lett.*, 26, 1493–1496.

Richards, M.A. and Griffiths, R.W. (1988) Deflection of plumes by mantle shear flow: experimental results and a simple theory. *Geophys. J. Int*. 94, 367–376.

Rychert, A.C., Laske, G., Harmon, N., Shearer., P. (2013) Seismic imaging of melt in a displaced Hawaiian plume. *Nature Geoscience* 6, 657–660, doi: 10.1038/ngeo1878.

Schilling, J.G. (1991) Fluxes and excess temperatures of mantle plumes inferred from their interaction with migrating midocean ridges, *Nature*, 352, 397-403.

Schimmel, M. and J. Gallart (2007) Frequency-dependent phase coherence for noise suppression in seismic array data, *J. Geophys. Res.*, 112, B04303, doi:10.1029/2006JB004680.

Schimmel, M., Stutzmann, E., Gallart, J. (2011) Using instantaneous phase coherence for signal extraction from ambient noise data at a local to a global scale, *Geophys. J. Int.*, 184, 494-506, doi: 10.1111/j.1365-246X.2010.04861.x.

Schmerr, N., Garnero,E. (2006) Investigation of upper mantle discontinuity structure beneath the central Pacific using SS precursors. *J. Geophys. Res*. 111, http://dx.doi.org/10.1029/2005JB004197.

Schmerr, N., Garnero,E., and McNamara, A. (2010) Deep mantle plumes and convective upwelling beneath the Pacific Ocean. *Earth Planet. Sci. Lett.*, 294,143–151.

Schutt, D.L. and Lesher, C.E. (2006) Effects ofmelt depletion on the density and seismic velocity of garnet and spinel lherzolite, *J. Geophys. Res.*, 111, B05401, doi:10.1029/2003JB002950.

Shen, Y., C. J. Wolfe and S. C. Solomon (2003) Seismic evidence for a mid-mantle discontinuity beneath Hawaii and Iceland, *Earth Planet. Sci. Lett.*, 214, 143-151.

Sobolev, A.V., Hofmann, A.W., Sobolev, S.V. and Nikogosian, I.K. (2005) An olivine-free mantle source for Hawaiian shield basalts, *Nature*, 434, 590–597.

Steinberger, B., O'Connell, R.J. (1998) Advection of plumes in mantle flow: implications on hotspot motion, mantle viscosity and plume distribution. *Geophys. J. Int*. 132, 412–434.

Steinberger, B., Sutherland, R., O'Connell, R.J. (2004) Prediction of Emperor-Hawaii seamount locations from a revised model of plate motion and mantle flow. *Nature* 430, 167–173.

Tilmann, F.J., Benz, H.M., Priestley, K.F. and Okubo, P.G. (2001) P-wave velocity structure of the uppermost mantle beneath Hawaii from traveltime tomography, *Geophys. J. Int.*, 146, 594–606.

VanDecar, J.C. and Crosson, R.S. (1990) Determination of teleseismic rela- tive phase arrival times using multi-channel cross-correlation and least squares, *Bull. seism. Soc. Am.*, 80, 150–169.

Von Herzen, R. P., M. J. Cordery, R. S. Detrick, and C. Fang (1989) Heat flow and the thermal origin of hot spot swells: The Hawaiian Swell revisited, *J. Geophys. Res.*, 94, 13,783-13,799.

Weis, D., Garcia, M.O., Rhodes, J.M., Jellinek, M., Scoates, J.S. (2011) Role of the deep mantle in generating the compositional asymmetry of the Hawaiian mantle plume. *Nature Geosci.* 4, 831-838.

Wölbern, I., Jacob, A., Blake, T., Kind, R., Li, X. (2006) Deep origin of the Hawaiian tilted plume conduit derived from receiver functions. *Geophysical Journal International* 166, 767–781.

Wolfe, C.J., Solomon, S.C., Laske, G., Collins, J.A., Detrick, R.S., Orcutt, J.A., Bercovici, D., and Hauri, E.H. (2009) Mantle shear-wave velocity structure beneath the Hawaiian hot spot, *Science*, 326, 1388–1390, doi:10.1126/science.1180165.

Wolfe, C.J., Solomon, S.C., Laske, G., Collins, J.A., Detrick, R.S., Orcutt, J.A., Bercovici, D., and Hauri, E.H. (2011) Mantle P-wave velocity structure beneath the Hawaiian hot spot, *Earth planet. Sci. Lett.*, 303, 267– 280.

Woods, M.T. & Okal, E.A. (1996) Rayleigh-wave dispersion along the Hawaiian Swell: a test of lithospheric thinning by thermal rejuvenation at a hotspot, *Geophys. J. Int.*, 125, 325–339.

Yang, Y. and Forsyth, D.W. (2006a) Regional tomographic inversion of amplitude and phase of Rayleigh waves with 2-D sensitivity kernels, *Geophys. J. Int.*, 166, 1148- 1160.

Yang, Y. and Forsyth, D.W. (2006b) Rayleigh wave phase velocities, small-scale convection and azimuthal anisotropy beneath southern California, *J. Geophys. Res.*, 111, B07306, doi:10.1029/2005JB004180.

Yang, Y, A. Li, and Ritzwoller, M.H. (2008) Crustal and uppermost mantle structure in southern Africa revealed from ambient noise and teleseismic tomography, *Geophys. J. Int.*174 (1) , 235-248 doi:10.1111/j.1365-246X.2008.03779.x.

Chapter 3

Imaging earth discontinuity: A 3D pre-stack depth Kirchhoff migration method of teleseismic receiver functions

3.1 Abstract

We present a novel 3D pre-stack Kirchhoff depth migration (PKDM) method for teleseismic receiver functions. The proposed algorithm considers the effects of diffraction, scattering, and travel time alteration caused by 3D volumetric heterogeneities. It is therefore particularly useful for imaging complex 3D structures such as dipping discontinuities, which is hard to accomplish with traditional methods. The scheme is based on the acoustic wave migration principle, where at each time step of the receiver function, the energy is migrated back to the ensemble of potential conversion points in the image, given a smooth 3D reference model. Travel times for P and S waves are computed with an efficient Eikonal solver, the Fast Marching Method. We also consider elastic scattering patterns, where the amplitude of converted S waves depends on the angle between the incident P wave, and the scattered S wave. Synthetic experiments demonstrate the validity of the method for a variety of dipping angle discontinuities. Comparison with the widely used Common Conversion Point (CCP) stacking method reveals that our migration shows considerable improvement. For example, the effect of multiple reflections that usually produce apparent discontinuities is avoided. The proposed approach is practical, computationally efficient, and is therefore a potentially powerful alternative to standard CCP methods for imaging large-scale continental structure under dense networks.

3.2 Introduction

Teleseismic receiver functions [e.g. Phinney 1964; Burdick & Langston 1977; Vinnik 1977; Langston 1979] have become a standard method to map seismic discontinuities in the crust and upper mantle beneath a broadband seismometer. The standard process is to deconvolve the vertical component from the radial component in the coda of teleseismic P wave seismograms. This removes source and instrument effects, while

preserving P-to-S converted phases generated at discontinuities beneath the receiver, which contain a significant amount of information on seismic structure.

There are various ways to analyze and interpret receiver functions. For example, one may invert receiver functions for 1D profiles of velocity structure individually [Kind et al. 1995; Sandvol et al. 1998] or jointly with surface wave dispersion data [Julia et al. 2000; Shen et al. 2012; Bodin et al. 2014]. Alternatively, Zhu & Kanamori [2000] and Chevrot & Van der Hilst [2000] introduced a grid search method over Moho depth (H) and Vp/Vs (κ), the so-called H–κ stacking technique, transforming time domain receiver functions into the depth-Vp/Vs domain. This is a widely used method in seismology to estimate crustal properties [e.g. Julià et al. 2003; Lombardi et al. 2008; Spieker et al. 2014, etc ...].

Receiver functions observed at different stations of an array of seismometers may be combined into a 2D or 3D volume and interpreted structurally. This process often utilizes common conversion point (CCP) stacking [Dueker & Sheehan 1997], which stacks the amplitude of receiver functions from several station-event pairs sampling the same sub-volume. Both the signal-to-noise ratio and the spatial resolution can be significantly improved by optimum CCP binning, moveout correction, and subsequent stacking thus providing important constrains on crustal and upper mantle structure. For example, the USArray seismic network has recently facilitated a number of CCP studies under the US continent [Abt et al. 2010; Schmandt et al. 2012; Tauzin et al. 2013; Lekic & Fischer, 2014]. CCP stacking has also been used in other regions where dense seismic networks are available, such as in Tibet, China [Caldwell et al. 2013; Shi et al. 2015]; in the North China Craton [Ai et al. 2007; Zheng et al. 2014; Liu et al. 2015]; and in Europe [Steckler et al. 2008].

However, early CCP stacking relies on the assumption of a 1D Earth where discontinuities are horizontal. Despite the great success of CCP imaging, numerous studies document that complex 3D structures as well as multiple reflections may result in significant artifacts in the final image. Both Abers [1998] and Morozov [2004] demonstrate the coherency and high amplitude of signals generated by dipping, out-of-plane, structures. Later, a technique for correcting for 3D velocity perturbations along the 1D ray path using the linear tomography assumption with the travel time corrections calculated from a hybrid 3D velocity model [Levander & Miller, 2012] is introduced into CCP. But limited research has been done to demonstrate the improvement over the earlier one in the presence of heterogeneity. Also even if the smoothed background 3D velocity perturbation is “corrected”, CCP processing does not restore dipping events or collapse diffractions because of intrinsic limitation of CCP method, such as the horizontal layer assumption of the pre-mapping stack [Rondenay 2009; Levander & Miller, 2012]. Overall, CCP stacking presents three well known issues: 1) it gives poor results in the presence of lateral volumetric velocity variations, 2) it fails at imaging dipping discontinuities, and 3) final images are strongly polluted by the signal of multiply reverberated waves.

Alternatively, more complex migration techniques can be used to image discontinuities [Claerbout, 1985]. Migration schemes are extensively used in exploration geophysics, and are an active field of research with a wide number of algorithms available such as Kirchhoff migration [Schneider, 1977], or wave-equation migration [Biondi & Sava, 1999; Sava & Biondi, 2004a,b]. Compared with CCP, they require more computation and memory as each observed seismic phase is relocated on a large number

of different grid points of the image, representing the location of a potential scatterer. The main advantage of migration techniques over CCP 1-D mapping is that they make fewer assumptions about the geometry of the subsurface structure. Instead of assuming that the Earth is made of planar, horizontal layers, migration algorithms treat scattering from 2-D and 3-D structures.

Pre-stack Kirchhoff migration of seismic records is a well-established technique in industry to image the shallow sedimentary structure [e.g., Schneider, 1977; Wiggins, 1984; Claerbout, 1985]. It was later introduced to seismology for imaging larger scale structures as local networks became dense enough [e.g. Rondenay et al. 2001; Levander et al. 2005). Teleseismic Kirchhoff migration is an imaging scheme applied to the scattered wavefield associated to incident body waves recorded at an array of stations. The data are weighted and stacked along diffraction hyperbolae for every potential scattering point in a regular grid defining the model space. Effectively, one sums over all the available data that have a travel time consistent with a scatterer at the target point. All the teleseismic Kirchhoff migration techniques that have been developed to date consider only first order interactions between the incident wavefield and subsurface perturbations (i.e. they make use of the single scattering, or Born approximation) [Rondenay, 2009]. Depending on how the scattering coefficient is treated, teleseismic migration schemes can be separated into two groups. One group is based on acoustic scattering, it treats the incoming P wave and the scattered S wave both as scalar, and involves stacking of singly scattered wavefields along diffraction hyperbolae to recover relative scattering intensity/potential at individual points through a 2-D or 3-D model space [Revenaugh 1995; Ryberg & Weber 2000; Sheehan et al. 2000; Levander et al. 2005]. Another group of Kirchhoff migration is based on elastic scattering, which treats the incoming P wave as scalar and scattered S wave as a vector and combines stacking with inversion/backprojection operators [Bostock & Rondenay 1999; Bostock et al. 2001; Poppeliers & Pavlis 2003a; Poppeliers & Pavlis 2003b].

Recently, other migration techniques have been borrowed from industry and applied to teleseismic receiver functions, such as one-way wave-equation migration [Chen et al. 2005], which is a 2-D scheme that still relies on 1-D horizontal layer assumption for the move-out correction; teleseismic shot profile migration [Shragge et al. 2006], which is also a 2D wave-field extrapolation scheme. Another example is reverse time migration (RTM) [Shang et al. 2013], which highly depends on computation capability and image scale. These migration methods are based on powerfull numerical solver for the wave-equation, where the full wavefield is accurately modeled, and finite frequency effects are accounted for.

Finally, full 3-D waveform inversion [Frederiksen & Revenaugh 2004] of scattered waves can be used to recover either scattering potential or estimates of localized material property perturbations relative to the background model. Both acoustic and elastic methods can be highly computationally expensive, especially when it comes to 3D wave field extrapolation using finite difference schemes, or when a large amount of receiver functions are incorporated. For a complete review of available methods, we refer the reader to the review papers by Bostock [2007], and Rondenay [2009].

In this work, we present an efficient 3D pre-stack Kirchhoff depth migration method for teleseismic receiver functions. It highly resembles the acoustic wave migration scheme, as it can account for 3D dipping structures and strong volumetric

heterogeneities. However, this migration scheme is easy to implement and as fast and efficient as CCP depth mapping. It leads to an efficient algorithm for performing migration in 3D, which will allow for the possibility of using it for studies where CCP stacking was previously the only plausible approach. In section 2, we describe the theoretical aspects of our method. In section 3, we illustrate its advantages with some synthetic tests and compare it with the traditional CCP method.

3.3 Methodology:

As summarized in Rondenay [2009], the general framework for Kirchhoff teleseismic wave migration would be:

$$f(r) = \sum_{j=1}^{N} \sum_{r_0=1}^{M} \vartheta(r, r_0, p_j^0) \Delta\tilde{u}[r_0, p_j^0, t = T(r, r_0, p_j^0)] \quad (1)$$

where f(r) is the scattering potential at grid point r, and the stack is performed on N incident waves, measured at M stations. $\Delta\tilde{u}$ is the amplitude of the scattered wavefield measured at station r_0 at time $t = T(r, r_0, p_j^0)$ predicted using a smooth model while p_j^0 is the slowness term for the particular teleseismic event. The summation term over r_0 represents a stack over different stations of the weighted scattered wavefield. $\vartheta(r, r_0, p_j^0)$ is a weighting term that accounts for amplitude effects, such as geometrical spreading, i.e. the amplitude of a converted phase observed at the surface decays as the conversion point gets deeper. Fig. 3.1 depicts the principles of Kirchhoff migration for receiver functions. This is a general approach and there are various ways to implement it. Different methods apply different simplifications to the weights or filters.

The main advantage of pre-stack migration techniques over CCP depth mapping is that they make much fewer assumptions about the subsurface structure, and thus consider seismic scattering in more general terms. However, they still rely on a smoothly varying background velocity model, necessary to back-project the scattered wavefield. In practice, we can get this absolute velocity model from either global or regional tomographic images. 3D volumetric large-scale velocity structure is essential for proper image focusing.

3.3.1 Acoustic scattered-wave migration scheme:

Following Levander et al. [2005], we implement an acoustic scattered-wave migration scheme. The receiver function time domain migration equation writes:

$$f(r) = S_{PS}(r) = \sum_{r_0=1}^{N} \sum_{r_e=1}^{M} RF(r_e, r_0, t = (\tau_P + \tau_S - \tau_e)) \frac{A_S(r,r_0)\cos\theta(r_0)}{A_P(r,r_e)\beta(r_0)} \quad (2)$$

In which, r is the imaging grid point; r_e is the source position, and RF is the receiver function data recorded at station r0, which shall be migrated to depth. $A_P(r, r_e)$

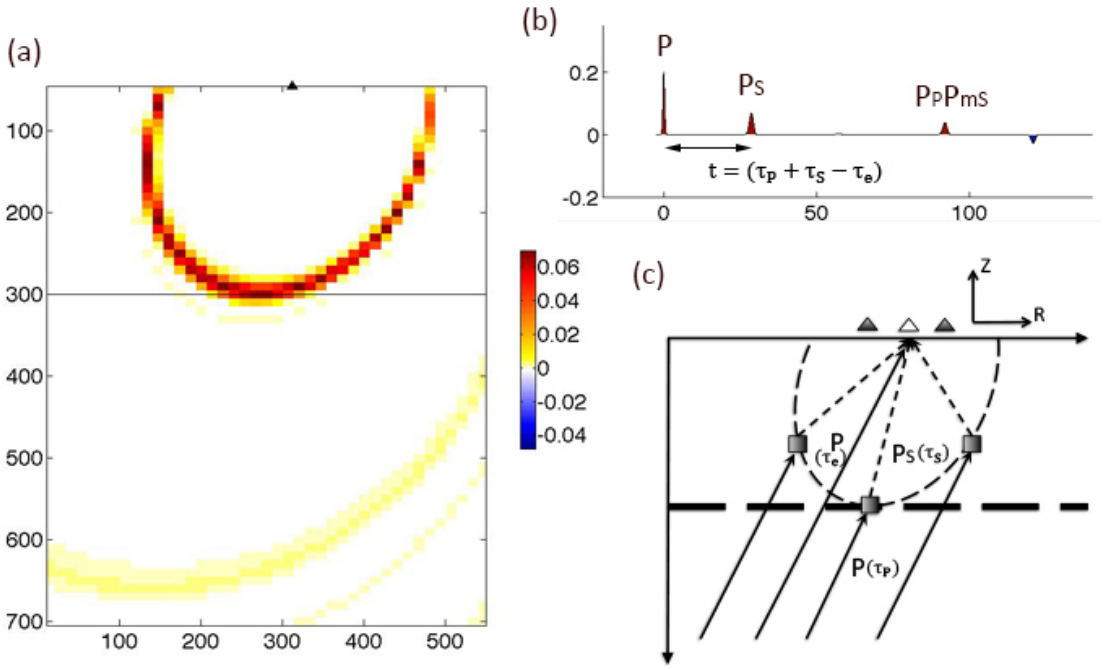

Figure 3.1: Schematic illustrations of how Kirchhoff migration works for a teleseismic receiver function. (a) Migrated parabola of one receiver function, constructed from a simple model made of a horizontal layer over a half space. A vertical slice is shown. (b) Synthetic receiver function used for migration. (c) Ray paths for direct P wave and transmitted S wave in the same vertical plane as (a). The converted Ps phase is migrated to all possible conversion points that predict the observed travel time t.

represents the geometric spreading of the P wave from the source to the imaging grid, and $A_S(r, r_0)$ the geometric spreading of the transmitted S wave from the imaging grid to the station. $\beta(r_0)$ is the surface shear wave velocity and the θ is the incidence angle. The time $(t = (\tau_P + \tau_S - \tau_e))$ is the imaging condition for receiver function Kirchhoff migration, in which τ_P is the P travel time from source to imaging grid, τ_S is the S travel time from imaging grid to receiver and τ_e is the P travel time from source to receivers (see Fig. 3.1).

In Levander et al.'s approach the travel times and amplitude of the P and S wave fields are calculated using an upwind finite-difference solver to account for heterogeneity in the imaging region. Due to heavy computational costs in 3D, the finite-difference scheme used is typically a 2D solver. So the whole formula should be considered as a pseudo-3D equation. For example, in Levander et al. [2005], the correction for out of plane propagation with respect to a reference coordinate, y', using the ray parameter in the coordinate orthogonal to the image, P_y, is included in the phase term (i.e. the time t).

A clear advantage of acoustic scattered-wave migration is the simplicity of the processing and the ability to treat simultaneously a large number of input data to produce images of scattering potential. A limitation of the approach is the lack of formal relationship between the scattering potential and actual material property perturbations in the scattering expressions (except for the P-to-P scattering mode, which is a scalar function of P-wave velocity perturbation) [Bostock et al. 2001; Rondenay 2009]. In particular, this limitation affects images generated by scattering modes involving S-waves (e.g., P-to-S), but can be addressed by solving the problem for elastic waves.

Our method can be viewed as a simplification on Levander et al.'s [2005] acoustic equation in order to consider fully 3D structure, improved by incorporating elastic scattering patterns, which will be discussed in detail in the following sections. Overall, the main advantage of our method is its computational efficiency, which makes feasible applications at continental scales.

Instead of calculating the full wavefield at each grid point by using an expensive 2D finite-difference solver, we make some simplifications on the formula in eq. (2), which allow us to include the full 3D velocity structure. The term $A_P(r, r_e)$ represents the amplitude of the wave propagating from the teleseismic source to the scattering grid point. It has relatively small variations across the model box, and hence can be simplified to a constant across the whole image. Another term $A_S(r, r_0)$ represents the geometrical spreading of the scattered S wave, i.e. the converted S wave traveling from the grid point to the receiver. Instead of calculating it using a finite-difference solver in a heterogeneous model, here we simplify it as a $1/d$ term in a 3D case [Rondenay, 2009], where d is the Euclidian distance between r and r_0. Assuming only geometrical spreading is like assuming a constant velocity model, and ignoring focusing and defocussing effects due to volumetric heterogeneities. This may be adequate with a smoothly varying velocity field. In this way, these simplifications leave us with only the travel time calculation, which we implement with the Fast Marching Method [Rawlinson et al. 2004].

The simplified migration equation takes the form of:

$$f(r) = S_{PS}(r) = \sum_{r_0=1}^{N} \sum_{r_e=1}^{M} RF(r_e, r_0, t = (\tau_P + \tau_S - \tau_e)) \frac{1}{d} \times \mathcal{W} \qquad (3)$$

where $\mathcal{W}$ reprents some weighting coefficient which will be discussed in detail later.

3.3.2 Fast Marching Method:

The Fast Marching Method (FMM) [Sethian 1996; Sethian & Popovici 1999] is a grid based numerical scheme for tracking the evolution of monotonically advancing interfaces via finite difference solution of the Eikonal equation. The Eikonal equation states that the magnitude of the traveltime gradient at any point along a wave front is equal to the inverse of the velocity at that point and is written as $|\nabla T = s(r)|$, where s(r) is the local slowness. To date, FMM has been applied to a wide variety of problems including seismic wave propagation, photolithographic development, geodesics, deposition of sediments, and medical imaging. In this work, we use FMM as a quick and efficient way to estimate travel times between source, receiver, and grid point pairs.

The principal drawbacks of standard ray tracing schemes are related to robustness, speed and ray selection. It can also be a time consuming process, especially if a large number of sources and receivers are involved and the medium is 3-D, as in our migration case. FMM distinguishes itself by combining both unconditional stability and rapid computation, making it a truly practical scheme for velocity media of arbitrary complexity. Some synthetic tests [Rawlinson et al. 2004] have shown that wave fronts can be accurately tracked with minimal computational effort, even in the presence of complex velocity fields and layer boundaries with high curvature. These features of FMM make our migration algorithm computationally effective, as it only requires travel time computations for all source-receiver grid point pairs (see cartoon in Fig. 3.1). For a detailed discussion on FMM, we refer the readers to Rawlinson et al. [2004].

3.3.3 Travel time Matrix, and stacking:

The FMM algorithm also allows us to compute travel times, and store them in a matrix for a later migration process. We compute three different types of travel times: 1) P wave travel times from sources to stations $\tau_e(r_e,r_0)$; 2) P wave travel times from sources to imaging grid points $\tau_P(r_e, r)$; and 3) S wave travel times from imaging grid points to stations $\tau_S(r, r_0)$. The last one is calculated using reciprocity principle, and shooting rays from stations and propagating the wavefront through the 3D volume to be imaged. Three matrices are thus constructed in three steps:

For each event, run FMM to propagate a wavefront starting from a point source and store the travel time between the source and each station $\tau_e(r_e,r_0)$. The wavefront is tracked in a combination of a global model, and local model for the 3D volume to be imaged.

For each event, run FMM to propagate a wavefront starting from a point source, and store the time between the source and each grid point $\tau_P(r_e, r)$.

For each station, run FMM to propagate a wavefront starting from the station and store the time between the station and each grid point $\tau_S(r, r_0)$.

In this way, the FMM scheme needs only be run N*2*M times, where N is the number of stations and M the number of sources. Since each run of FMM is independent, calculation can be easily parallelized (with linear speed-up), thus reducing computational costs. The reason for separating step 1) and step 2) is because keeping the travel time of the whole wave field inside the memory requires significant space and is not stable, while writing them to the hard disk is time consuming, either way is not efficient.

Once travel times are computed and stored, the staking scheme is simple to implement, and only consists of two loops. It can be summarized by the following pseudo-code:

For each grid point r

For each observed receiver function associated with source re and station r0

Stack the amplitude of the receiver function at time $t=\tau_P + \tau_S - \tau_e$

End second loop

End first loop

As shown in eq (3), the stacked amplitudes are weighted with a number of terms that we detail below. Since each step within both loops can be done independently, the stacking procedure can also be conveniently parallelized (also with linear speed-up). For the synthetic example shown below (i.e. for ~650000 grid points, and 27000 receiver functions), the stacking procedure took about 12 CPU hours.

3.3.4 Weighting terms:

In this work, the data that is back propagated and stacked are radial receiver functions, which are constructed by deconvolving the vertical component from the radial one. Scattered shear waves are observed both on vertical and radial components. Depending on their incidence angle, they will contribute more or less to the radial component. A maximum contribution is expected when the converted S wave arrives vertically under the receiver. That is, the amplitude of converted phases observed on the receiver functions depend on the location of the conversion point. We simply correct for this effect by applying two weighting coefficients in eq. (3). Fig. 3.2a shows θ_1, which is the angle between the line connecting the imaging grid point and the station and vertical direction. Fig. 3.2c shows the migrated parabola after applying the $\cos(\theta_1)$ (see eq. 5 below). Compared with the migrated image shown in Fig. 3.1, there is a cosine-distribution to the amplitude along the parabola.

Future work will include rotating each receiver function to a SV/P receiver function. Given the ray parameter of the incoming P wave, the incidence angle of the P wave at the surface can be given from the P velocity at the surface with a free surface transform [Abt et al. 2010; Yu et al.2013].

Another weighting coefficient is applied for the reason that the main energy in the radial component is from the great circle path. The energy back projected at grid points that are not in the great circle plane are therefore down-weighted by a $\cos(\theta_2)$ term (see eq. 5 below), where θ_2 represent the angle between the line connecting imaging grid point to the station and the great circle in the horizontal map view, as indicated in Fig. 3.2b.

3.3.5 Elastic wave migration and Elastic Scattering pattern:

In the acoustic approach presented above, P and S waves are scalar fields, and only phase information (travel time) is extracted from the data. This is because until now the weighting term in eq. (3) only comprises geometrical spreading, phase shifting, and projection into the radial component, without accounting for amplitudes of elastic interactions. In this way, for an incident P wave impinging upon a scatterer, one assumes that all resulting scattered waves radiate energy uniformly in all directions. However, this is not valid for P to S conversions. For example, as illustrated in Fig. 3.4, the polarity of a converted SV wave is reversed when the angle between the incoming P and converted S is greater than 180 deg. For teleseismic events arriving at near vertical incidence, this is likely to occur for strongly dipping discontinuities (greater than ~50deg). In this case, a positive velocity jump will result in a negative phase in the receiver function. If we do not account for elastic interactions (radiation patterns), this negative phase will be miss-interpreted as a negative velocity jump.

It is possible to account for the full elastic effects, by casting the problem in terms of classical linear inverse theory [Bostock & Rondenay 1999; Miller et al 1987; Bostock et al. 2001]. The cost of these fully elastic approaches though, is a substantial increase in requirements in terms of data sampling and computational cost compared to the acoustic case [Poppeliers, 2001; Pavlis, 2011].

In this work, we account for elastic interactions of forward scattered waves (transmissions) by adding a term in the weighting term in eq. (3) in addition to the elements introduced in the acoustic treatment. This factor corrects for the variation in amplitude of the scattered wave as a function of the angle θ between the incident and scattered (transmitted) wave. This factor is given by the radiation pattern described in Rondenay [2009]:

$$\varepsilon^{P\to S}(r,\theta) = \rho\left(\frac{\delta\beta}{\beta}\left(2\frac{\beta}{\alpha}\sin 2\theta\right) + \frac{\delta\rho}{\rho}\left(\sin\theta + \frac{\beta}{\alpha}\sin 2\theta\right)\right) \qquad (4)$$

where $\delta\beta/\beta$ is the shear wave velocity perturbation, $\delta\rho/\rho$ is the density perturbation and θ is the scattering angle (Fig. 3.5), which is calculated by projecting rays on the great circle plane, using the apparent slowness of the incoming P wave ray, and assuming a straight rays between projected grid point and station for the converted S wave. Future work will include accounting for fully 3D elastic patterns [Dahlen et al. 2000]. In elastic scattered wave migration/inversion schemes [Bostock & Rondenay, 1999; Bostock et al. 2001], velocity and density perturbations are unknown parameters to be solved for. In this work, we simply are interested in the angular dependence, and we fix $\delta\beta/\beta$ to a constant value and assume the density perturbation is zero. The factor $\delta\beta/\beta$ we choose as no importance, as it will act as a scaling factor for the final image. This might also be reasonable when a smoothly changing velocity and density field is met across the whole model, which means the perturbation is small and won't change the pattern much across the whole model. The final migration equation writes:

$$f(r) = S_{PS}(r) = \sum_{r_0=1}^{N}\sum_{r_e=1}^{M} RF(r_e, r_0, t = (\tau_P + \tau_S - \tau_e))\frac{1}{d}\cos\theta_1\cos\theta_2\,\varepsilon^{P\to S}(r,\theta) \qquad (5)$$

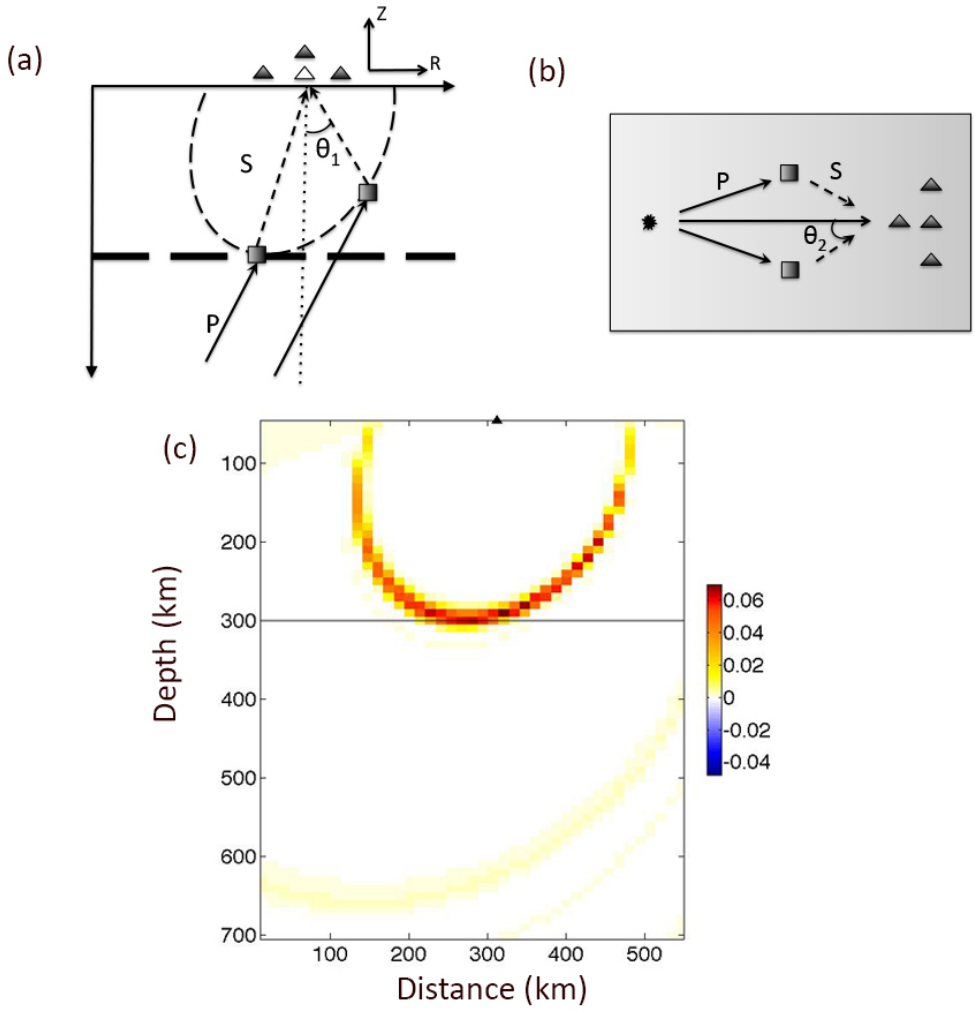

Figure 3.2: Schematic illustration of the two weighting coefficients applied during the 3D Pre-stack Kirchhoff migration process. (a) is a vertical section and shows θ_1, which is the angle between the line connecting the imaging grid point and station in the vertical plane. (b) is map-view and shows θ_2, which is the angle between the line connecting imaging grid-point and station, and the great circle path. (c) is a vertical section through the migrated parabola after applying these two cosine terms.

In the case of a grid point where the incident P and transmitted S are collinear (θ = 180 deg), no energy can be transmitted from the P wave to the S wave, and hence we do not migrate the amplitude of the RF at this grid point (the weigh equals 0). As will be shown in the next section (Fig. 3.6), this scattering pattern significantly improves the image, especially for structures with large dipping angle.

3.4 Synthetic tests

3.4.1 Model geometry and Data:

We compare our method with traditional CCP with synthetic seismograms generated from a known velocity model. The true model is defined as two layers of constant velocity separated by a dipping planar discontinuity (Fig. 3.3), a feature often targeted by RF studies in subduction zones. The top layer has seismic velocities of 3.9 km/s for S waves and 7.2 km/s for P waves. The bottom layer has velocities of 4.5 km/s for S waves and 8.1 km/s for P waves. In the migration process, the reference model used for travel time calculation is a smoothed version of the true model around the discontinuity. We smoothed it over two grid points to mimic tomographic models.

We present results for three cases, with different angles of dip: 0°, 30° and 60°. At the surface, a 30 by 30 square stations array records the teleseismic events, with a station spacing of 30km similarly to some dense networks in western North America (e.g. FACES and MENDOCINO experiments [Eakin et al. 2010]). It can be shown that ideally the station spacing required to avoid spatial aliasing approaches asymptotically $\lambda/2$ [Rondenay et al. 2005] where λ is the wavelength. However this effect tends to diminish with increasing depth and affects the resulting image between the surface and a depth equivalent to approximately twice the station spacing [Rondenay et al. 2005]. In the synthetic tests shown here, the inter-station spacing is 30km and all the discontinuity structures starts deeper than 50km, and hence we only stack receiver functions for grid points deeper than 50km. The teleseismic sources used in this study are regularly distributed on a circle around the network, with an average epicentral distance of 80°, as showed in Fig. 3.3a.

Synthetic waveforms are constructed with the RAYSUM package [Frederiksen & Bostock, 2000], a ray theoretical scheme that allows one to model teleseismic waves in dipping anisotropic structures. Once synthetic seismograms are generated, receiver functions are constructed by deconvolving the vertical component from the radial component with a frequency domain deconvolution method [Ammon, 1991]. A low-pass Gaussian filter (corresponding to a time pulse of almost 4 s) is applied to stabilize the deconvolution, followed by a bandwidth filter (with cut-offs of 1Hz to 0.1Hz). Fig. 3.4 shows the synthetic waveforms for all events at one station, for each of the three velocity models.

The main advantage of the proposed scheme is the ability to efficiently compute travel times in 3D with FMM. However, we acknowledge that here we only test our approach in a 2.5D scenario. This experiment should be seen only as a proof of concept, to demonstrate how our procedure outperforms CCP stacking. To better estimate the

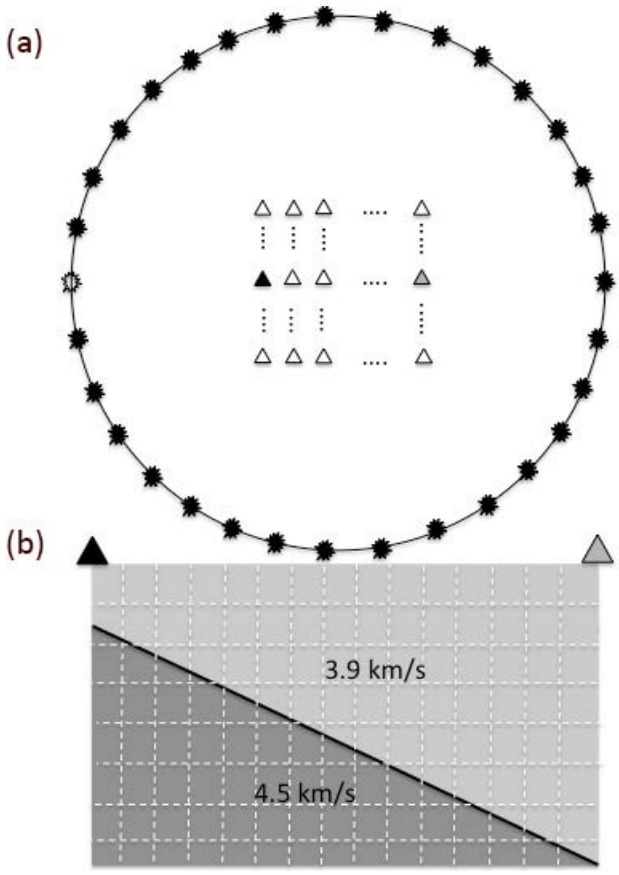

Figure 3.3: (a) Schematic figure (not to scale) showing the earthquake source distribution map used for simulations. A circle of sources surrounds our grid of surface seismic stations (triangles), which is roughly 80° epicentral distance from the sources. A solid triangle corresponds to the seismograms showed in figure 3.4. (b) is a vertical section though our synthetic velocity model. We test three cases with a horizontal or dipping interface. The angels of dip used were 0°, 30°, and 60°.

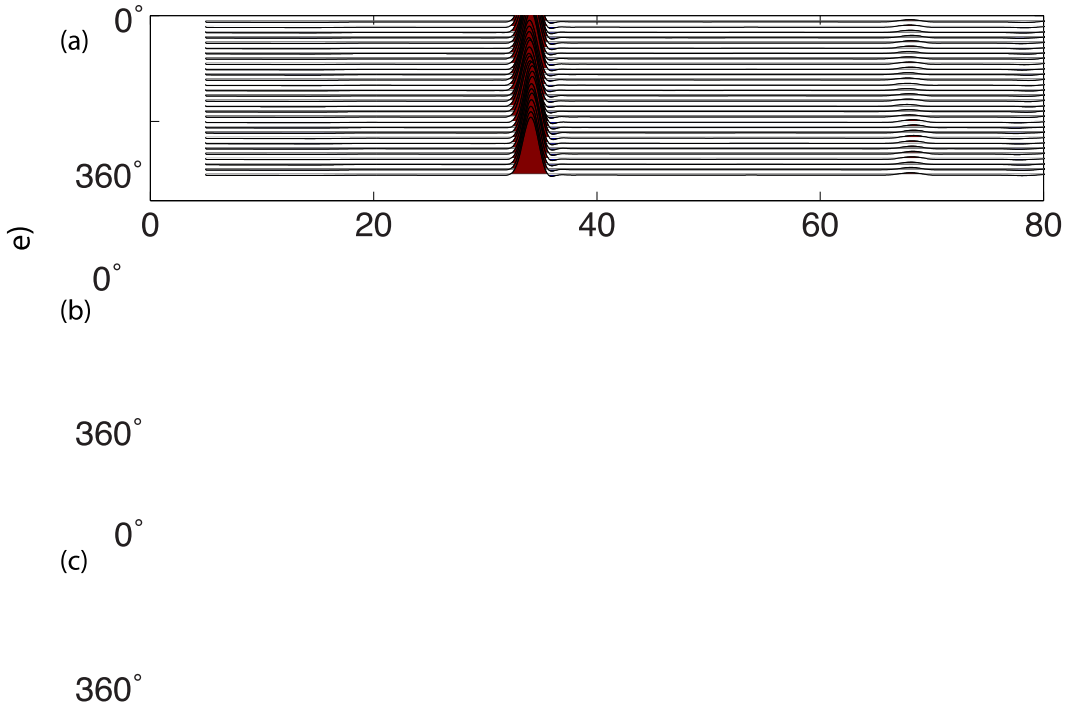

Figure 3.4: Synthetic receiver functions from the station showed with solid triangle in Fig. 3.3(a) for the 3 models studied here: (a) 0° dip, (b) 30° dip, and (c) 60° dip. Receiver functions are shown between 5s and 80s, and hence the first P pulse is not visible here. The effects of the dipping layer are clearly visible including the azimuthal dependence of travel times and polarities.

resolving power and full potential of our method, future work will consist of testing our scheme in a fully 3D experiment (with 3D synthetics computed with a Hybrid waveform modeling code [Monteiller et al. 2013]). In such 3D experiments, we will be able to compare results with other approaches based on a 2D assumptions [e.g. Bostock & Rondenay 1999; Bostock et al. 2001; Levander et al. 2005]. We also plan to assess the resolving power of the method in different situations, e.g. by varying data sampling and data noise.

3.4.2 Results:

In order to illustrate the benefit of using elastic scattering patterns to weigh the amplitude of migrated waveforms at conversion points, we first compare results with and without accounting for scattering patterns, i.e. acoustic versus elastic migration.

The amplitude of a Ps wave converted at a dipping positive discontinuity is reversed for events coming from the down-dip direction (Fig. 3.4c, Fig. 3.5b) [Bianchi et al. 2008]. This produces apparent negative discontinuities in acoustic migration stacks as illustrated in Fig. 3.5c, for the 60° dipping case.

When all backazimuths are migrated together (Fig. 3.6), this negative energy coming from the down-dip direction may interfere destructively with the positive energy coming from other backazimuths, which produces some artifacts in the final image (Fig. 3.6b).

The problem of reversed polarities can be addressed by introducing the factor $\varepsilon^{P\rightarrow S}(r,\theta)$ accounting for elastic scattering patterns. Fig. 3.5d clearly shows that, after this correction, the polarity of the negative phases is flipped, and hence they correctly represent a positive velocity jump in the stacked migrated image.

Another synthetic test is shown in Fig. 3.6, for which we used events at all azimuths (Fig. 3.3a). Fig. 3.6a shows the stacked image using the acoustic migration (no polarity correction) for the 60° dipping case. Fig. 3.6b shows the elastic case with the scattering pattern polarity correction. Without the elastic correction (Fig. 3.6a) there is a negative energy artifact in the upper mantle, above the dipping interface, which disappears when the correction is included (Fig. 3.6b).

We compare the results of CCP depth mapping and final FMM pre-stack migration for different dipping interfaces (Fig. 3.7). Imaging dipping structures is one of the challenges to understand the dynamics of subduction zones [Rondaney, 2009]. During the CCP stacking process for the receiver functions, the stacking bins are designed to be equally spaced but the width of bins is allowed to vary along the stacking profile according to the data coverage. After the CCP stacking, the stacked receiver functions are simply mapped to the depth domain. The CCP depth images have similar appearance as those of the unmigrated time domain CCP receiver functions (not shown here). The images obtained by 3D pre-stack migration are shown along the same profile, which is perpendicular to the strike of the dipping plane. This allows us to directly compare the two approaches and to see their systematic differences.

As shown in Fig. 3.7a and d, both methods recover the discontinuity quite well in the 0° dipping case. However, the prestack Kirchhoff migration doesn't show any artifacts due to multiple reflections, as this energy does not interfere constructively during the

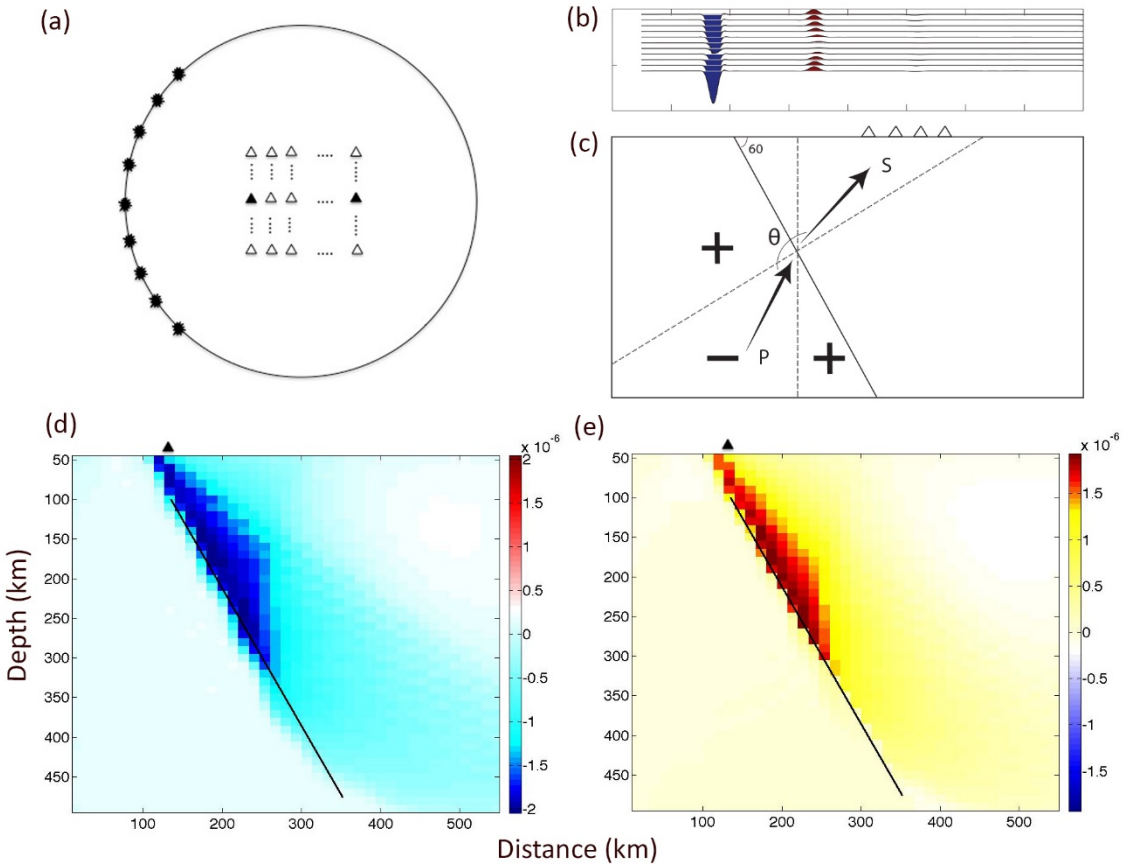

Figure 3.5: Receiver function images with and without application of the scattering coefficient as a weighting term. (a) Schematic figure shows events used in this simulation, for which all the ray path fall in the negative domain in (c). (b) Receiver functions from the same station as in Fig. 3.4, constructed with RAYSUM package for the events showed in (a). (c) Vertical section showing the model used in this synthetic test with a 60 deg dipping layer (dashed line). The positive and negative symbols show the polarity of P to S energy in receiver functions. (d) Migration result without the scattering polarity correction. (e) Migration result after applying the scattering correction. The solid black triangle in (d) and (e) shows where the array starts at the surface. Notice the length of the array is ~900km so the image is a subsection.

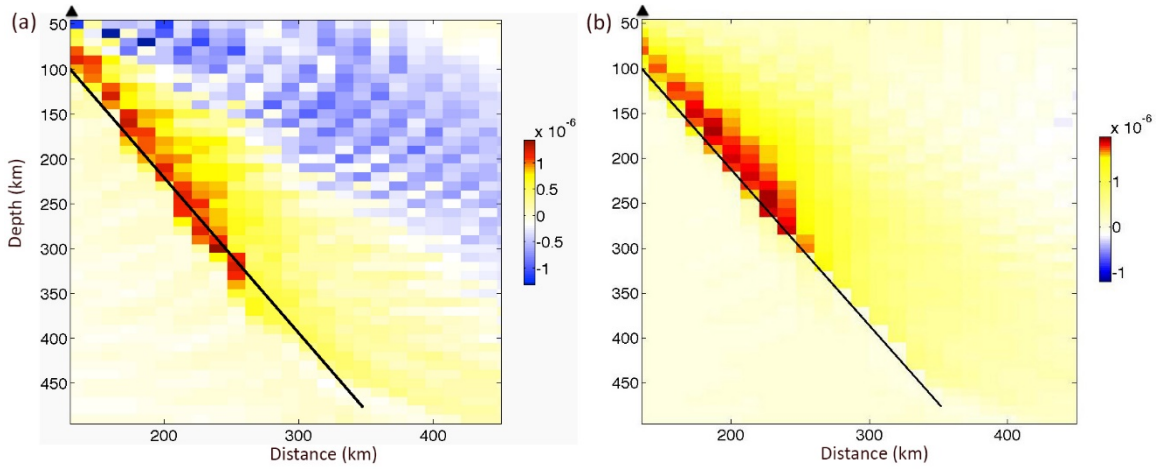

Figure 3.6. 3D Pre-stack Kirchhoff migrated image without (a), and with (b) the elastic scattering pattern polarity correction applied as a weighting coefficient. The 60° dipping interface is indicated by the solid black line. The solid black triangle in (a) and (b) shows where the array starts at the surface. Notice the length of the array is ~900km so the image is a subsection.

stacking process. When interpreting receiver function CCP stacks, it is well known that the image is contaminated by spurious discontinuities due to multiples. Whether and how to interpret the negative energy below the Moho or other positive discontinuities is unclear. The lithospheric signal can be at the same depth as the multiples. Using our pre-stack Kirchhoff migration approach clearly images the discontinuity without the constructive energy from multiples.

In the case of dipping interfaces, the assumption of a horizontal and planar structure adopted in the CCP stacking leads to either wrong information on geometry or distortion of the shape of the discontinuities, such as the shallow dipping structure or defocusing of the diffracted energies (Fig. 3.7b and c). In contrast, the pre-stack migration significantly reduces the unwanted stacking effects and properly accounts for the propagation effects of lateral heterogeneities by making no assumption on the shape of the discontinuities (Fig. 3.7e and f).

In the 30° case, the CCP stacks yield a dip angle smaller than the real model, and a shallower interface, while the pre-stack Kirchhoff migration algorithm is still recovering the interface well. This is because the horizontal layer assumption made in the CCP is not valid, which results in underestimating the dip angle. We also notice the presence of an artificial interface in the CCP image, due to multiple reflections.

In the 60° case, the CCP totally fails at recovering the dip angle and the position of the interface. The energy generated by the interface is highly defocused. In contrast, the pre-stack migration coherently recovers the interface down to ~400km. The maximum depth to which the interface can be imaged is dependent on the array aperture. The signal-to-noise ratio in the resultant image is proportional to the square root of the number of receiver functions used in stacking [Morozov and Dueker, 2003]. For real data with noise, since data is stacked, and that noise is not correlated between the different amplitudes stacked, noise will decrease with stacking, and hence effect of noise is also directly proportional to level of data sampling.

3.5 Summary

We have presented a practical and scalable three-dimensional Kirchhoff pre-stack depth migration scheme for receiver functions analysis of teleseismic arrivals. Receiver functions computed at an array of stations are back propagated to depth through a 3D background model with an Eikonal solver (the fast marching method) that is significantly computationally cheaper than standard finite difference schemes.

Synthetic experiments demonstrate that the proposed method allows us to accurately image 3D complex structures, such as dipping discontinuities. Compared with traditional CCP depth mapping, our migration procedure presents three advantages that significantly improves the quality of the image:

1. By using a 3D background model for migration, we account for 3D volumetric heterogeneities, whereas CCP assume a 1D reference Earth.
2. Dipping discontinuities are accurately mapped.
3. Multiple reflections interfere destructively and do not appear as spurious discontinuities in the final image.

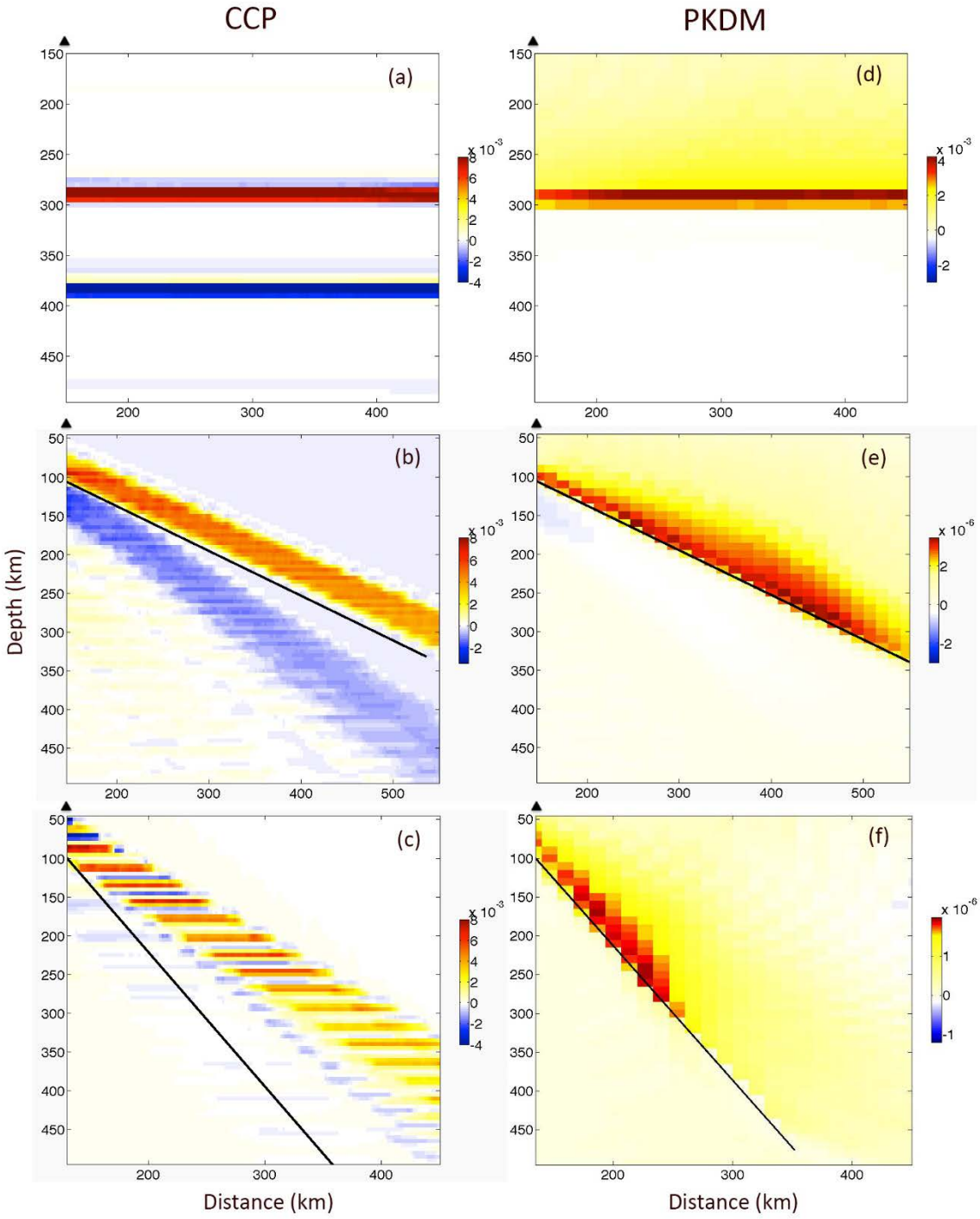

Figure 3.7: Receiver function images using CCP depth migration (a)-(c), and 3D pre-stack Kirchhoff depth migration (d)-(f) for our three synthetic models with dips of 0° (a,d), 30° (b,e), and 60° (c,f). Solid black lines mark the real location of the model discontinuity. The solid black triangle in all the figures shows where the array starts at the surface. Notice the length of the array is ~900km so the image is a subsection.

At the same time, compared with more sophisticated finite difference migration schemes [Bostock et al. 2001; Poppeliers & Pavlis 2003a; Poppeliers & Pavlis 2003b], our method only requires computations of travel times, and hence is conceptually simpler, easier to implement, and computationally cheaper. In this way, it has the potential to be applied to large arrays of stations (e.g. USArray) for seismic imaging at the continental scale.

We also acknowledge that Kirchhoff methods have drawbacks. Identifying appropriate imaging conditions (weighting terms) may be difficult. The effects of noise in the data and inaccurate velocity models (both inaccurate velocities and complexities of the real Earth that are not accounted for in the smooth model), and sparse (low-fold) coverage, lead to poor performance of Kirchhoff methods. A problem here is that most earthquake data is very low-fold, and these issues may be non-negligible for further applications. This first work only presents a proof of concept and future work will include testing our migration approach in fully 3D structures, quantifying resolution, and testing the limits in terms of data coverage, station spacing, data noise, etc.

Also one of the great advantages of Kirchhoff methods for earthquake applications is that the receivers do not need to be evenly spaced. However, large gaps between receivers will produce artifacts or low amplitudes or unrecognizable features in the model. This could possibly be addressed using least-square migration scheme [Nemeth et al. 1999] in the future.

We expect this method to be a powerful tool for imaging subduction zones where the key tectonic structure has a large dip. Accurate imaging will put constraints on the slab location and material pathways into the mantle and also can provide prior information for geodynamic modeling of subducted plate. The method will likely be most helpful in regions with large slab dips such as the Cascadia subduction zone, Japan, Central America and the Aegean.

3.6 Bibliography

Abers, G. (1998) Array measurements of phase used in receiver-functions calculations: importance of scattering. *Bull. Seismol. Soc. Am.*, 88, 313-318.

Abt D., Fischer K.M., French S.W., Ford H.A., Yuan H.Y. and Romanowicz B. (2010) North American lithospheric discontinuity structure imaged by Ps and Sp receiver functions. *J. geophys. Res.*, 115, B09301, doi:10.1029/2009JB006914.

Ai, Y., Chen, Y., Zeng, F., Hong, X. and Ye, W. (2007) The crust and upper mantle structure beneath southeastern China. *Earth Planet. Sci. Lett.*, 260, pp. 549–563

Ammon, C.J. (1991) The isolation of receiver effects from teleseismic P waveforms. *Bull. Seismol. Soc. Am.*, 81, 2504-2510.

Bianchi, I., Agostinetti, N.P., Gori, P.D. and Chiarabba, C. (2008) Deep structure of the Colli Albani volcanic district (central Italy) from receiver functions analysis. *J. Geophys. Res.*, 113, B09313, doi:10.1029/2007JB005548.

Biondi, B. and Sava, P. (1999) Wave-equation migration velocity analysis*: 69th Annual International Meeting, SEG*, Expanded Abstracts, 1723–1726.

Bodin, T., Yuan, H.Y. and Romanowicz, B. (2014) Inversion of receiver functions without deconvolution, *Geophys. J. Int.*, 196 (2), 1025–1033.

Bostock, M.G. and Rondenay, S. (1999) Migration of scattered teleseismic body waves. *Geophys. J. Int.*, 137:732 – 746.

Bostock, M.G., Rondenay, S. and Shragge, J. (2001) Multiparameter two-dimensional inversion of scattered teleseismic body waves, 1, Theory for oblique incidence, *J. Geophys. Res.*, 106:30771 – 30782.

Bostock, M.G. (2007) Teleseismic Body-Wave Scattering and Receiver-Side Structure, *Treatise on Geophysics*, volume 1:219-246.

Burdick, L. and Langston, C. (1977) Modeling crustal structure through the use of converted phases in teleseismic body-wave forms. *Bull. seism. Soc. Am.*, 67(3), 677 – 691.

Caldwell, W. B., Klemperer, S. L., Lawrence, J. F. and Ashish, S. S. R. (2013) Characterizing the Main Himalayan Thrust in the Garhwal Himalaya, India, with receiver function CCP stacking. *Earth Planet. Sci. Lett.*, 367, 15–27.

Chen, L., Wen, L.X. and Zheng, T.Y. (2005) A wave equation migration method for receiver function imaging, (I) Theory. *J. Geophys. Res.*, 110, p. B11309 http://dx.doi.org/10.1029/2005JB003665.

Chevrot, S., and van der Hilst, R. D. (2000) The Poisson ratio of the Australian crust: geological and geophysical implications, *Earth Planet. Sci. Lett.*, 183(1), 121-132.

Claerbout, J.F. (1985) Imaging the Earth's Interior, Blackwell Scientific Publications, Oxford.

Dahlen, F.A., Nolet, G., Hung, S.-H. (2000) Fréchet kernels for finite-frequency traveltime—I. Theory, *Geophys. J. Int.*, 141, 157–174.

Dueker, K. G., and Sheehan, A. F. (1997) Mantle discontinuity structure from midpoint stacks of converted P to S waves across the Yellowstone hotspot track. *J. Geophys. Res.*, 102, 8313 – 8327.

Eakin, C.M., Obrebski, M., Allen, R.M., Boyarko, D.C., Brudzinski, M.R. and Porritt, R. (2010) Seismic anisotropy beneath Cascadia and the Mendocino triple junction: interaction of the subducting slab with mantle flow. *Earth planet. Sci. Lett.* (297, 627–632.

Frederiksen, A.W. and Bostock, M.G. (2000) Modelling teleseismic waves in dipping anisotropic structures. *Geophys. J. Int.*, 141:401 – 412.

Frederiksen, A.W. and Revenaugh, J. (2004) Lithospheric imaging via teleseismic scattering tomography, *Geophys. J. Int.*, 159:978 – 990.

Julia, J., Ammon, C.J., Herrmann, R.B. and Correig, A.M. (2000) Joint inversion of receiver function and surface wave dispersion observations, *Geophys. J. Int.*, 143,1 – 19.

Julià J., Ammon C.J. and Herrmann R.B. (2003) Evaluation of deep sediment velocity structure in the New Madrid Seismic Zone. *Bull. seismol. Soc. Am.*, 94:334-340.

Kind, R., Kosarev, G. and Petersen, N. (1995) Receiver functions at the stations of the German Regional Seismic Network (GRSN), *Geophys. J. Int.*, 121(1), 191 – 202.

Langston C.A. (1979) Structure under Mount Rainier, Washington, inferred from teleseismic body waves, *J. geophys. Res.*, 84, 4749 – 4762.

Lekić, V. and Fischer, K. M. (2014) Contrasting lithospheric signatures across the western United States revealed by Sp receiver functions, *Earth planet. Sci. Lett.*, 402, 90-98.

Levander, A., Niu, F. and Symes, W.W. (2005) Imaging teleseismic P and S scattered waves using the Kirchhoff integral. In: Levander A, Nolet G (eds) Seismic Earth: array analysis of broadband seismograms, No. 157 in AGU Geophysical Monograph. AGU, Washington, DC, pp 149 – 169.

Levander, A., Miller, M. (2012) Evolutionary aspects of lithosphere discontinuity structure in the western U.S., *Geochem. Geophys. Geosyst.*, 13(1):Q0AK07.doi:10.1029/2012GC004056.

Liu, Z., Niu, F., Chen, Y. J., Grand, S., Kawakatsu, H., Ning, J., Tanaka, S., Obayashi, M. and Ni, J. (2015) Receiver function images of the mantle transition zone beneath NE China: New constraints on intraplate volcanism, deep subduction and their potential link, *Earth Planet. Sci. Lett.*, 412, 101-111.

Lombardi, D., Braunmiller, J., Kissling, Giardini, E.,G. (2008) Moho depth and Poisson's ratio in the Western – Central Alps from receiver functions, *Geophys. J. Int.*, 173, 249 – 264 http://dx.doi.org/10.1111/j.1365-246X.2007.03706.x

Monteiller, V., Chevrot, S., Komatitsch, D. and Fuji, N. (2013) A hybrid method to compute short period synthetic seismograms of teleseismic body waves in a 3-D regional model, *Geophys. J. Int.*, 192, 230–247.

Morozov, I. B., and Dueker, K. G. (2003) Signal-to-noise ratios of teleseismic receiver functions and effectiveness of stacking for their enhancement, *J. Geophys. Res.*, *108*(B2), 2106, doi:10.1029/2001JB001692.

Morozov, I. B. (2004) Crustal scattering and some artefacts in receiver function images, *Bull. Seismol. Soc. Am.*, 94 (4), 1492-1499.

Nemeth, T., Wu, C., Schuster, G.T. (1999) Least-squares migration of incomplete reflection data, *Geophysics*, 64, 208–221.

Pavlis, G.L. (2011b) Three-dimensional, wavefield imaging of broadband seismic array data. *Comput. Geosci.*, 37(8): 1054-1066.

Phinney, R. (1964) Structure of the Earth’s crust from spectral behavior of long-period body waves, *J. Geophys. Res.*, 69, 2997 – 3017.

Poppeliers, C. (2001) Prestack planewave migration of teleseismic P-to-S converted phases. *Ph.D. Dissertation*, Indiana University, Bloomington.

Poppeliers, C. and Pavlis, G.L. (2003a) Three-dimensional, prestack, plane wave migration of teleseismic P-to-S converted phases: 1. Theory, *J. Geophys. Res.*, 108:2112. doi:10.1029/2001JB000216.

Poppeliers, C. and Pavlis, G.L. (2003b) Three-dimensional, prestack, plane wave migration of teleseismic P-to-S converted phases: 2. Stacking multiple events, *J. Geophys. Res.*, 108:2267. doi:10.1029/2001JB001583.

Rawlinson, N., Sambridge, M. (2004) Wave front evolution in strongly heterogeneous layered media using the fast marching method, *Geophys. J. Int.*,156(3), 631 – 647.

Revenaugh, J. (1995) A scattered-wave image of subduction beneath the transverse ranges, *Science*, 268: 1888 – 1892.

Rondenay, S., Bostock, M.G. and Shragge, J. (2001) Multiparameter two-dimensional inversion of scattered teleseismic body waves, 3, Application to the Cascadia 1993 data set, *J. Geophys. Res.*, 106:30795 – 30808.

Rondenay, S., Bostock, M. and Fischer, K. (2005) Multichannel inversion of scattered tele-seismic body waves: Practical considerations and applicability, in LevanderA., Nolet G. eds., Seismic Earth: Array analysis of broadband seismograms: American Geophysical Union Geophysical Monograph 157, p. 187 – 204.

Rondenay, S. (2009) Upper mantle imaging with array recordings of converted and scattered teleseismic waves, *Surv. Geophys.*, 30,377 – 405, doi:10.1007/s10712-009-9071-5.

Ryberg, T. and Weber, M. (2000) Receiver function arrays: a reflection seismic approach, *Geophys. J. Int.*, 141:1 – 11.

Sandvol, E., Seber, D., Calvert, A. and Barazangi, M. (1998) Grid search modeling of receiver functions: implications for crustal structure in the Middle East and North Africa, *J. geophys. Res.*, 103(B11), 26899 – 26917.

Sava, P. and Biondi, B. (2004a) Wave-equation migration velocity analysis - I: Theory: *Geophysical Prospecting*, 52, 593–606.

Sava, P. and Biondi, B. (2004b) Wave-equation migration velocity analysis - II: Subsalt imaging examples: *Geophysical Prospecting*, 52, 607–623.

Schmandt, B., Dueker, K., Humphreys, E. and Hansen, S. (2012) Hot mantle upwelling across the 660 beneath Yellowstone, *Earth planet. Sci. Lett.*, 331, 224-236.

Schneider, W.A. (1977) Integral formulation for migration in two and three dimensions, *Geophysics*, 43, 49-76.

Sethian, J.A. (1996) A fast marching level set method for monotonically advancing fronts, *Proc. Nat. Acad. Sci.*, 93, 1591-1595.

Sethian, J.A. and Popovici, A.M. (1999) 3-D traveltime computation using the fast marching method, *Geophysics*, 64, 516-523.

Shang, X., de Hoop, M. and van der Hilst, R. (2012) Beyond receiver functions: Passive source reverse time migration and inverse scattering of converted waves, *Geophys. Res. Lett.*, 39, 1 – 7.

Sheehan, A.F., Shearer, P.M., Gilbert, H.J. and Dueker, K.G. (2000) Seismic migration processing of P – SV converted phases for mantle discontinuity structure beneath the Snake River Plain, western United States, *J. Geophys. Res.*, 105:19055 – 19065.

Shen, W., Ritzwoller, M.H., Schulte-Pelkum, V. and Lin, F.-C. (2013) Joint inversion of surface wave dispersion and receiver functions: a Bayesian Monte-Carlo approach, *Geophys. J. Int.*, 192(2):807-836.

Shi, D., Wu, Z., Klemperer, S. L., Zhao, W., Xue, G., and Su, H. (2015) Receiver function imaging of crustal suture, steep subduction, and mantle wedge in the eastern India–Tibet continental collision zone, *Earth planet. Sci. Lett.*, 414, 6-15.

Shragge, J., Artman, B. and Wilson, C. (2006) Teleseismic shot-profile migration, *Geophysics*, 71(4), SI221–SI229.

Spieker, K., Wölbern, I., Thomas, C., Harnafi, M. and Moudnib, L.E. (2014) Crustal and upper-mantle structure beneath the western Atlas Mountains in SW Morocco derived from receiver functions, *Geophys. J. Int.*, 198(3): 1474-1485.

Steckler, M. S., Agostinetti, N. P., Wilson, C. K., Roselli, P., Seeber, L., Amato, A. and Lerner-Lam, A. (2008) Crustal structure in the southern Apennines from teleseismic receiver functions, *Geology*, 36(2), 155-158.

Tauzin, B., van der Hilst, R. D., Wittlinger, G. and Ricard, Y. (2013) Multiple transition zone seismic discontinuities and low velocity layers below western United States. *J. Geophys. Res.*, 118, doi:10.1002/jgrb.50182.

Vinnik, L. (1977) Detection of waves converted from P to SV in the mantle. *Phys. Earth planet. Inter.*, 15(1), 39 – 45.

Wiggins, J.W. (1984) Kirchhoff integral extrapolation and migration of nonplanar data. *Geophysics*, 49, 1239-1248.

Xue, M. and Allen, R.M. (2007) The fate of the Juan de Fuca plate: Implications for a Yellowstone plume head. *Earth Planet. Sc. Lett.*, 264, 266-276.

Yu, C.Q., Chen, W.P. and van der Hilst, R.D. (2013) Removing source-side scattering for virtual deep seismic sounding (VDSS). *Geophys. J. Int.*, 195 (2013), pp. 1932–1941.

Zheng, T. Y., Zhao, L., He, Y. M. and Zhu, R. X. (2014) Seismic imaging of crustal reworking and lithospheric modification in eastern China. *Geophys. J. Int.*, 196(2), 656-670.

Zhu, L.P. and Kanamori, H. (2000) Moho depth variation in southern California from teleseismic receiver functions. *J. Geophys. Res.-Solid Earth*, 105, 2969 – 2980.

Chapter 4

Cascadia subduction slab heterogeneity revealed by three-dimensional receiver function Kirchhoff migration

4.1 Abstract

We present a 3D model of upper mantle seismic discontinuity structure below Cascadia using a receiver function Kirchhoff migration method. A careful analysis of the primary and multiple reverberated phases allows imaging of the Juan de Fuca plate dipping below the North American continent. The subducting slab is observed as an eastward dipping signal at all latitudes. We associate this signal with a thermal gradient between the slab and surrounding mantle, rather than a sharp chemical discontinuity. Our model also shows along-strike variations in the dipping angle and strength of this signal. To the southern and northern ends of the subduction system, the signal is clearly observed down to ~300 km. However, beneath central Oregon, this structure is missing below ~150km depth. We propose this gap is due to weakening of the slab beneath central Oregon possibly caused by deformation and hydration combined with plume-slab interaction processes after subduction. continental structure under dense networks.

4.2 Introduction

The Cascadia subduction zone is a young lithosphere end-member of the global subduction system [Hacker, 2003]. The Juan de Fuca plate that subducts beneath Cascadia is divided into two sub-plates: the Gorda section subducting under Northern California and the rest of the Juan de Fuca plate (JdF) subducting under Oregon and Washington. Contrary to older and colder subduction zones such as the western Pacific margins, the absence of a well-developed Wadati–Benioff zone in Cascadia limits direct observation of the top of this subducting slab [McCrory et al., 2012].

As one of the most well-observed subduction zones in the world, extensive seismic studies have been done in Cascadia. These include teleseismic tomography [e.g *Obrebski et al.*, 2011; *Hawley et al.*, 2016], regional tomography [e.g. *Gao*, 2016; *Bell et al.*, 2016], receiver function imaging [*Audet et al.*, 2009; 2010], observations of seismic anisotropy [*Martin-Short et al.*, 2015], reflection imaging offshore [*Han at al.*, 2016], and seismicity

studies [*McCrory et al.*, 2012]. All these studies provide imperfect constraints on the geometry and physical properties of the subduction slab and surrounding mantle.

From teleseismic transmitted waves, *Bostock et al.* [2002] *and Bostock* [2013] showed that the dipping angle of the slab is around 30° in the uppermost 100 km of the mantle. Teleseismic tomography models [*Burdick et al.*, 2008; *Obrebski et al.*, 2010; 2011] showed that the dipping angle of the slab between 200 km and 600 km depth varies along-strike with steeper angle to the south. In central Oregon, these models also showed the segmentation of the slab, interpreted as the interaction between the subducted plate and the Yellowstone mantle plume. At shallow depth, a recent study by *Han et al.* [2016] suggests variation of the hydration of oceanic crust/mantle along the strike of the subduction zone, based on the regional differences in the extent of crustal/mantle bend-faulting near the deformation front. They inferred that the oceanic plate offshore Oregon has a higher potential for crustal hydration and mantle serpentinization than offshore Washington.

Receiver function analysis resolves sharp velocity contrasts that produce conversions from P to S waves, which in return can provide information on the chemical and thermal properties of the upper-mantle. Previous RF studies of the North American continent [e.g., *Sheehan et al.*, 2000; *Levander and Miller*, 2012; *Tauzin et al.*, 2013; *Hansen et al.*, 2015; *Hopper et al.*, 2015; *Ford et al.*, 2016] commonly utilize the Common Conversion Point (CCP) stacking method. However, this method assumes horizontal discontinuities, and is known to give poor results in the case of dipping interfaces, such as in the Cascadia subduction zone [*Rondenay*, 2009; *Cheng et al.*, 2016]. *Bostock et al.* [2002] imaged the velocity structure of the subducting plate using a more sophisticated migration/inversion scheme (the 2D Generalized Transform Migration), but this method has been limited to 2D slices because it requires dense arrays of instruments and intense computation. The position of the slab interface at depth, its seismic structure and its lateral variations therefore remains controversial and seismologists keep on applying advanced imaging methods to reveal it [e.g. *Tauzin et al.*, 2016].

In this study, we present an image of the Cascadia subduction zone extending from 10 km down to 450 km depth, based on a 3D pre-stack Kirchhoff depth migration (PKDM) method for teleseismic receiver functions [*Cheng et al.*, 2016]. We account for 3D velocity variations to provide a more accurate and complete 3D discontinuity model for the subducting slab than previous studies [*Levander and Miller*, 2012; *Tauzin et al.*, 2013]. We use a synthetic test to distinguish primary phases from multiply reflected phases that generate spurious artificial interfaces. We find that the dominant seismic discontinuity in the subducting plate, a dipping positive interface marking a shear-wave velocity increase with depth, varies anomalously from the Gorda to the rest of the Juan de Fuca portions of the plate. This heterogeneous pattern of seismic discontinuity structure inside the oceanic slab coincides potentially with slab-plume interaction inferred at similar depth [*Obrebski et al.*, 2010], and may also be related with the fluid distribution in the subducting plate, as reported by *Han et al.* [2016].

4.3 Data and Method

We use a receiver function (RF) database created using three-component broadband

records of passive seismicity at stations deployed during the U.S. Transportable Array experiment between January 2004 and November 2009 [*Tauzin et al.*, 2013]. Waveforms were obtained from the IRIS Data Management Center for 932 teleseismic earthquakes, which resulted in 64,578 receiver functions. The RFs were obtained by deconvolving the vertical component of seismic records from their radial component, and using an iterative time domain deconvolution [*Ligorrìa and Ammon*, 1999].

Two denser arrays of stations were added [*Tauzin et al.*, 2016]: the Cascadia 93 and Mendocino experiments located in central Oregon and northern California respectively (Figure 4.1a). The wide aperture Transportable Array allows us to image the western US structure down to the transition zone (TZ) across the continent. Two RF data-sets were obtained from waveforms low-pass filtered at 0.1 and 0.2 Hz. In this work, we present a migrated model obtained at 0.2 Hz but the same processing has been done from the 0.1 Hz data-set (see Figure 4.5). A seismic section derived by stacking all the RFs at 0.2 Hz is shown in Figure 4.1b. The data are aligned on the P arrival and stacked within 0.25° epicentral distance intervals. After the direct P arrival at 0 s, clear arrivals with similar moveout (travel time decreasing with epicentral distance) are observed around 5 sec and 50 sec. These are, respectively, the direct P-to-S conversions at the continental Moho (Pms), and the 410 km discontinuity (P410s) under the array. Figure 4.1b shows that the signal after the Pms is dominated by free surface reflected multiples (travel time increasing with epicentral distance) in the crust, the PPms (positive) and PSms (negative) phases. Here “m” indicates waves are transmitted or reflected from the continental Moho.

We use a 3D pre-stack Kirchhoff depth migration (PKDM) method for the migration [*Cheng et al.*, 2016]. This algorithm considers the effects of diffraction, scattering and traveltime alteration caused by 3D volumetric heterogeneities. It is therefore particularly useful for imaging complex 3D structures such as dipping discontinuities, which is hard to accomplish with traditional methods. Given a smooth 3-D reference model, traveltimes for P and S waves are computed with an efficient eikonal solver, the fast marching method [*Rawlinson and Sambridge*, 2004]. We also account for the elastic scattering patterns, where the amplitude of converted *S* waves depends on the angle between the incident P wave and the scattered S wave [*Dahlen et al.*, 2000]. The reference P model in the mantle comes from *Burdick et al.* [2010] and the S model in the mantle comes from *Yuan and Romanowicz* [2010]. Seismic velocity and Moho topography of Crust 2.0 model [*Bassin et al.*, 2000] is used in the crust. For a detailed description of the algorithm, we refer the reader to *Cheng et al.* [2016].

Images obtained from classical P-to-S receiver function imaging in a subduction context are usually contaminated by multiple phases reverberating between the surface and the top of the subducted plate [*Tauzin et al.*, 2016], such as PPs and PSs. These free-surface multiples can sometimes generate strong signals, which are mixed together with primary Ps in the migration process. In order to distinguish multiples from primary phases, we first migrate a synthetic dataset using a known velocity model and compare the migrated result to the observed model. The synthetic model is intended to represent a subduction zone: it is defined as three volumes of constant velocity (shown in Figure 4.2b) separated by a Moho at 25 km and a 30-degree dipping planar interface at greater depth (the slab) as shown in Figure 4.2b. The interstation spacing is 30 km and the teleseismic sources used in this study are regularly distributed on a circle around the network, with an average epicentral distance of 80° (Figure 4.2a). The generation of

synthetic waveforms and the process of migration is the same as in *Cheng et al.*, [2016]. As shown in the final migrated image (Figure 4.2c), the dipping interface is recovered quite well by the migrated primary Ps wave. However, multiple reflected phases are also visible in the deeper part of the model. We identify these multiple signals as PPs and PSs for the dipping structure. The horizontal continental Moho also suffers from spatial aliasing making it difficult to identify, as previously discussed by *Cheng et al.*, [2016]. At the same time, a negative PSms reverberation from the continental Moho is clearly imaged around ~100 km depth. Based on this observation, the faint positive signal above the PSms phase may therefore represent the PPms phase from the continental Moho.

4.4 Image result

In contrast to the previous CCP model of *Tauzin et al.* [2013], where a 3-D image is obtained by interpolating a set of parallel 2-D sections, here we directly present a fully 3D migrated image of the Cascadia subduction zone. In Figure 4.3 we show seismic cross-sections along three profiles at constant latitude: A_1-A_2 below Northern California, B_1-B_2 below Central Oregon, and C_1-C_2 below Washington. The image is obtained from the 0.2 Hz dataset. The same images are shown for 0.1 Hz data in Figure 4.5. The position of the profiles in the map view is showed in the Figure 4.1a. Because of the limited frequency content of the observed seismic wavefield, our model only depicts a bandpass-filtered approximation of the true reflectivity structure.

We highlight two features in this reflectivity model. First, the migration algorithm recovers the 410 km discontinuity approximately as a flat interface near 410 km depth. Second, east of 121°W longitude, a strong negative (blue) signal appears between 150 and 200 km depth. We identify this signal as the PSms multiple from the continental Moho that overwhelms the signal associated with the true structure. We interpret this negative signal as a multiple (rather than the base of the lithosphere) for two reasons: first, from the synthetic test in Figure 4.2, we can see that the PSms multiple from a Moho at 25 km is mapped at ~100 km depth; second, the Lithosphere-Asthenosphere boundary in western North America is expected at around ~80 km depth [e.g. *Levander and Miller*, 2012; *Yuan and Romanowicz,* 2010]. Furthermore, we point to the presence of a weak and discontinuous signal at approximately ~80 km on all the profiles (marked by black arrows in Figure 4.3 and 4.5), which represents the actual bottom of the lithosphere. The LAB signal is small and discontinuous at this depth because it suffers from aliasing and the LAB is a relatively weak discontinuity compared to the Moho. Given the station spacing of the US Transportable Array, the same spatial aliasing problem will happen to all structures (Moho, LAB) shallower than ~100 km. Although the negative signal at ~150 km is a multiple from the Moho and should not be interpreted as a discontinuity, it still provides information about shallow structure. For example, in Figure 4.3 and 4.5, the apparent depth of the multiple appears to increase east of 112°W, suggesting an increase of thickness of the crust, in agreement with *Levander and Miller*, [2012]. Quantitative interpretation of surface multiples is beyond the scope of this paper and will be subject of future work.

In this study, we focus our attention on one of the major imaged feature: namely the structure dipping eastward in the upper mantle below the Cascadia volcanic arc, which

we relate to the subduction of the Gorda and Juan de Fuca plate. Since the migration suffers from strong multiple signals that generate spurious interfaces in the final image (Figure 4.2), we first need to separate them from primary phases.

We identify the primary signal Ps from multiples in the following way. First, at depths shallower than 100 km, the synthetics (Figure 4.2) show that dipping interfaces are poorly recovered by primary Ps arrival, and the multiples accompany the main arrival on the left. Our synthetic example also shows that the red-over-blue signal, which is very strong on the left edge of Figure 4.3b-c, is certainly a multiple. Multiples are identified as PPs (red) and PSs (blue) after the primary Ps (red, highlighted with a black dotted line in Figure 4.3 and 4.5). Here we use Ps to indicate the first dominant signal transmitted from the dipping slab. In the discussion section, we propose that this signal is the P-to-S transmitted wave at a discontinuity related to the subducted slab.

Second, this conclusion is further confirmed by comparing our migrated model with the images obtained from a teleseismic P-wave finite-frequency tomography model [*Hawley et al.*, 2016] (Figure 4.4, 4.6). The Ps signals marked by the black dotted lines in Figures 4.3, 4.4, 4.5 and 4.6 coincide with the upper surface of the tomographic fast velocity anomaly. Furthermore, the green dotted lines in Figures 4.4 and 4.6 that we will interpret as the oceanic LAB coincide with the bottom of the tomographic fast velocity anomaly. Note also that the dipping angle of the slab in the two models coincides with each other. Also note that the position of the inferred multiples is not spatially coincident with the fast velocity anomaly of the subducted slab in this tomographic model supporting our interpretation that they are multiples.

In the following sections, we focus our discussion on the 150 km to 410 km depth window, as this portion of the model does not suffer from aliasing problems. In this depth range, the red positive dipping Ps signal marked with a black dotted line in Figure 4.3 and S1 is a Ps transmitted wave and represents the dominant seismic discontinuity of the subducted oceanic plate.

The model (Figure 4.3) shows that the morphology of the Cascadia subduction system varies as a function of the latitude in the upper mantle. A steep subducting slab (~50°) down to at least 300 km is observed for the Gorda plate under Northern California (Figure 4.3c, 4.1c), whereas the profile to the north under Washington (Figure 4.3a, 4.5a) shows the Juan de Fuca plate gently dipping (~30°) at upper mantle depth. More notable is the absence of Pms signal at depths between 150 km and 300 km under Central Oregon (Figure 4.3b, 4.5b), which leaves a gap in the seismic signature of the subducting plate in this region. Figures 4.3d and 4.5d show seismic cross-sections along a profile in the longitude direction D_1-D_2, at -121°. In this view, the Gorda plate appears more steeply dipping than the JdF plate to the north with a clear gap in-between, from 43°N to 46°N near ~250 km depth (Figure 4.3d, 4.5d).

4.5 Discussion

A variety of processes can perturb the structure of the subducted oceanic plate and modify its seismic expression. Early receiver function studies showed that beneath forearc

longitudes the structure of the JdF subducted plate is dominated by the presence of an east-dipping, low-velocity zone (LVZ), which was first interpreted as the oceanic crust [*Langston*, 1981]. Some recent models interpret this LVZ as the uppermost layer of the oceanic crust, which has been extensively hydrated before subduction [*Bostock* 2013]. Hydration and possibly overpressure [*Audet et al.*, 2009] would result in a strong seismic velocity contrast at the base of the LVZ. Therefore, one possible explanation of our observation of a dipping positive (red) Ps signal in the mid-upper mantle is the expression of a velocity contrast between the LVZ and underlying higher-velocity material in the subducting slab.

However, as a young lithosphere end-member of the global subduction system (6 – 10 Ma at trench), the oceanic crust is expected to reach the dehydration solidus, i.e. eclogitization, at depth shallower than 100km [*Hacker et al.*, 2003]. The oceanic crust undergoes eclogitization in a top-down sense leading to gradual disappearance of the LVZ with depth in the subduction zone. *Bostock* [2013] argues that eclogitization reduces the seismic velocity contrast within the LVZ in two ways. First, the mineralogy changes as lower-velocity minerals are replaced by higher-velocity minerals. Second, eclogitization produces a ~10% volume reduction in the solid phase thereby reducing pore pressures. The LVZ under Washington can be traced down to ~100 km; under central Oregon, it disappears at a very shallow depth (~40 km) due to dehydration [*Bostock*, 2013]. In conclusion, this process occurs before the slab reaches 100 km depth. An observation of the oceanic slab Moho (or base of the LVZ) as deep as ~300 km is therefore quite rare, and the eclogitization process is unlikely to explain our dipping Ps signal in the mid-upper mantle.

Alternatively, another explanation for this signal is that it represents the thermal velocity gradient or boundary layer between the cold subducting slab and the surrounding continental mantle. A similar observation has been made in Southern Central America Cocos plate by *MacKenzie et al.* [2010], where they find a steeply dipping subducting slab down to 200 km under Nicaragua. At 200 km, steady state thermal models [*Peacock et al.*, 2002] predict a lateral temperature change of around 50°C over a 15 – 25 km distance. The method of *Hacker and Abers* [2004] predicts a 6 – 9% velocity increase from this temperature change in peridotites. Such a broad velocity gradient would be seen as a discontinuity at long wavelengths. Given the resolution of our receiver function data (the 5 sec RF data allows a vertical resolution of ~10 km and the 10 sec RF data allows a vertical resolution of ~25 km; [*Bostock*, 1999]), it is hard to distinguish between a thermal gradient layer on this scale and a sharp chemical discontinuity. Given this interpretation, we would also expect to see consistency between our migration model and the longer-wavelength temperature-driven tomographic anomalies observed by *Hawley et al.*, [2016].

The heterogeneity of the Ps interface along the strike is also striking. In our model, the positive (red) dipping Ps signal in Figure 4.3b and 4.5b under Central Oregon dissapears by ~150 km depth. However, under Washington and Northern California, this signal persists to the approximate depth of 300 km in the upper mantle. This observation of a gap between 43°N and 46°N is also consistent with the results of tomographic studies [*Hawley et al.*, 2016; *Obrebski et al.*, 2010], showing a much weaker high velocity anomaly representing the oceanic slab under Central Oregon than below Washington or North California (e.g. Figure 4.4b).

It is not clear why the slab signal in both models is not seen past ~150 km depth under Central Oregon. *Obrebski et al.* [2010] speculated that the interaction of the Yellowstone plume with the slab, starting from 17-19 Ma, caused the break-up of the Cascadia subducting slab and had a longer-lasting effect at the point of origin beneath Oregon. While the arrival of the buoyant plume likely precipitated break-up of the slab, pre-existing weaknesses may also have facilitated this break-up. In our model, the dipping angle varies along strike, and is larger under Northern California than under Washington. This change of slab curvature along the trench of the subduction zone could originate from localized deformation due to slab weakening under central Oregon. *Bercovici et al.* [2015] proposed a weakening mechanism for necking and rapid slab detachment, based on grain reduction and damage in polycrystalline rocks due to entrainment of thick buoyant crust such as oceanic plateaux, mid-oceanic ridges, or continental material in the subduction zone. Rheology is also known to play a role in strain localization. We speculate that an alternative mechanism for strain localization and slab-detachment is extensive hydration of the oceanic plate offshore of Oregon due to the presence of faulting through the entire oceanic crust. Such faulting has been proposed based on lithospheric imaging using seismic reflection profiling offshore of Oregon and Washington [*Han et al.,* 2016]. This could lead to the formation of a thick and weak layer of serpentinite in the oceanic mantle.

4.6 Conclusion

As a conclusion, whatever the causal mechanism is, our migration approach clearly shows a variation in the dip and depth extend of the Ps refraction. The observed variation is consistent with that previously imaged using tomographic techniques and is likely caused by a steep thermal gradient between the slab and surrounding mantle rather than a chemical discontinuity. This variability may be related to localized deformation and variations in the hydration of the incoming oceanic lithosphere due to crust-cutting faults observed offshore of Oregon, and may also be related to plume processes as previously proposed.

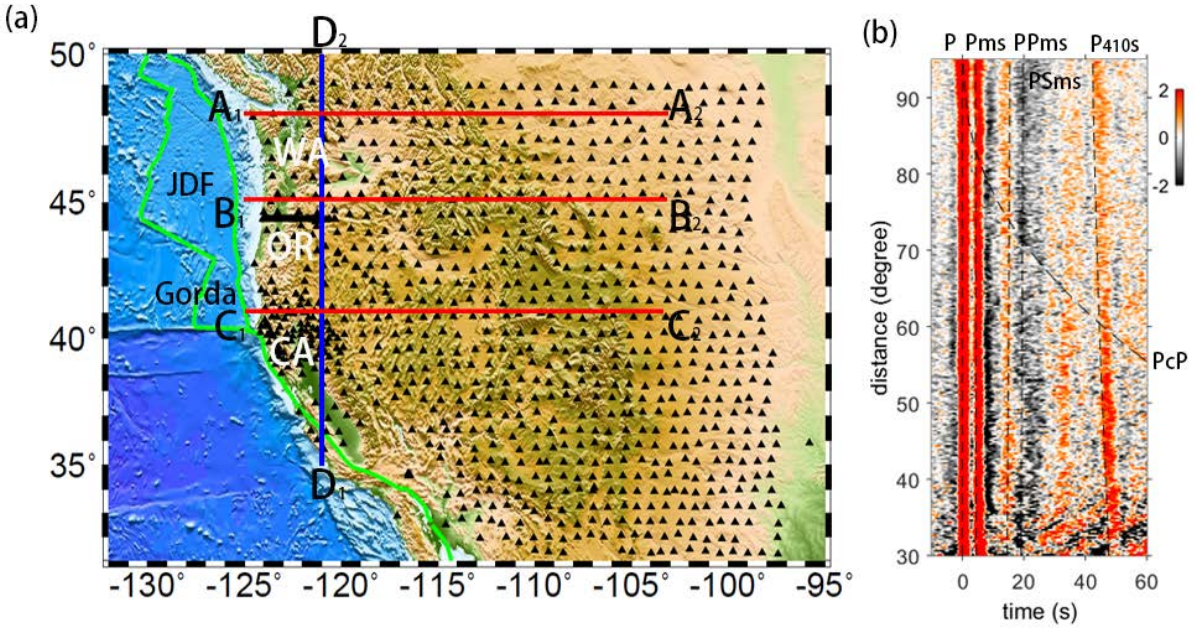

Figure 4.1: (a) Map of Western U.S. and broadband seismic stations (black triangles) used in this study. (b) Time-distance seismic section for all the receiver functions used in this study. The primary signal (Pms) and later multiples are labeled.

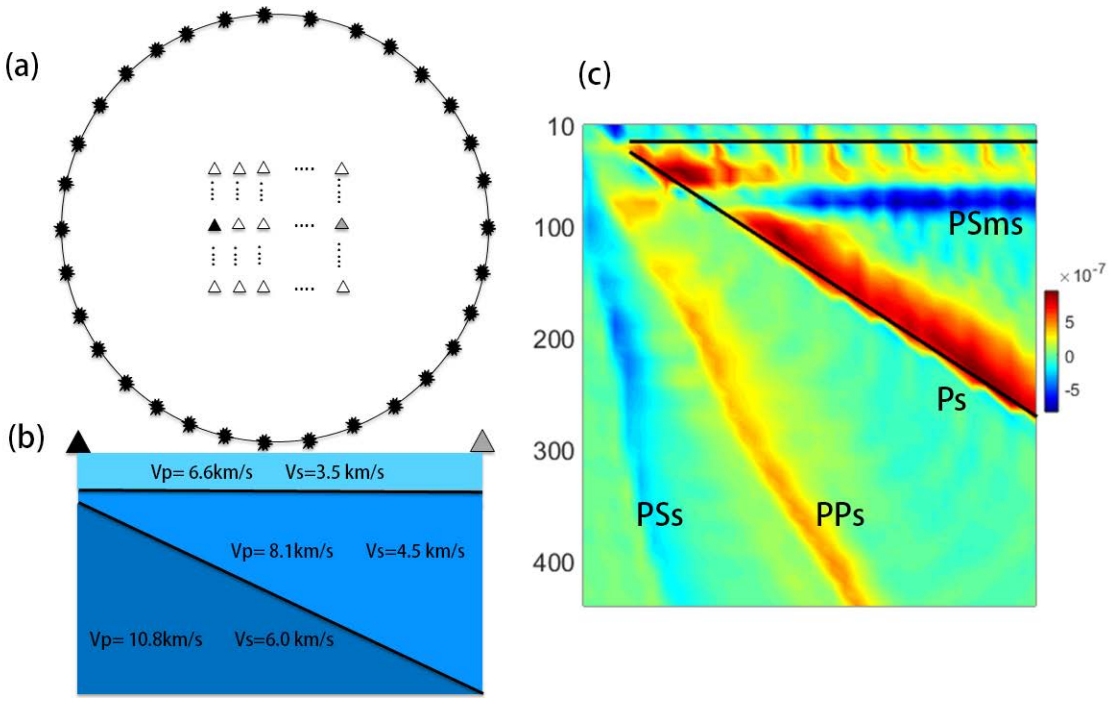

Figure 4.2: (a) Schematic figure (not to scale) showing the earthquake source distribution map used for synthetics. A circle of sources surrounds our grid of surface seismic stations (triangles), which is roughly 80° (epicentral distance) from the sources. (b) A vertical section though our synthetic velocity model. (c) The final migrated results using our Kirchhoff migration method. Solid black lines mark the real location of the model discontinuity. The primary signal and late multiples are labeled on the figures.

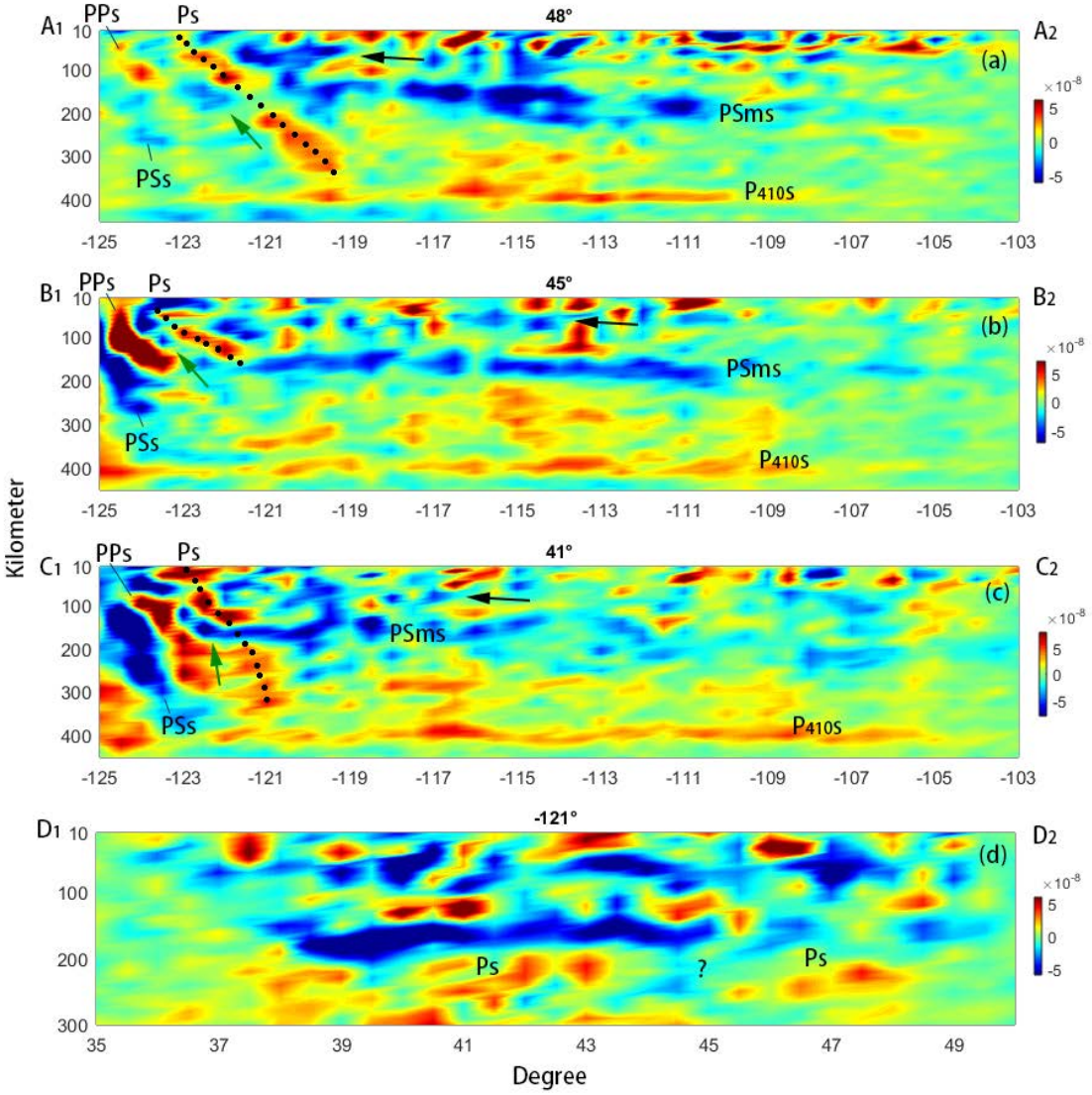

Figure 4.3: Migrated seismic cross-section for (a) A1-A2 profile at 48°N; (b) B1-B2 profile at 45°N; (c) C1-C2 profile at 41°N; (d) D1-D2 profile at 121°W; from low-pass-filtered data at 0.2Hz period. The black dotted line emphasizes the prominent discontinuity related to the slab. The position of migrated primary signal (Ps) and later multiples are labeled on the figures. P410s indicates the 410km discontinuity. The black arrows in (a, b, c) show the continental LAB (blue and discontinuous), and green arrows in (a, b) show the oceanic LAB. The question mark in (d) shows the gap in the primary Ps arrival.

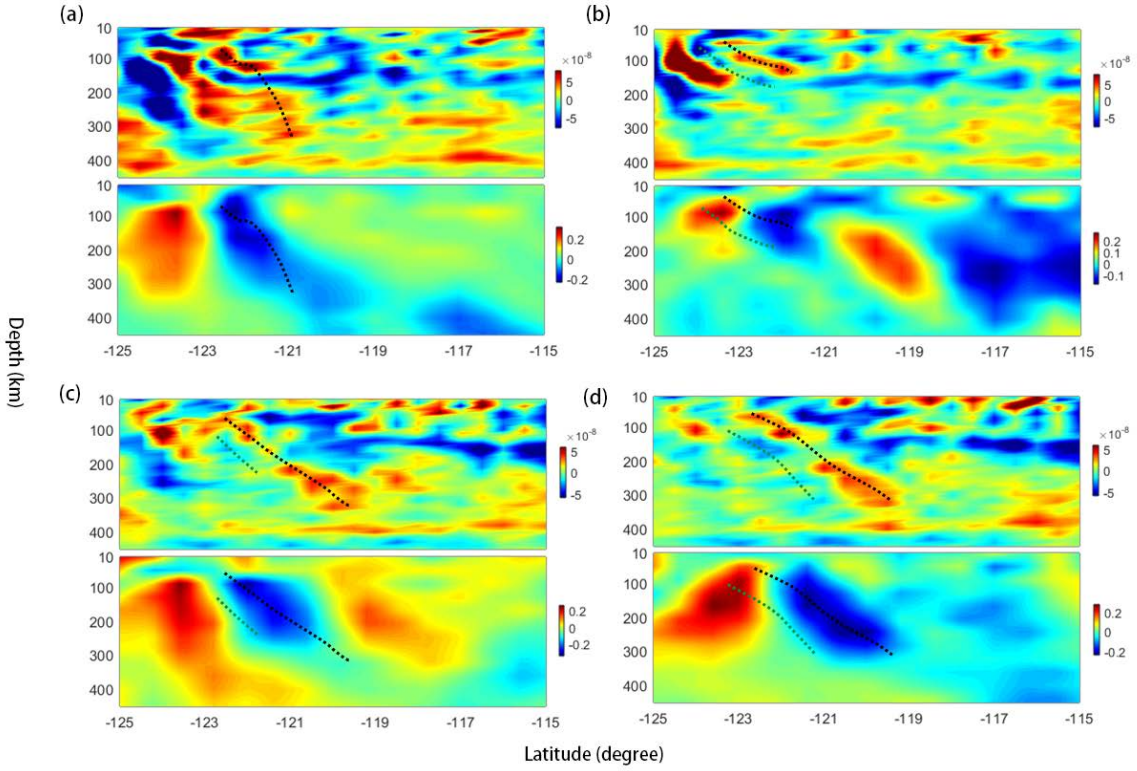

Figure 4.4: Comparison between our reflectivity model (0.2 Hz dataset) (upper panel in each pair) and a teleseismic tomography model (lower panel in each pair) [Hawley et al., 2016] at (a) 41°N; (b) 45°N; (c) 47°N; and (d) 48°N. The black dotted line emphasizes the prominent discontinuity related to the slab as imaged by receiver functions. The green dotted line shows the bottom of the slab from the receiver function study also.

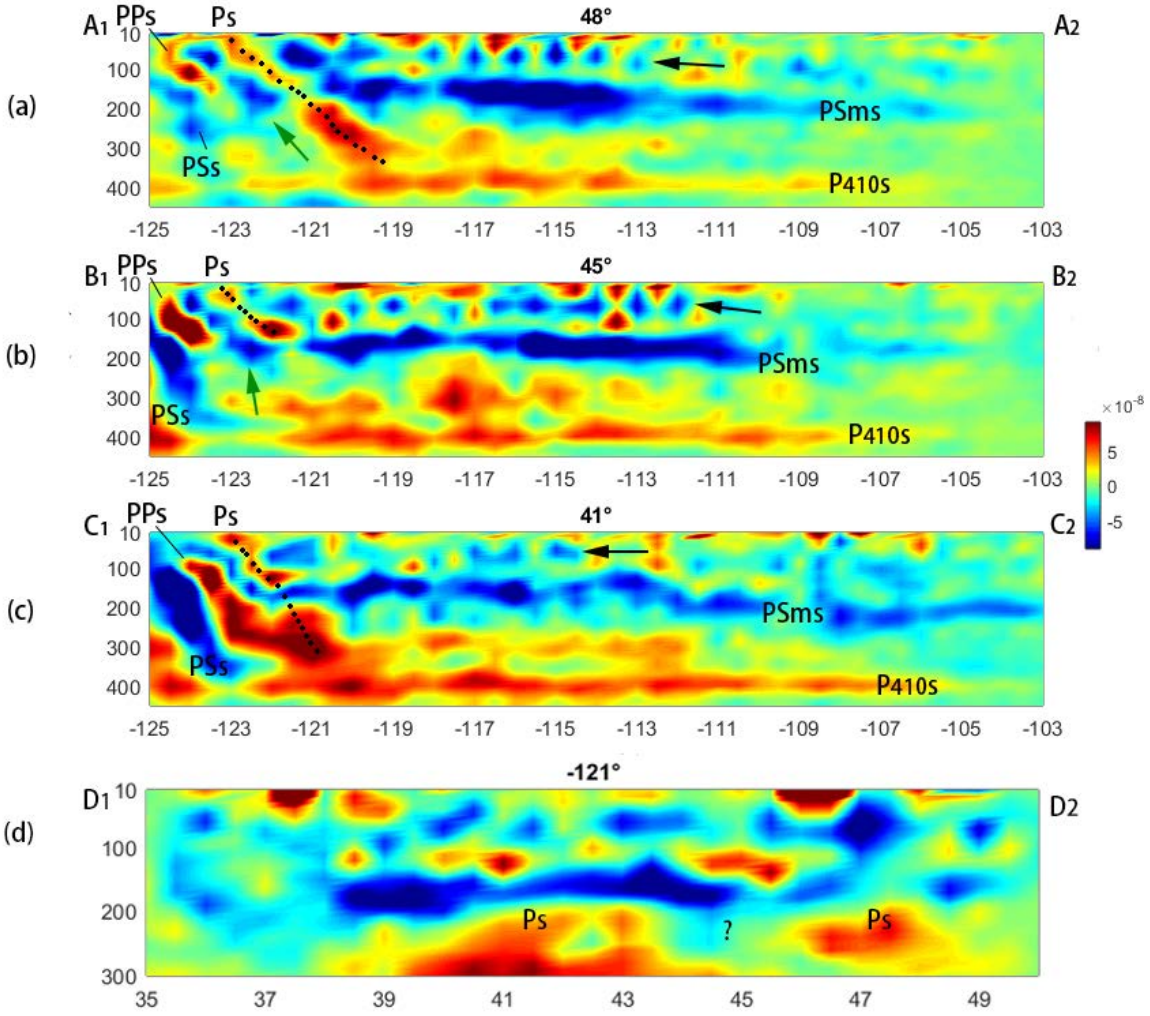

Figure 4.5: Migrated seismic cross-section for (a) A1-A2 profile at 48°N; (b) B1-B2 profile at 45°N; (c) C1-C2 profile at 41°N; (d) D1-D2 profile at 121°W; from low-pass-filtered data at 0.1Hz period. The black dotted line emphasizes the prominent discontinuity related to the slab. The position of migrated primary signal (Ps) and later multiples are labeled on the figures. P410s indicates the 410km discontinuity. The black arrows in (a, b, c) show the continental LAB (blue and discontinuous), and green arrows in (a, b) show the oceanic LAB. The question mark in (d) shows the gap in the primary Ps arrival.

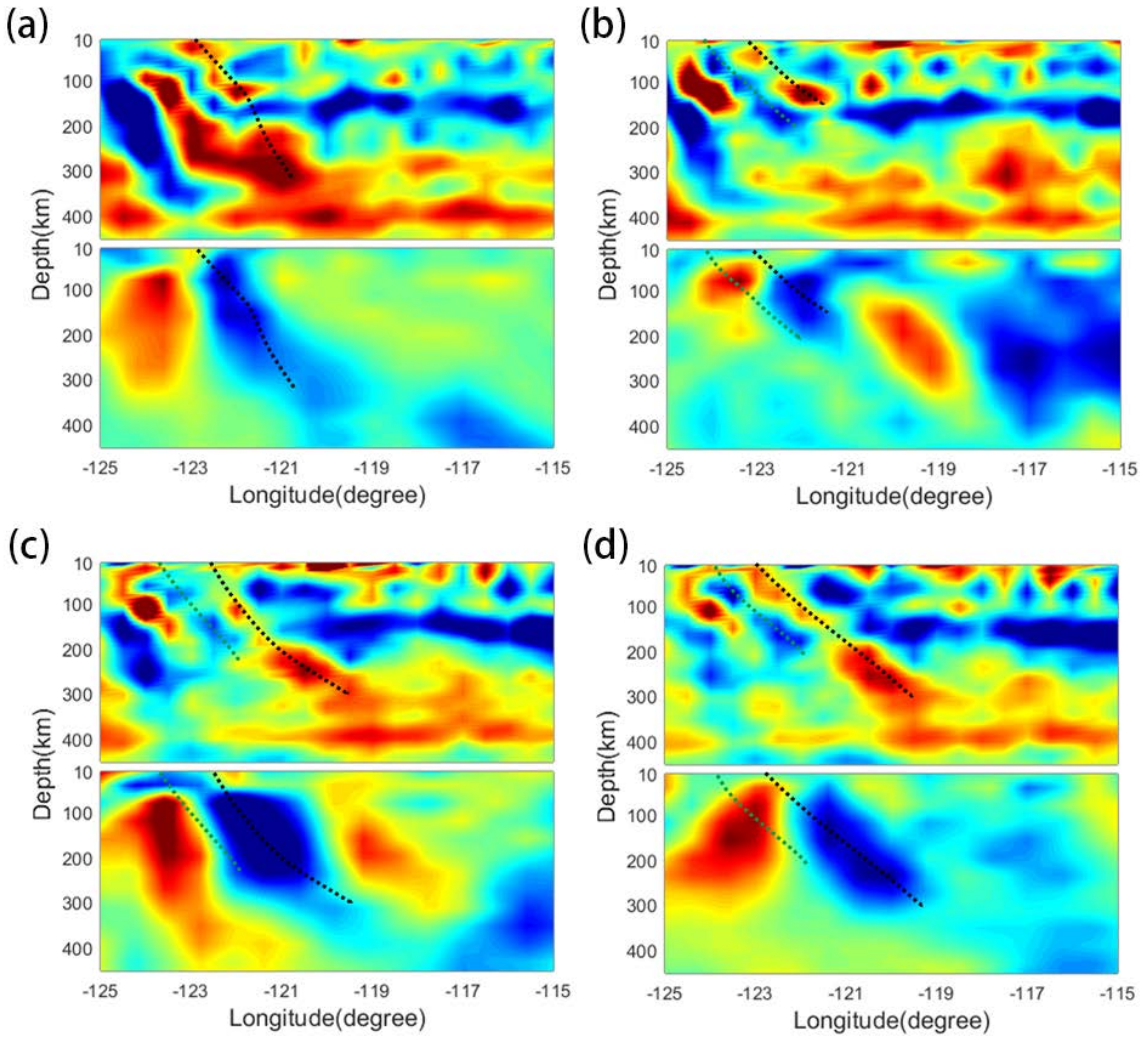

Figure 4.6: Comparison between our reflectivity model (0.1 Hz dataset - upper panel in each pair) and a teleseismic tomography model (lower panel in each pair) [Hawley et al., 2016] at (a) 41°N; (b) 45°N; (c) 47°N; and (d) 48°N. The black dotted line emphasizes the prominent discontinuity interpreted as the slab imaged by receiver functions. The green dotted line shows the bottom of the slab from the receiver function study also.

4.7 Bibliography

Audet, P., M. G. Bostock, N. I. Christensen, and S. M. Peacock (2009), Seismic evidence for overpressured subducted oceanic crust and sealing of the megathrust, Nature, 457, 76 – 78.

Audet, P., M. G. Bostock, D. C. Boyarko, M. R. Brudzinski, and R. M. Allen (2010), Slab morphology in the Cascadia fore arc and its relation to episodic tremor and slip, J. Geophys. Res., 115, B00A16, doi:10.1029/2008JB006053.

Bassin, C., G. Laske, and G. Masters (2000), The Current Limits of Resolution for Surface Wave Tomography in North America, EOS Trans AGU, 81, F897.

Bell, S., Y. Ruan, and D. W. Forsyth (2016), Ridge asymmetry and deep aqueous alteration at the trench observed from Rayleigh wave tomography of the Juan de Fuca plate, J. Geophys. Res. Solid Earth, 121, doi:10.1002/2016JB012990.

Bercovici, D., G. Schubert, and Y. Ricard (2015), Abrupt tectonics and rapid slab detachment with grain damage, Proc. Natl. Acad. Sci. U.S.A., 112, 1287–1291, doi:10.1073/pnas.1415473112.

Bostock, M. G. (1999), Seismic waves converted from velocity gradient anomalies in the Earth's upper mantle, Geophys. J. Int., 138, 747–756.

Bostock, M. G., R. D. Hyndman, S. Rondenay, and S. M. Peacock (2002), An inverted continental Moho and serpentinization of the forearc mantle, Nature, 417, 536–538.

Bostock, M. G. (2013), The Moho in subduction zones, Tectonophysics, 609, 547–557, doi:10.1016/j.tecto.2012.07.007.

Burdick, S., et al. (2010), Model update January 2010: Upper mantle heterogeneity beneath North America from traveltime tomography with global and USArray Transportable Array data, Seismol. Res. Lett., 81, 689–693.

Cheng, C., T. Bodin, and R. M. Allen (2016), Three-dimensional pre-stack depth migration of receiver functions with the fast marching method: A Kirchhoff approach, Geophys. J. Int., 205(2), 819–829, doi:10.1093/gji/ggw062.

Dahlen, F.A., G. Nolet, and S.-H. Hung (2000), Fr´echet kernels for finite-frequency traveltime—I. Theory, Geophys. J. Int., 141, 157–174.

Ford, H. A., M. D. Long, and E. A. Wirth (2016), Midlithospheric discontinuities and complex anisotropic layering in the mantle lithosphere beneath the Wyoming and

Superior Provinces, J. Geophys. Res. Solid Earth, 121, 6675–6697, doi:10.1002/2016JB012978.

Gao, H. (2016), Seismic velocity structure of the Juan de Fuca and Gorda plates revealed by a joint inversion of ambient noise and regional earthquakes, Geophys. Res. Lett., 43, 5194 – 5201, doi:10.1002/2016GL069381.

Hacker, B. R., S. M. Peacock, G. A. Abers, and S. D. Holloway (2003), Subduction factory: 2. Are intermediate-depth earthquakes in subducting slabs linked to metamorphic dehydration reactions?, J. Geophys. Res., 108(B1), 2030, doi:10.1029/2001JB001129.

Hacker, B., and G.A. Abers (2004), Subduction factory 3. An excel worksheet and macro for calculating densities, seismic wave speeds, and H2O contents of minerals and rocks at pressure and temperature, Geochem. Geophys. Geosyst. 5, Q01005.

Han, S., S. M. Carbotte, J. P. Canales, M. R. Nedimović, H. Carton, J. C. Gibson, and G. W. Horning (2016), Seismic reflection imaging of the Juan de Fuca plate from ridge to trench: New constraints on the distribution of faulting and evolution of the crust prior to subduction, J. Geophys. Res. Solid Earth, 121, 1849 – 1872, doi:10.1002/2015JB012416.

Hansen, S. M., K. G. Dueker, and B. Schmandt (2015), Thermal classification of lithospheric discontinuities beneath USArray, Earth Planet. Sci. Lett., 431, 36–47.

Hopper, E., and K. M. Fischer (2015), The meaning of midlithospheric discontinuities: A case study in the northern U.S. craton, Geochem. Geophys. Geosyst., 16, 4057–4083, doi:10.1002/2015GC006030.

Langston, C. A. (1977), Corvallis, Oregon, crustal and upper mantle receiver structure from teleseismic P and S waves, Bull. Seismol. Soc. Am., 67, 713 – 724.

Langston, C. A. (1981), Evidence for the subducting lithosphere under southern Vancouver Island and western Oregon from teleseismic P wave conversion, J. Geophys. Res., 86, 3857 – 3866.

Levander, A., and M. S. Miller (2012), Evolutionary aspects of the lithosphere discontinuity structure in the western U.S, Geochem. Geophys. Geosyst., 13, Q0AK07, doi:10.1029/2012GC004056.

Ligorrìa, J., and C. Ammon (1999), Iterative deconvolution and receiver function estimation, Bull. Seismol. Soc. Am., 85, 1395 – 1400.

MacKenzie, L.S., G.A. Abers, S. Rondenay, and K.M. Fischer (2010), Imaging a steeply dipping subducting slab in southern Central America, Earth Planet. Sci. Lett., 296, 459 – 468.

Martin-Short, R., R. M. Allen, I. D. Bastow, E. Totten, and M. A. Richards (2015), Mantle Flow geometry from ridge to trench beneath the Gorda-Juan de Fuca plate system, Nat. Geosci., 8, 965–968.

McCrory, P. A., J. L. Blair, F. Waldhauser, and D. H. Oppenheimer (2012), Juan de Fuca slab geometry and its relation to Wadati-Benioff zone seismicity, J. Geophys. Res., 117, B09306, doi:10.1029/2012JB009407.

Nedimović, M. R., D. R. Bohnenstiehl, S. M. Carbotte, J. P. Canales, and R. P. Dziak (2009), Faulting and hydration of the Juan de Fuca plate system, Earth Planet. Sci. Lett., 284(1 – 2), 94 – 102, doi:10.1016/j.epsl.2009.04.013.

Obrebski, M., R. M. Allen, M. Xue, and S. -H. Hung (2010), Slab-plume interaction beneath the Pacific Northwest, Geophys. Res. Lett., 37, L14305, doi:10.1029/2010GL043489.

Obrebski, M., R. M. Allen, F. Pollitz, and S. H. Hung (2011), Lithosphere-asthenosphere interaction beneath the Western United States from the joint inversion of body-wave traveltimes and surface-wave phase velocities, Geophys. J. Int., 185, 1003–1021.

Peacock, S. M., K. Wang, and A. M. McMahon (2002), Thermal structure and metamorphism of subducting oceanic crust—Insight into Cascadia intraslab earthquakes, U.S. Geol. Surv. Open-File Rep., 02–328, 123 – 126.

Rawlinson, N. and M. Sambridge (2004), Wave front evolution in strongly heterogeneous layered media using the fast marching method, Geophys. J. Int., 156(3), 631–647.

Rondenay, S. (2009), Upper mantle imaging with array recordings of converted and scattered teleseismic waves, Surv. Geophys., 30, 377–405.

Schmandt, B., K. Dueker, E. Humphreys, and S. Hansen (2012), Hot mantle upwelling across the 660 beneath Yellowstone, Earth planet. Sci. Lett., 331, 224–236.

Tauzin, B., R. D. van der Hilst, G. Wittlinger, and Y. Ricard (2013), Multiple transition zone seismic discontinuities and low velocity layers below western United States, J. Geophys. Res. Solid Earth, 118, 2307–2322, doi:10.1002/jgrb.50182.

Tauzin, B., T. Bodin, E. Debayle, J. P. Perrillat, and B. Reynard (2016), Multi-mode conversion imaging of the subducted Gorda and Juan de Fuca plates below the North American continent, Earth Planet. Sci. Lett., 440, 135-146.

Hawley, W. B., R. M. Allen, and M. A. Richards (2016), Tomography reveals buoyant asthenosphere accumulating beneath Juan de Fuca plate, Science, 353, 6306, doi:10.1126/science.aad8104.

Yuan, H., and B. Romanowicz (2010), Lithospheric layering in the North American craton, Nature, 466, 1063–1068, doi:10.1038/nature09332.

Chapter 5

Least-square migration: an introduction

5.1 Introduction

In Chapter 3, we present the novel 3D pre-stack Kirchhoff depth migration method for teleseismic receiver functions. In Chapter 4 we saw the successful application of this method to the Cascadia subduction plate. Migration is now recognized as the most important process in seeking the subsurface seismic reflectivity structures. But we also note that in the real data application (Cascadia, chapter 4), there exists unsolved problems in the final image. For example, the narrow band low frequency reflectivity feature in the image comes from the intrinsic property of the migration algorithm. Also, the final migration image is contaminated by different modes of multiple, which makes it hard to reveal the true structure.

In this chapter, I would like to introduce a novel migration technique: least-squares migration which is aiming to tackle these unsolved issues existing in the traditional migration process. Most of the synthetic work in this chapter is done with small scale (compare with the scale of continent) seismic reflection data. I would like to lay out the main idea of this technique and show the potential of applying it in imaging large continental scale structures.

Equation (1) represents the Born first order approximation of the seismic data generation. A is the kernel matrix obtained by ray tracing, x is the real reflectivity and b is the observed data. Before migration what we have is data b and what we want is x. If one thinks about the procedure of the migration procedure in terms of equation (2), it is essentially a transpose operator of the kernel matrix A and multiplied by the observed data b. The $\tilde{x}$ is the image obtained by migration and is an approximation of real reflectivity x. The data b is reflection data in the small scale case (reflection seismology) and is receiver function data in large scale case. Equation (1) can represent most geophysical inversion problems. For example, in finite frequency tomography the x is the velocity perturbation and in full waveform inversion x is velocity structure, A is the Hessian matrix and b is gradient vector.

$$Ax = b \tag{1}$$

$$\tilde{x} = A^T b \tag{2}$$

We are aiming for the broadband true amplitude reflectivity structure of the earth, the process of which is an inversion, rather than a migration. This means we need to solve for equation (3) to get real reflectivity structure x. But the migration can only give us the approximate transposed solution $\tilde{x}$. The difference between migration and inversion can be observed from a simple Matlab example in Fig. 5.1. In this example, we build a Gaussian random matrix A (Fig. 5.1(d)). So the Hessian matrix A^TA is a nonsingular diagonal dominant and we can invert it directly. We generate data b by multiplying A with the real reflectivity x (Fig. 5.1(a)). Then we can migrate it according to equation (1). The migrated reflectivity (Fig. 5.1(b)) is noisier with incorrect amplitudes when compared to the inverted solution (Fig. 5.1(c)). It is also clear that the spectrum of the reflectivity is not correct either.

In fact, the migration result approaches the true inverted results when assuming perfect acquisition, i.e. the small scale reflection case, with regular surface sampling, infinite recording aperture, and unaliased seismic data, which cannot be achieved in practice [Zhang et al., 2013].

$$x = (A^TA)^{-1}A^Tb \qquad (3)$$

In the past, the development of prestack depth migration has focused on improving its propagation operators to tackle the challenges of imaging in increasingly complicated subsurface structure, from ray-tracing-based Kirchhoff migration [Schneider, 1978] to the wave-propagation-based one-way wave equation migration [Claerbout, 1971] and reverse time migration (RTM) [McMechan, 1983; Whitmore, 1983]. To remove the acquisition footprint and to improve the quality of seismic imaging, least-squares migration (LSM) has been proposed to seek an inverted image, which generates the simulated data best matching the amplitude of the seismic data. The idea of LSM was first applied to Kirchhoff migration [Schuster, 1993; Nemeth et al., 1999], then generalized to one-way wave equation migration [Wang et al., 2005], and now applied to RTM [Dai et al., 2011]. Now least-squares migration is applied widely in exploration geophysics and is considered as the next generation of imaging. In the real case, depending on the scale of the problem and frequency of the data, the Hessian matrix A^TA can be very large and ill-conditioned, which can make using Newton's method or the Gaussian-Newton method to solve for the inversion of the Hessian extremely computationally expensive. Currently people solve with an iterative inversion process to approach the real inversion solution. That is, in a least-square sense, define an objective function as in equation (4), and use a conjugate-gradient based linear inversion method to minimize it. So the idea is: by matching the observed data, the migration image will be updated step by step and get close to the real reflectivity, which also means that the frequency band will be increased and the artificial multiples will be removed.

$$f(\tilde{x}) = \frac{1}{2}\|b - A\tilde{x}\|^2 \qquad (4)$$

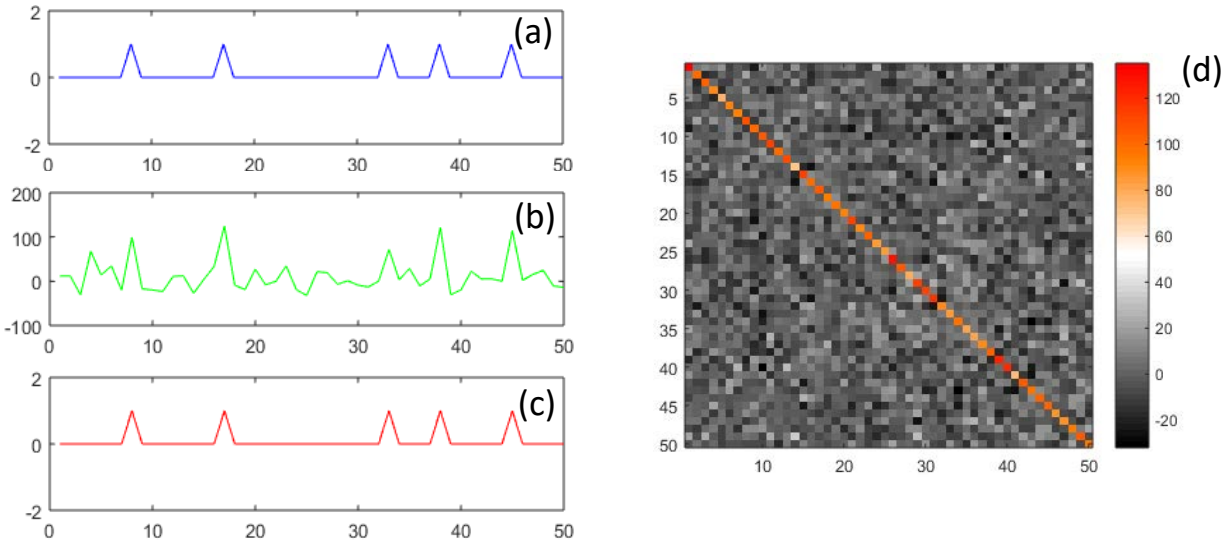

Figure 5.1: (a) The original signal which is also the vector x in equation (1). (b) The migrated signal which is also the vector $\tilde{x}$ in equation (2). (c) The inverted structure signal, the vector x in equation (3). (d) The Hessian matrix of this numerical example.

In the following sections, the results I get for one-way wave equation migration and reverse time migration are based on this linear gradient inversion scheme. Both results are using seismic reflection data.

5.2 Least-square wave equation migration

5.2.1 Methodology:

Wave-equation migration consists of numerically extrapolating source and receiver wavefields into the subsurface, where an imaging principle is applied [Claerbout, 1971]. In this study, the migration process is a hybrid migration method, named "Fourier finite-difference (FFD) migration," wherein the downward-continuation operator is split into two downward-continuation operators: one operator is a phase-shift operator for a chosen constant background velocity, and the other operator is an optimized finite difference operator for the varying component of the velocity function. If there is no variation of velocity, then only a phase-shift operator will be applied. If there is a strong variation of velocity, then the phase-shift component is suppressed and the optimized finite-difference operator will be fully applied. Readers should refer to the original paper [Ristow and Rühl, 1994] for more technical details if interested.

During this synthetic test, the Sigsbee model is used. The stratigraphic velocity structure is showed in Fig. 5.2. Sigsbee is a constant density acoustic model released in September 2001 and contains both low velocity sedimentary layers and high velocity salt body. It does not contain free surface multiples and almost no internal multiples due to a very low contrast water bottom, but it is over a sub-salt structure that is difficult to image because of the illumination. And there are a total of 500 sources distributed evenly at the sea surface.

The operator here is essentially a one-way operator. Compared with the numerical finite difference two-way operator, it is much faster and cheaper in computation but the drawback is it cannot accommodate high-dip structure. We use both point source and data reinjected at the stations as the source term and use the total wavefield at the receiver side. When imaging primary reflections, the source wavefield is initiated by a point source and propagated into the earth. The upgoing wavefield, used as receiver wavefield at the surface, is obtained by deghosting the data. These surface recordings contain not only primary reflections but also multiple-scattered energy. When imaging primary reflections, the multiple-scattered waves are treated as noise that typically is attenuated in processing (e.g., surface-related multiple removal). Fig. 5.3(a) shows the original migration result using the FFD algorithm. From this image, one can notice that the main reflectivity structure has been recovered well at both the sedimentary layer and the salt layer. However, in the sub-salt region, which is lacking seismic ray illumination, the structure is poorly mapped. At the bottom layer the reflectivity is imaged but with an illumination hole. Also we can notice the image is contaminated by artificial crosstalk because we do include the multiples in the data.

Least-squares migration can account for these problems in the original wave equation migration buy fitting the synthetic data to the real data. For the least-square migration, the matrix A^T is the migration operator which is the same as we have been using. The

matrix *A* is the operator for generating synthetic data given a velocity structure and a reflectivity model. In this test, we use a Born modelling operator as the matrix *A* to generate synthetic data.

5.2.2 Synthetic results:

For inversion, we use a LSQR inversion method, which is developed as a conjugate-gradient type method for solving sparse linear equations and sparse least-squares problems. Gradient is updated every iteration and added to the original image by multiplying a scale factor. Fig. 5.3(a) shows the inverted least-squares image after 20 iterations. Compared to the original migration image, the image quality has been improved substantially. The main structure has been preserved well. In addition, the least-squares inversion improves the illumination by iteratively fitting the synthetic to real data. The image has more balanced amplitude overall. The sub-salt region which is invisible to migration before, is revealed by the least-square migration.

Fig. 5.3(b,c) shows the F-K diagram and spectrum of the migration image. Fig. 5.4(b,c) shows F-K diagram and spectrum for least-square image for comparison. One can see the spatial resolution and temporal resolution of the image is broadly improved by least-square inversion.

Another important feature least-squares migration brings is attenuating the crosstalk during the inversion process. That is because the synthetic data generated by the multiple structure of migration can't fit the real data, the LSQR will remove the multiples iteratively. Because the multiple data generate the largest misfit, the inversion algorithm will remove it at the first few iterations. Fig. 5.5 shows the objective function of the least-square inversion. It shows the misfit decreases to 10 percent of the original at iteration 20.

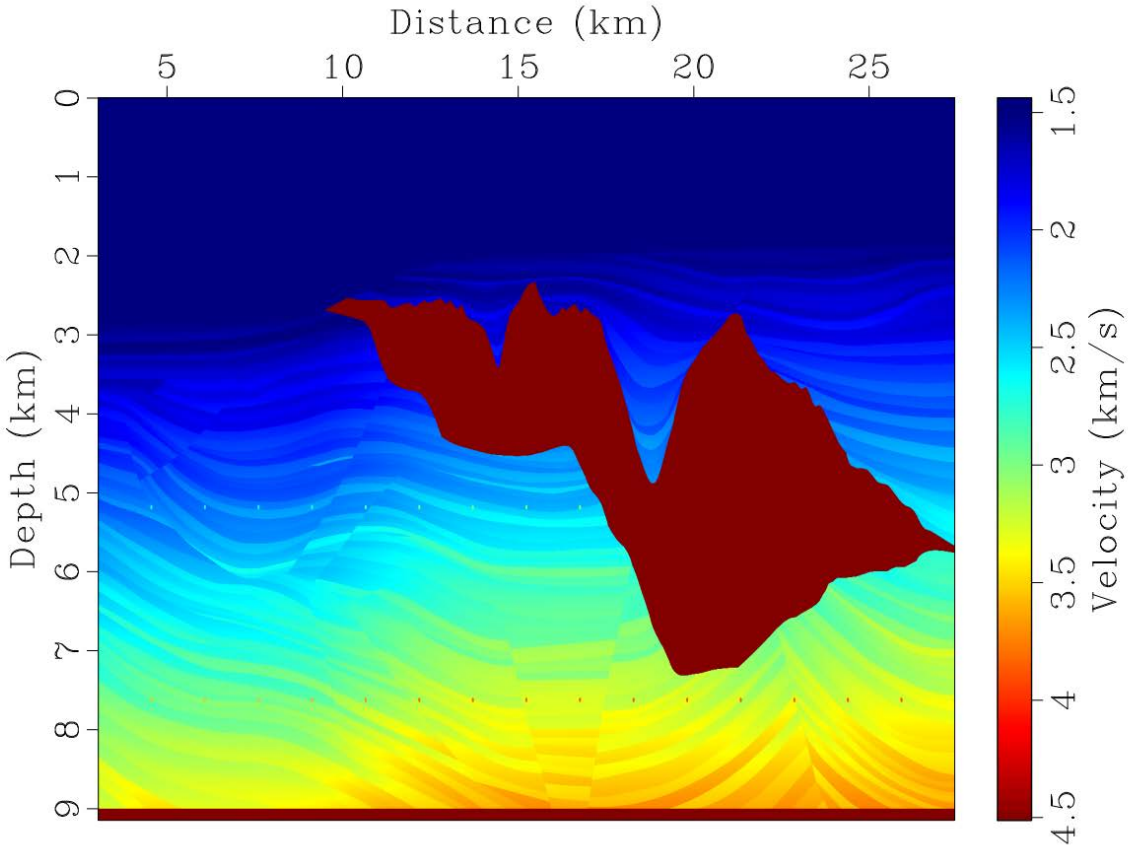

Figure 5.2: The stratigraphic velocity model of Sigsbee2b.

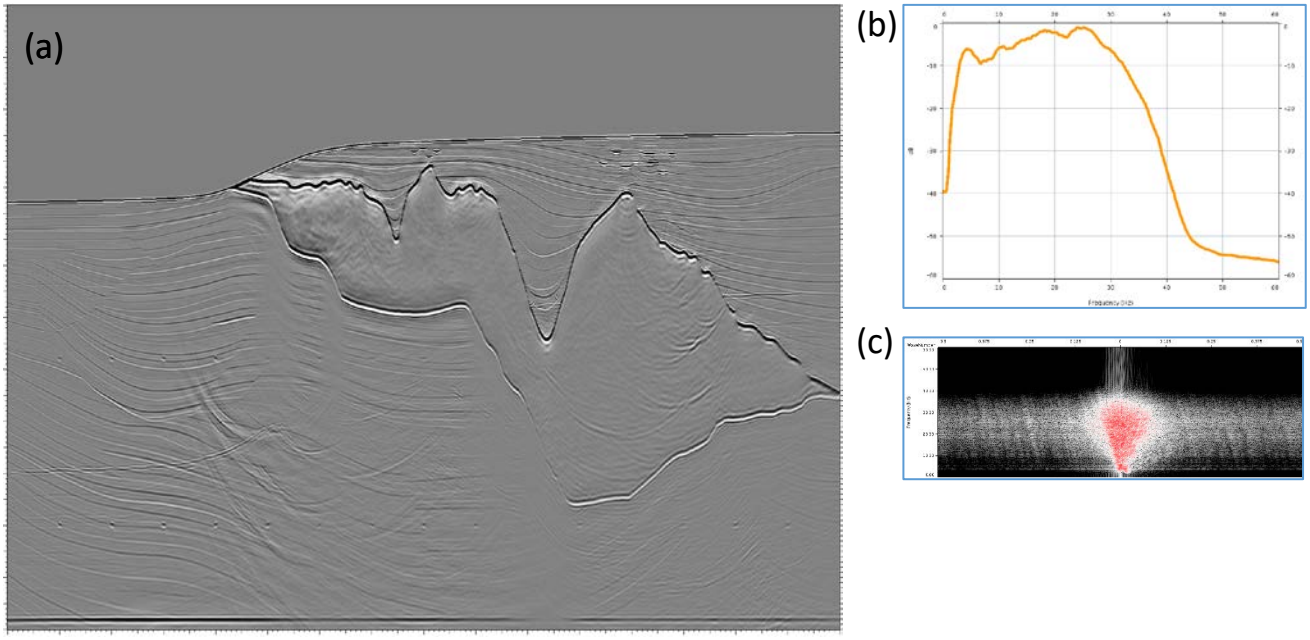

Figure 5.3: (a) The migration result of the Sigsbee2b model, with both primary and migration data. (b) The frequency spectrum of the image (a) in the sediment sections. (c) The f-k spectrum of image (a).

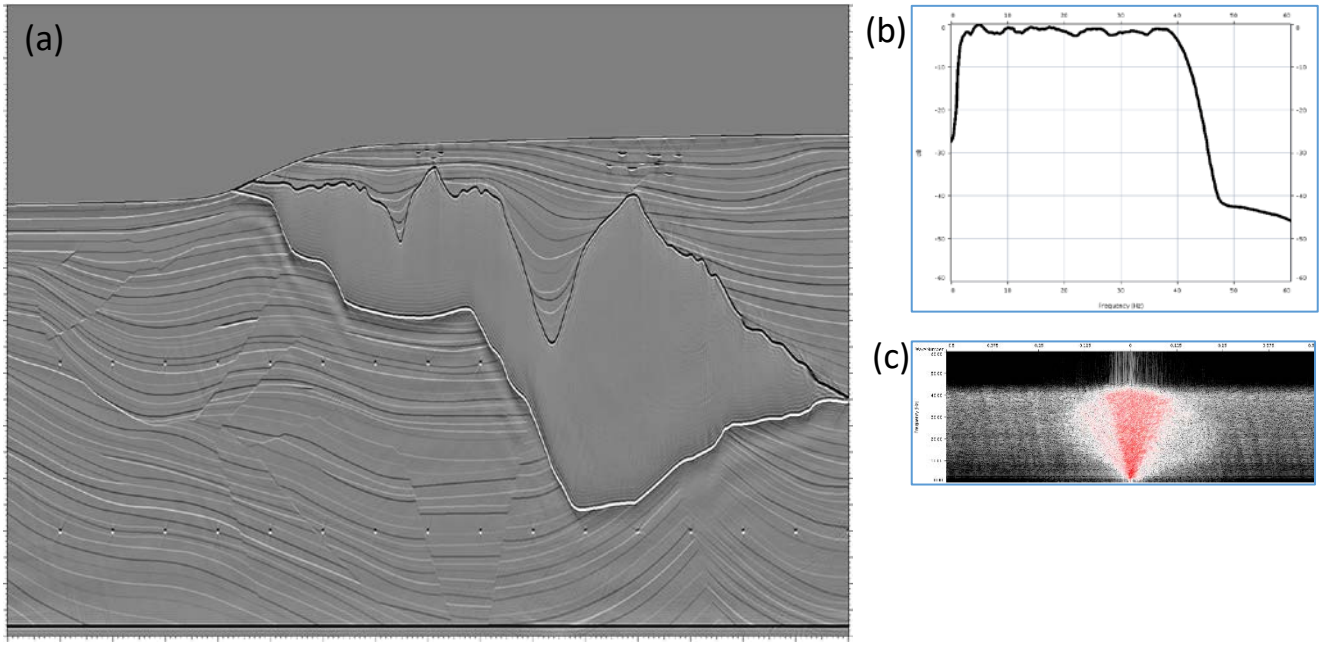

Figure 5.4: (a) The least-squares inversion result of the Sigsbee2b model, with both primary and migration data. (b) The frequency spectrum of the image (a) in the sediment sections. (c) The f-k spectrum of image (a).

5.3 Least-square reverse time migration

5.3.1 Methodology:

We have seen the performance of the least-squares inversion on one-way wave equation migration. For complicated structures, reverse time migration (RTM) is the state-of-the-art imaging technology. RTM is now the most widely used migration algorithm in reflection seismology. It uses true amplitude migration theory, which aims to automatically compensate for the geometric spreading occurring during the migration process and obtain the angle-dependent reflectivity. It has been developed by Zhang and Sun (2009) and Xu et al. (2011). For a zero-phased shot record $D(x, y; t; x_s)$, with the shot at x_s and receivers at x_r, the RTM algorithm can be summarized as forward propagation of the source wavefield Ps (Zhang et al., 2007):

$$\begin{cases} \left(\frac{1}{v(x)}\frac{\partial^2}{\partial t^2} - \Delta\right) Ps(x; t; x_s) = 0 \\ Ps(x, y, z = 0) = \delta(x - x_s)\int_0^{t1} S(t)dt \end{cases} \tag{5}$$

and backward propagation of the receiver wavefield Pr by reducing time:

$$\begin{cases} \left(\frac{1}{v(x)}\frac{\partial^2}{\partial t^2} - \Delta\right) Pr(x; t; x_s) = 0 \\ Pr(x, y, z = 0) = D(x, y; t; x_s) \end{cases} \tag{6}$$

where x is the subsurface imaging location, $v(x)$ is velocity, and Δ denotes the Laplacian operator. As generating angle domain common image gathers can be very computational expensive, geophysicists choose to use the full stacked image by a cross-correlation:

$$r(x) = \iint Ps(x; t; x_s)\mathrm{Pr}(x; t; x_s)dtdx_s \tag{7}$$

As with one-way wave equation migration, RTM assumes perfect acquisition with regular surface sampling, infinite recording aperture, and unaliased seismic data. Without these requirements, the image result would be biased. Here again we are also trying to use the least-square method to further improve the RTM image.

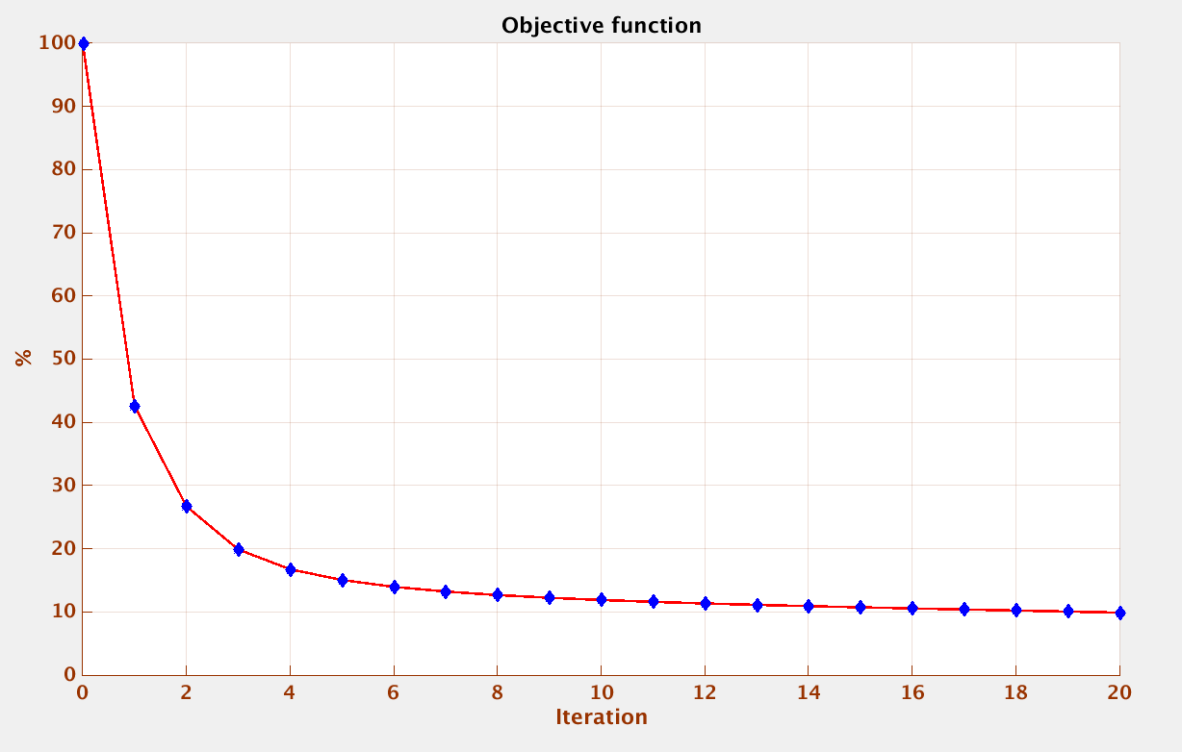

Figure 5.5: The objective function of the least-square inversion performed on Sigsbee2b model.

In this research, we use a different framework of least-squares RTM by using a different objective function. The reason is that, in practice, it is not an easy task to directly apply the (conventional) amplitude-matching-based least-squares RTM (LSRTM) (equation (4)). The earth is at least a viscoelastic medium with density variations; hence, it is much more complicated than the models we use to propagate acoustic wavefields in seismic imaging. As a result, the amplitude matching is never perfect. Also, it is difficult to define a good source signature in the modeling. The challenge of determining source strength, which can vary from source to source, is even greater. So instead of matching the amplitude of seismic data trace by trace, we use the following cross-correlation based objective function in the time domain:

$$f(r) = -\iiint \frac{d(x_r;t;x_s)\cdot D(x_r;t;x_s)}{\sqrt{\int (d)^2 dt}\sqrt{\int (D)^2 dt}}\, dt dx_s dx_r \qquad (8)$$

The negative sign on the right side is introduced so that the optimal solution is achieved when the objective function reaches its minimum. The cross-correlation relaxes on the amplitude matching and uses phase information to measure the closeness between the simulated data and the observed seismic data. The goal is to find the optimal image r, which maximizes the cross-correlation between the observed seismic and simulated data at zero lag, or equivalently, to minimize the objective function.

5.3.2 Synthetic results:

In this synthetic test, we use a Marmousi model, which is also widely used in reflection seismology. Fig. 5.6 shows the stratigraphic velocity model for Marmousi. It is composed by complicated low velocity sedimentary layers and high velocity salt layers.

For the inversion, we use a non-linear conjugate-gradient method. Fig. 5.7(a) shows the original migration result using the RTM algorithm. From this image, one can see that as before the main reflectivity structure has been recovered well at both the sedimentary layer and the salt layer. However, in the sub-salt region, the structure is poorly mapped. Fig. 5.7(b) shows the result after least-square reverse time migration using equation (8). We can identify that the least-squares RTM is not only just balancing the overall amplitude of the initial image, but it also reveals structural detail that are otherwise unidentifiable.

In seismic reflection data acquisition, the source is below the sea surface. So, we can easily get reflections from the sea surface which makes the data to appear as “ghosted” data. Normally the data we use for migration is before deghosting (removal of the ghost effect). So, as a consequence, the original image is displayed as a ghosted image. The least-square migration however can remove the ghost effect on the image and improve the resolution. By matching the real data, the ghost effect in the image is removed. Overall, the inverted image is amplitude balanced with improved continuity and reveals more detailed structures.

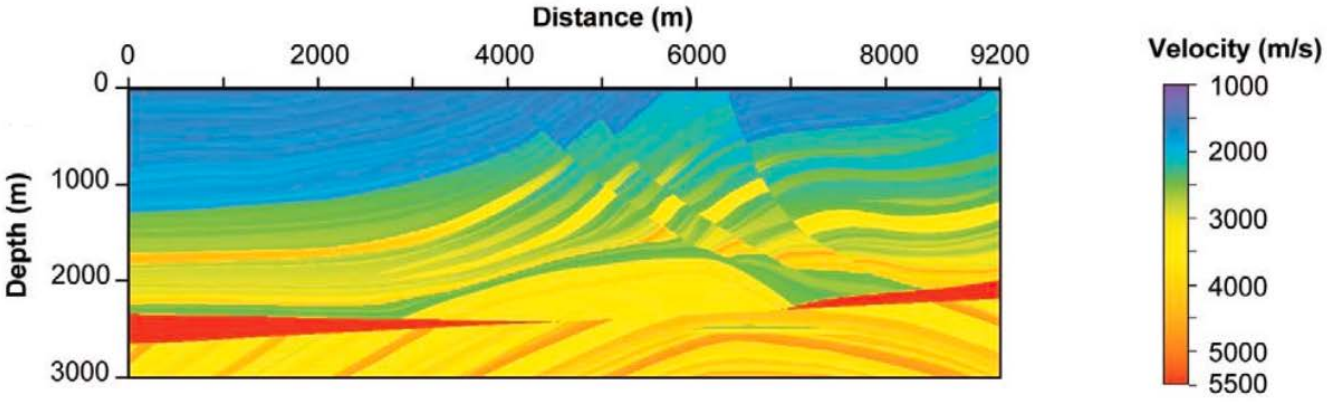

Figure 5.6: The stratigraphic velocity model of Marmousi.

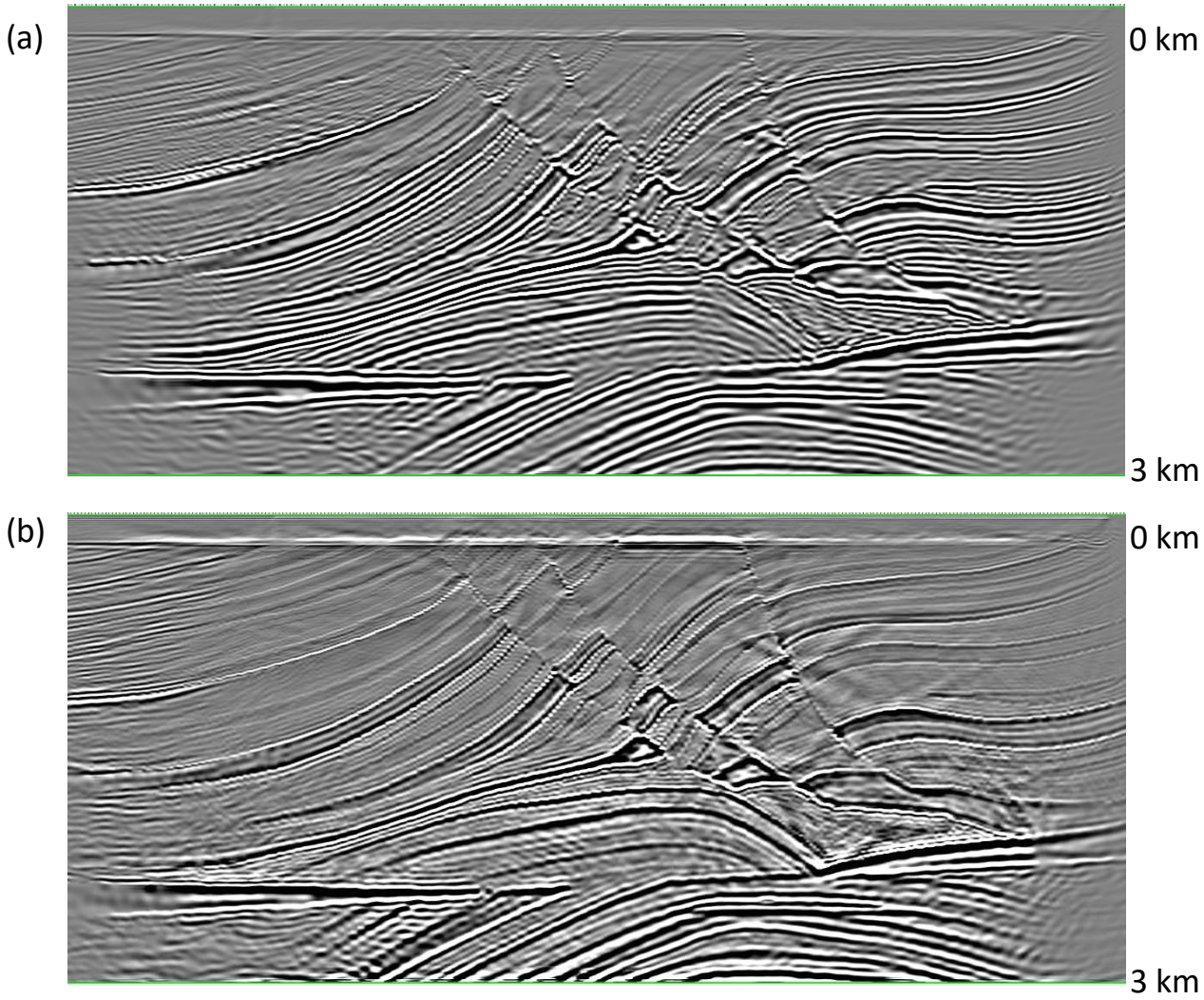

Figure 5.7: (a) The original migration result of Marmousi model. (b) The correlative least-squares migration result of Marmousi model.

5.4 Summary

We have presented the concept of least-squares migration in this chapter. We have seen that the least-squares migration theory works for both wave equation migration and reverse time migration. The improvements of the least-squares inversion on the original migration has been shown, on the Sigsbee and Marmousi models respectively. The synthetic tests here show that least-square migration is an attractive technique for improving image spatial and time resolution, removing the ghost effect, improving illumination, and suppressing migration artifacts. It can provide stable solutions even when the source signature is unknown because the inversion process can automatically accommodate that situation.

As computing capability is increasing, LSM is widely used in exploration and reflection seismology. It is considered to be the next generation of seismic imaging and migration. The approach may also improve imaging of large continental scale structures. For example, it can be directly applied to the receiver function Kirchhoff migration. While it is theoretically applicable, there will be some practical issues. The receiver function data can be noisy and the velocity model used in migration is not accurate. This chapter serves as an introduction to future work, and hopefully provide a possible path to improved continental scale imaging.

5.5 Bibliography

Claerbout, J. (1971) Toward a unified theory of reflector mapping. *Geophysics*, 36, 467–481, doi: 10.1190/1.1440185.

Dai, W., X. Wang, and Schuster G. (2011) Least-squares migration of multisource data with a deblurring filter. *Geophysics*, 76, no. 5, R135–R146, doi: 10.1190/geo2010-0159.1.

McMechan, G. (1983) Migration by extrapolation of time-dependent boundary values. *Geophysical Prospecting*, 31, 413–420, doi: 10.1111/j.1365-2478.1983.tb01060.x.

Nemeth, T., Wu, C. and Schuster, G. (1999) Least-squares migration of incomplete reflection data: Geophysics, 64, 208–221, doi: 10.1190/1.1444517.

Ristow, D. and Ruhl, T. (1994) Fourier finite-difference migration: Geophysics, 59, 1882–1893.

Schneider, W. (1978). Integral formulation for migration in two and three dimensions. *Geophysics*, 43, 49–76, doi: 10.1190/1.1440828.

Schuster, G. (1993). Least-squares crosswell migration. *63rd Annual International Meeting, SEG*, Expanded Abstracts, 110–113.

Wang, J., Kuehl, H. and Sacchi, M. D. (2005) High-resolution wave-equation AVA imaging: Algorithm and tests with a data set from theWestern Canadian Sedimentary Basin. *Geophysics*, 70, no. 5, S91–S99, doi: 10.1190/1.2076748.

Whitmore, D. (1983) Iterative depth migration by backward time propagation. *53rd Annual International Meeting*, SEG, Expanded Abstracts, 382–385.

Xu, S., Zhang, Y. and Tang, B. (2011) 3D angle gathers from reverse time migration. *Geophysics*, 76, no. 2, S77–S92, doi: 10.1190/1.3536527.

Zhang, Y., and Sun, J. (2009) Practical issues of reverse time migration: True amplitude gathers, noise removal and harmonic-source encoding. *First Break*, 26, 29–35.

Zhang, Y., Duan, L. and Xie, Y. (2013) A stable and practical implementation of least-squares reverse time migration. *83rd Annual International Meeting, SEG*, Expanded Abstracts, 3716–3720.